Galactic Winds and Structure of z~2 Star-forming Galaxies

Author
Newman, Sarah

Publication Date
2013

Galactic Winds and Structure of $z \sim 2$ Star-forming Galaxies

By

Sarah F. Newman

A dissertation submitted in partial satisfaction of the

requirements for the degree of

Doctor of Philosophy

in

Astrophysics

in the

Graduate Division

of the

University of California, Berkeley

Committee in charge:

Reinhard Genzel, Chair
Chris McKee
Mariska Kriek
Steven Boggs

Fall 2013

Galactic Winds and Structure of $z \sim 2$ Star-forming Galaxies

Abstract

Galactic Winds and Structure of $z \sim 2$ Star-forming Galaxies

by

Sarah F. Newman

Doctor of Philosophy in Astrophysics

University of California, Berkeley

Reinhard Genzel, Chair

Galactic-scale outflows are a key driver of galaxy evolution through their feedback effect on star-formation and their ejection of metals and energy into the inter-galactic medium (IGM). While it is known that outflows likely play an important role in the quenching of star-formation - transforming actively star-forming, blue galaxies into their 'red and dead' counterparts - this role is currently not well understood. In particular, at $z \sim 2$, during the most active epoch of star-formation, the mass and energy in these outflows is poorly constrained, as is the mechanism for launching them. Furthermore, active-galactic nuclei (AGN) in the centers of massive star-forming galaxies (SFGs) likely play an important role in star-formation quenching, but we do not have a clear understanding of how this AGN feedback compares with that of star-formation driven feedback, and it is not known how many of these massive SFGs at $z \sim 2$ even have AGN. This issue is complicated by the fact that many high-z AGN are likely highly obscured, and have strong nebular emission line contributions from both star-formation and the AGN.

In this dissertation, I explore these issues using high-spatial and spectral resolution integral field unit spectroscopic data of $z \sim 2$ SFGs. The observations are obtained with the instrument SINFONI on the European Southern Observatory (ESO) Very Large Telescope (VLT) at Cerro Paranal. These high-quality data allow spatially-resolved studies of the gas-phase kinematics of these galaxies, as well dynamical information on their outflows. In this work, I explore outflow properties in one galaxy with exceptionally deep data, allowing detailed examination of the outflow energetics, spatial extent and underlying ISM properties, as well those from a larger sample of galaxies. I also probe the fraction of SFGs in our sample which contain (possibly obscured) AGN, and study how this affects our determination of galaxy properties, such as gas-phase metallicity. Finally, I study a subsample of $z \sim 2$ galaxies whose turbulent velocities dominate the kinematic signature, and examine the link between the overall evolution of $z \sim 2$ galaxies and the systems we see today. Together this body of work explores how galactic-scale outflows in $z \sim 2$ SFGs are launched, effect the IGM and eventually shape the evolution of their host galaxies.

I dedicate this dissertation to my parents.

Contents

List of Figures

List of Tables

Acknowledgments

First and foremost, I'd like to thank my advisor, Reinhard Genzel for his patience and support throughout my graduate school tenure. I would also like to thank Kristen Shapiro Griffin, who served as both a mentor and a friend to me during the last four years, and who has made my life a whole lot easier. In addition, Linda Tacconi and Natascha Förster Schreiber have been very supportive both during my frequent trips to Garching, but also during their visits to Berkeley. Peter Buschkamp among many other things, taught me how to reduce data. I'd also like to thank Mariska Kriek, for our many useful conversations and her guidance. I thank Peter Williams for creating this very useful thesis template.

I also want to thank Bonnie Buratti, my supervisor at JPL, who continues to be an inspiration and a mentor to me. And Richard Binzel, my undergraduate advisor, who first helped me discover my interest in Astronomy and guided me during a difficult time switching departments.

Finally, I'd like to thank my parents, brother Mark, and husband Lukasz for their continued love and support.

Chapter 1

Introduction

1.1 Opening Remarks

The study of the $z \sim 2$ universe is of great importance in understanding the evolution of the first galaxies into those we see today in the local universe. During the epoch of z $\sim$ 2–3, massive galaxies were forming stars more rapidly and quasars more active than any other time in the history of the universe (Madau et al. 1996; Lilly et al. 1996; Steidel et al. 1999; Juneau et al. 2005). Thus, in order to understand where we came from, we must examine the structure, dynamics and eventual fate of these high-z galaxies.

Over the last 10 years, this field has been revolutionized by the use of integral field units (IFUs) mounted on 10m-class telescopes paired with adaptive optics, allowing us to map out resolved properties across $z \sim 2$ galaxies without the constraints previously experienced with slit-based spectroscopy and with exceptional spatial resolution. The work presented in this thesis is only possible thanks to these technological developments.

1.2 Morphology and Kinematics of $z \sim 2$ Star-forming Galaxies

Most star-forming galaxies (SFGs) that we study at z $\sim$ 2-3 are selected either from their rest-ultraviolet (UV) or rest-optical colors. Several techniques exist for separating potential targets from other sources, and these divide high-z galaxies into different categories, which include:

- UV color-color selection of actively star forming galaxies, including the BX and BM classes, (e.g. Steidel et al. 1996, 2004),
- BzKs, which are selected from their B, Z and K_s or J and K magnitudes (e.g. Daddi et al. 2004a; Franx et al. 2003; Daddi et al. 2007),
- SMGs, selected from their sub-millimeter flux (e.g. Smail et al. 1997).

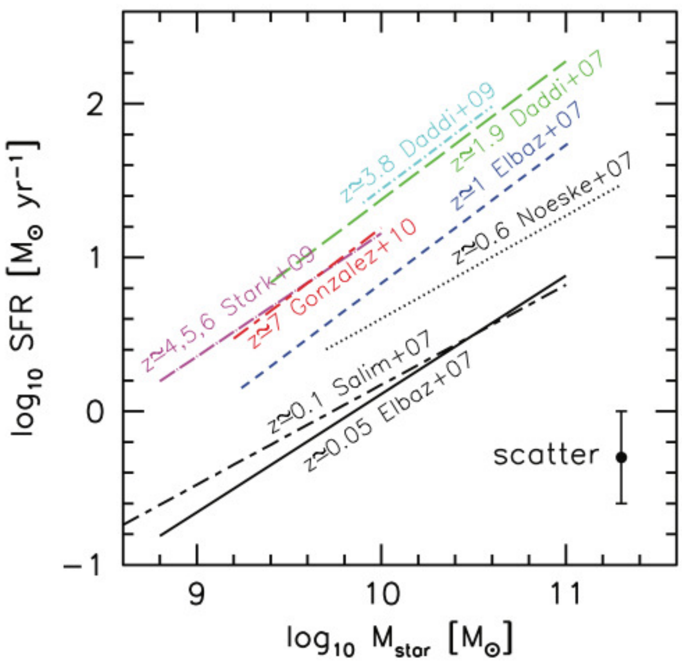

Figure 1.1: The star formation rate/stellar mass plane of star-forming galaxies from Dutton et al. (2010).

Many SMGs are likely the product of major mergers at the brightest end (Chapman et al. 2003; Swinbank et al. 2004; Tacconi et al. 2006, 2008; Engel et al. 2010), but the fainter objects are a mixture of massive 'main-sequence' SFGs (often with two objects in one beam, see: Hayward et al. 2012) and cold dust objects (Magnelli et al. 2012). As a mass-selected sample, they only constitute 2% of the SFG population and 10% of the cosmic SFR density at $z \sim 2$ (Rodighiero et al. 2011). Thus, they may not be significant for understanding the evolution of the bulk of the galaxy population.

The remaining $z \sim 2$ SFGs, selected by their rest-UV and rest-optical colors appear to form a 'main sequence' of star-formation, with a clear correlation between stellar mass and star formation rate (SFR) (Adelberger et al. 2004; Noeske et al. 2007; Daddi et al. 2007; Elbaz et al. 2007), a correlation which appears to extend from z $\sim$ 0 to z $\sim$ 8 (see Figure 1.1, Gonçalves et al. 2010; Wuyts et al. 2011b; Stark et al. 2009; Daddi et al. 2009). While these $z \sim 2$ 'main sequence' galaxies appear responsible for the majority of star-formation, and do so in a steady-state mode (Adelberger et al. 2004; Noeske et al. 2007; Daddi et al. 2007), their properties are quite different from their local counterparts (i.e. the Milky Way), including much higher SFRs, gas fractions and interstellar pressures (Wuyts et al. 2011a, and references therein), as is the case for many SMGs and local ULIRGs .

One of the most striking aspects of these $z \sim 2$ SFGs is their rest-UV/rest-optical morphologies (see Figure 1.2). They exhibit highly clumpy and irregular morphology, more

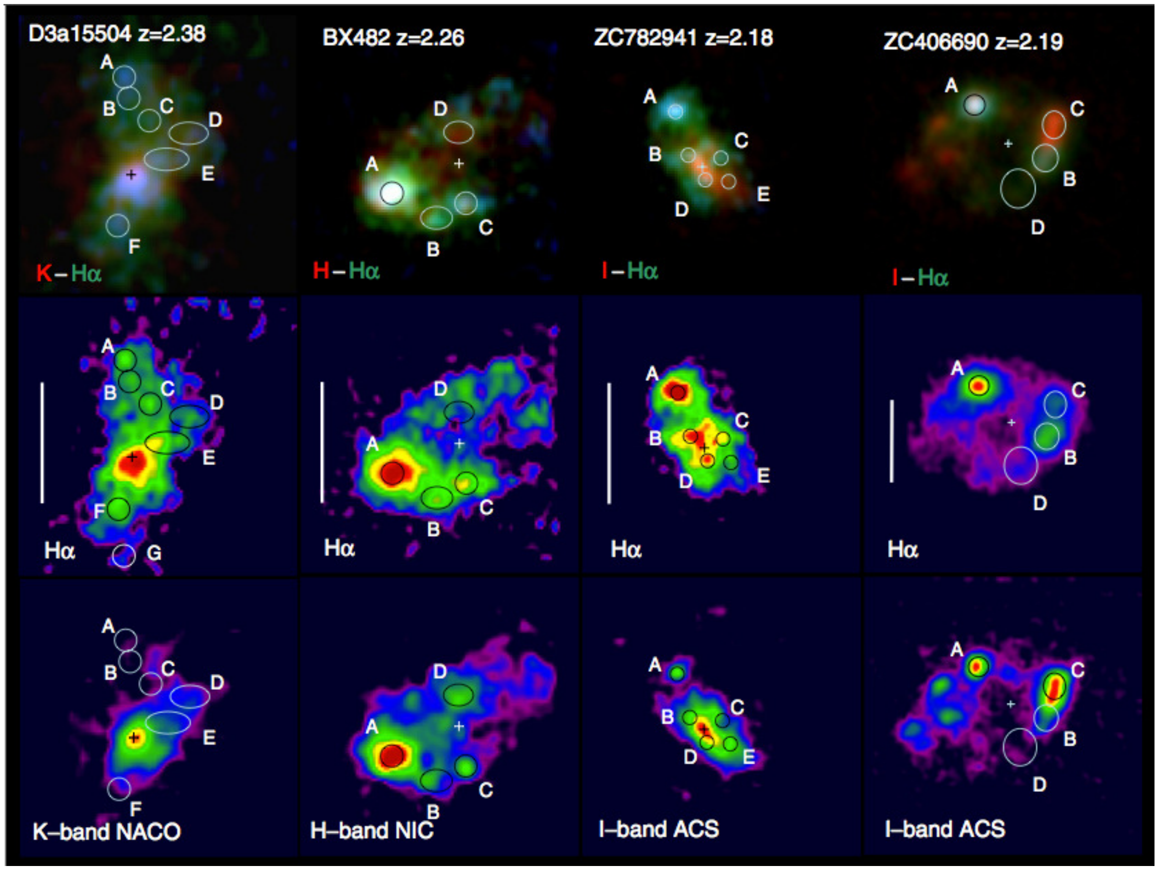

Figure 1.2: Hα and rest-frame optical/UV continuum images of four $z \sim 2$ SFGs from the SINS survey. The circles denote the locations of star-forming clumps and the crosses denote the morphological centers of the galaxies. Figure from Genzel et al. (2011).

reminiscent of local ULIRGs than normal star-forming disks (Cowie et al. 1995; van den Bergh et al. 1996; Elmegreen et al. 2004a, 2009b; Elmegreen & Elmegreen 2005, 2006; Genzel et al. 2006, 2008, 2011; Law et al. 2007, 2009, 2012c; Förster Schreiber et al. 2009, 2011a; Wuyts et al. 2011a; Swinbank et al. 2012b,a). However, as mentioned before, they appear to be in a phase of steady-state star-formation, and therefore the clumps are likely not individual galaxies in the process of a major merger (as is the case for many SMGs, see: Engel et al. (2010)) (Kennicutt et al. 2007; Bigiel et al. 2008; Shapiro et al. 2008; Genzel et al. 2010; Daddi et al. 2010a). Further supporting this, are stellar mass maps created by spatially-resolved SED modeling (Wuyts et al. 2012), which appear smooth and do not show peaks at the location of clumps.

In addition, the kinematics of these clumpy $z \sim 2$ SFGs show ordered velocity gradients with a peak in the velocity dispersion near their kinematic centers, suggesting that they are rotating disks (Shapiro et al. 2008; Förster Schreiber et al. 2009; Genzel et al. 2011). However, many $z \sim 2$ SFGs appear to be dominated by random motion with beam-smearing corrected velocity dispersions exceeding their inclination-corrected rotational velocities and even those galaxies with apparent ordered rotation have very large velocity dispersions of 50–100 km s^{-1}(Förster Schreiber et al. 2006, 2009; Law et al. 2007, 2009; Genzel et al. 2008, 2011; Wright et al. 2007, 2009; Shapiro et al. 2008; Cresci et al. 2009; van Starkenburg et al. 2008; Epinat et al. 2009, 2012; Lemoine-Busserolle & Lamareille 2010; Jones et al. 2012; Wisnioski et al. 2012; Swinbank et al. 2012b,a). Several scenarios have been suggested to explain these elevated (as compared with local disks) velocity dispersions, including accretion from the halo or outer regions of the disk, feedback from star-formation, or turbulence from the interaction of clumps and filaments within the disk (Förster Schreiber et al. 2009; Law et al. 2007, 2009, 2012b; Jones et al. 2010; Epinat et al. 2012), yet it is still unclear which scenario(s) is responsible.

This issue is further complicated by the need to separate the intrinsic velocity dispersion from that attributed to line-broadening from large-scale galactic outflows. This topic is discussed further in the following section.

1.3 Galactic-scale Outflows

Galactic-scale outflows, inflow and star-formation govern the dilution and enrichment of metals within galaxies, its subsequent expulsion into the inter-galactic medium (IGM) and potential re-aquisition through recycling back into the inter-stellar medium (ISM) (Martin 1998; Devine & Bally 1999; Lehnert et al. 1999; Strickland et al. 2004; Rupke et al. 2005; Martin 2005; Steidel et al. 2010; Sturm et al. 2011). In addition, outflows are likely an important ingredient in the self-regulating feedback of star-formation in high-z SFGs, preventing them from consuming all of their gas in a few dynamical timescales (Katz et al. 1996; Somerville & Primack 1999; Cole et al. 2000; Springel & Hernquist 2003; Finlator & Davé 2008; Kereš et al. 2009; Genel et al. 2012b; Davé et al. 2011). Characterizing the structure, energetics and mass in these winds is key for constraining the metal enrichment of the IGM, and understanding both the baryon and metal content of galaxies as well as the process of quenching of star formation, eventually turning actively star forming galaxies from the blue cloud into their 'red and dead' counterparts.

In the local universe, large scale outflows are observed in a hot phase (X-rays), warm phase (Hα), neutral phase (Lyα, MgII, NaI D), and cold molecular phase (OH, CO) mostly in extreme objects such as ULIRGS, dwarf starbursts and AGN (Veilleux et al. 2005, and references therein). X-ray and Hα emission are often seen at the interface between the hot wind fluid, moving at 1000s of km/s and cooler clouds in the ISM or halo of the galaxy (Veilleux et al. 2005, and references therein). This emission often traces out a bipolar hourglass shape in galaxies viewed almost edge on (Veilleux et al. 2005, and references therein).

In contrast, at high-z, outflows are observed in almost all 'normal' SFGs, that is galaxies forming stars in a steady state mode (Pettini et al. 2000; Shapley et al. 2003; Weiner et al. 2009; Steidel et al. 2010; Kornei et al. 2012). Much of the pioneering work for high-z

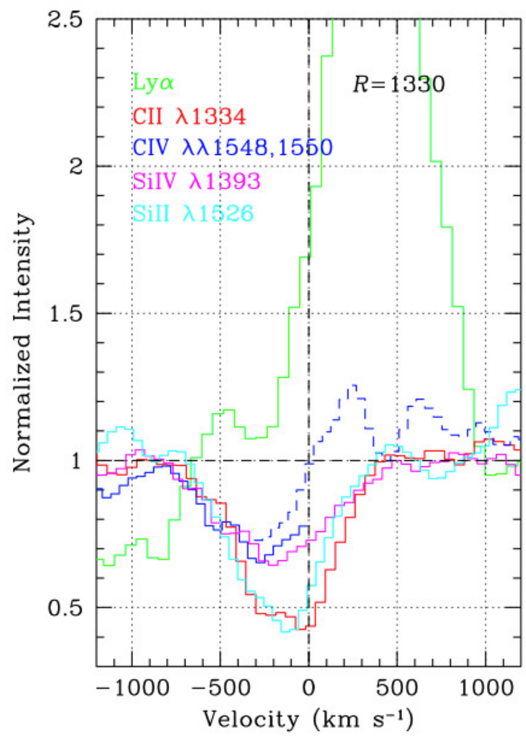

Figure 1.3: Velocity profiles of interstellar UV absorption and Lyα emission lines from a stack of 1330 CGM spectra around $z \sim 2$ LBGs from Steidel et al. (2010). Lyα emission is redshifted with respect to the galaxy systemic redshift, while the interstellar absorption is blueshifted, characteristic of an outflow signature.

outflows came from observations of blue-shifted low ionization interstellar absorption lines (e.g. MgII, NaI D) and redshifted Lyα emission around Lyman break galaxies (LBGs) (e.g. Lowenthal et al. 1997; Pettini et al. 2000, 2001, 2002; Adelberger et al. 2003; Shapley et al. 2003) and in the circum-galactic medium (CGM) of SFGs as viewed from the spectra of background quasars or galaxies (Steidel et al. 2004, 2010; Bordoloi et al. 2012; Kacprzak et al. 2012; Bouché et al. 2012, see Figure 1.3). Recent work using similar techniques has shown that there is a strong trend between detection rate of outflowing gas and inclination of the host galaxy, suggesting that when no winds are detected around a galaxy, it is merely an orientation effect (Kornei et al. 2012, Rubin et al. in prep.).

While studying the CGM around SFGs using background sources is a powerful tool to quantify the prevalence of outflows in a statistical sense, examining the outflowing gas in emission directly from the galaxy can give us different types of information on the outflow. Firstly, while the absorption line studies measure the neutral gas component of the outflow, Hα emission line data probes the warm ionized component, which may be photoionized directly by UV photons from HII regions or from shocks generated from the hot wind fluid impinging on cool clouds in the ISM or halo of the galaxy (Veilleux et al. 2005). In addition, resolved IFU data of $z \sim 2$ galaxies, allows us to simultaneously examine the kinematics of the gas in the galactic disk and the dynamics of the outflowing gas. Shapiro et al. (2009) showed from the stacked spectra of 4 AGN and 43 non-AGN SFGs, that both groups had evidence for large-scale outflows with broad wings flanking the Hα emission line profiles, and that a non-trivial fraction of the gas had velocities exceeding the galactic escape velocity. It was later demonstrated by Genzel et al. (2011) that a substantial amount of the broad emission and thus outflowing gas in these $z \sim 2$ SFGs was coming from Hα-bright star-forming clumps. Much of the work in this dissertation exploits such IFU data to further probe the origin and properties of galactic outflows in $z \sim 2$ SFGs.

1.4 This Thesis

This dissertation explores several of the aforementioned key issues in galaxy evolution, and attempts to answer the questions:

- **What drives galactic-scale winds at $z \sim 2$?**
  What is the structure of and energy contained in these winds? What role do active-galactic nuclei (AGN) vs. star-formation play? How does the amount of outflowing gas correlate with different galaxy properties? What fraction of star-formation and outflowing gas originates in the clumps?

- **How do winds affect their host galaxies?**
  Can they drive the elevated velocity dispersions observed at $z \sim 2$? Are they able to quench star-formation?

- **What is the nature of dispersion dominated SFGs at $z \sim 2$?**
  Are they linked in evolution to large, rotating disks or an entirely different class? What can they tell us about how galaxies form and evolve?

In Chapter 2, I explore the the first two questions by analyzing in detail one stunning galaxy from the SINS/zC-SINF survey (Förster Schreiber et al. 2009; Mancini et al. 2011). This galaxy, ZC406690, from the ZCOSMOS survey (Lilly et al. 2007), is a large-rotating disk with two bright clumps, and strong evidence for outflows. By probing high-resolution spectra of the clumps and regions surrounding them, we are able to learn about the structure and energetics of the gas outflowing directly from and the ISM properties within the clumps.

In Chapter 3, I take the study of $z \sim 2$ outflows to a larger sample of 27 SFGs. This allows an understanding of outflow properties in general, not just from one extreme object. In addition, we are able to probe how outflow velocity and strength varies with galaxy properties such as star formation rate, stellar mass, and star formation rate surface density. By stacking the spectra of many galaxies, we are able to probe for additional information that is not possible with one (even high signal to noise ratio) spectrum, such as the electron density of the outflowing gas.

In Chapter 4, I discuss the population of $z \sim 2$ SFGs that are dominated by turbulence: dispersion-dominated galaxies. By understanding what defines this class, and how they differ from rotationally-supported galaxies, we can begin to probe their evolutionary link and how this ties in to the effects of star-formation feedback and galaxy growth.

In Chapter 5, I use emission line ratio diagnostics to probe the prevalence of AGN in our sample of $z \sim 2$ SFGs. Using spatially-resolved data, we are able to glean additional information from these diagnostics and study the varying effects of shock ionization (possibly from outflows) and AGN to the line ratios. We also examine how these processes can affect metallicities calculated from line ratios with calibrations determined locally.

Together, these Chapters discuss the properties of galactic-scale winds in $z \sim 2$ SFGs from studies of individual objects and from a larger sample. They examine both the contribution from star-formation feedback and AGN, from many different types of SFGs, and from different physical processes in the ISM surrounding star-forming regions. I hope that this dissertation can shine some light on how outflows from high-z SFGs impact their evolution and that of the surrounding inter-galactic and circum-galactic media.

Chapter 2

Shocked Superwinds from the $z \sim 2$ Clumpy Star-forming Galaxy, ZC406690

We have obtained high-resolution data of the $z \sim 2$ ring-like, clumpy star-forming galaxy (SFG) ZC406690 using the VLT/SINFONI with AO (in K-band) and in seeing-limited mode (in H- and J-band). Our data includes all of the main strong optical emission lines: [OII], [OIII], Hα, Hβ, [NII], and [SII]. We find broad, blueshifted Hα and [OIII] emission line wings in the spectra of the galaxy's massive, star-forming clumps ($\sigma \sim 85$ km s^{-1}) and even broader wings (up to 70% of the total Hα flux, with $\sigma \sim 290$ km s^{-1}) in regions spatially offset from the clumps by ~ 2 kpc. The broad emission likely originates from large-scale outflows with mass outflow rates from individual clumps that are 1–8x the SFR of the clumps. Based on emission line ratio diagnostics ([NII]/Hα and [SII]/Hα) and photoionization and shock models, we find that the emission from the clumps is due to a combination of photoionization from the star-forming regions and shocks generated in the outflowing component, with 5–30% of the emission deriving from shocks. In terms of the ionization parameter (6x10^7–10^8 cm/s, based on both the SFR and the O_{32} ratio), density (local electron densities of 300–1800 cm^{-3} in and around the clumps, and ionized gas column densities of 1200–8000 M$_\odot$/pc^2), and SFR (10–40 M$_\odot$ yr^{-1}), these clumps more closely resemble nuclear starburst regions of local ULIRGs and dwarf irregulars than HII regions in local galaxies. However, the star-forming clumps are not located in the nucleus as in local starburst galaxies but instead are situated in a ring several kpc from the center of their high-redshift host galaxy, and have an overall disk-like morphology. The two brightest clumps are quite different in terms of their internal properties, energetics and relative ages, and thus we are given a glimpse at two different stages in the formation and evolution of rapidly star-forming giant clumps at high-z.

2.1 Introduction

Galactic-scale outflows are ubiquitous in local starburst galaxies and in most high-redshift star-forming galaxies (SFGs) (Heckman et al. 1993; Lehnert & Heckman 1996; Steidel et al.

1996; Franx et al. 1997; Pettini et al. 2000, 2001; Shapley et al. 2003; Adelberger et al. 2003, 2005; Veilleux et al. 2005; Erb et al. 2006b; Weiner et al. 2009; Sato et al. 2009; Rubin et al. 2010; Law et al. 2012c). These 'superwinds' have a profound impact on the gas content and metallicity of the inter-galactic medium (IGM), injecting enriched, hot and cold gas into the halos and often out of the gravitational potentials of the host galaxies (Martin 1998; Devine & Bally 1999; Lehnert et al. 1999; Strickland et al. 2004; Rupke et al. 2005; Martin 2005; Steidel et al. 2010; Sturm et al. 2011). Star-formation feedback in the form of these winds is key to understanding galaxy evolution, as they can modulate the star formation activity in gas-rich disks (Katz et al. 1996; Somerville & Primack 1999; Cole et al. 2000; Springel & Hernquist 2003; Finlator & Davé 2008; Kereš et al. 2009; Genel et al. 2012b; Davé et al. 2011).

Galactic winds in local starburst galaxies are most easily observed in edge-on systems in optical, near-IR, soft x-ray and radio emission, but outflows have also been detected in face-on galaxies from blue-shifted absorption by dense clouds in the ISM in front of the galactic disks (Veilleux et al. 2005, and references therein). While these winds are clearly important for ongoing galaxy evolution and star-formation, little is known about the role of such large-scale outflows in high-redshift galaxies, particularly between z $\sim$ 1–3, when massive local galaxies were undergoing their most powerful epoch of star formation and nuclear activity (Madau et al. 1996; Lilly et al. 1996; Steidel et al. 1999; Juneau et al. 2005; Le Floc'h et al. 2005; Le Borgne et al. 2009).

In the last 15 years, outflows at high redshift have been increasingly observed, most often in Lyman Break Galaxies (LBGs) and QSO absorption line systems (Steidel et al. 1996; Franx et al. 1997; Pettini et al. 2000, 2001; Shapley et al. 2003; Adelberger et al. 2003, 2005; Veilleux et al. 2005; Weiner et al. 2009; Rubin et al. 2010). Recently, Shapiro et al. (2009) observed broad Hα emission lines from the stacked spectra of 47 $z \sim 2$ SFGs, possibly indicative of outflows of several hundred km s^{-1} and mass outflow rates comparable to the galaxies' SFRs. In addition, Steidel et al. (2010) found interstellar (IS) absorption and Lyα emission from gas spatially offset from $\sim$100 z $\sim$ 2–3 LBGs using background galaxies, indicating that most of their sample of high-z galaxies produced metal-enriched galactic outflows. A subset of this sample was further analyzed by Law et al. (2012c) with HST/WFC3 imaging who found that outflow characteristics were correlated with rest-frame optical morphology. These previous studies did not have sufficient spatial resolution to resolve the source of the outflows, however. More recently, with high spatial resolution adaptive optics integral-field observations, Genzel et al. (2011) have observed powerful outflows emanating directly from massive, M $\sim 10^{9-10}$ M$_\odot$, star-forming clumps in five rotationally-supported SFGs at z $\sim$ 2. These clumps are at the high-mass end of the types of clumps observed with HST imaging by Förster Schreiber et al. (2011a,b) in $z \sim 2$ SFGs and by Elmegreen et al. (2004b, 2005), Elmegreen & Elmegreen (2006), Elmegreen et al. (2009b), Elmegreen & Elmegreen (2010), and Guo et al. (2011) in tadpole, chain, and clump-cluster galaxies in the Hubble UDF at z $\sim$ 1–5. In this paper, we present deep, follow-up, multi-band observations of one of the galaxies from Genzel et al. (2011), ZC406690.

ZC406690 is part of the "zC-SINF" program aimed at studying the spatially-resolved kinematic and star-formation properties of $z \sim 2$ galaxies with the SINFONI integral field spectrograph at the ESO Very Large Telescope (Mancini et al. 2011). The galaxy was originally drawn from the K-band limited sample in the COSMOS field (McCracken et al. 2010) with the additional "sBzK" color criterion, selecting candidate $1.4 < z < 2.5$ star-forming galaxies (Daddi et al. 2004b). Its redshift of 2.19 was confirmed from the zCOSMOS-Deep optical spectroscopic campaign (Lilly et al. 2007). The SINFONI seeing-limited and adaptive optics-assisted observations revealed that it is a rotating, clumpy ring with $M_* \sim 4 \times 10^{10}$ $M_\odot$, and $M_{gas} \sim 2 \times 10^{11}$ $M_\odot$, where M_{gas} is uncertain by a factor of 2–3 (Mancini et al. 2011; Genzel et al. 2011). With a UV-derived star-formation rate (SFR_{UV}) of 337 $M_\odot$ yr^{-1}, ZC406690, falls on the SFR-M_*main sequence on the high-mass and high-SFR end of the range of SINS and zC-SINF galaxies (Förster Schreiber et al. 2009; Mancini et al. 2011; Wuyts et al. 2011b) and the sample from Förster Schreiber et al. (2011a,b). This SFR is in good agreement with the total amount of star formation estimated from Hα corrected for extinction with the best-fit Av from SED modeling and adopting an extra nebular correction of 2.5 (354 $M_\odot$ yr^{-1}) (see Calzetti et al. 2000).

Genzel et al. (2011) found that ZC406690 is ejecting mass several times faster than it is forming stars ($\dot{M}_{out} \sim$ 3–8 x SFR), as traced through broad, blue-shifted Hα emission line wings centered on most clumps, indicative of an outflowing warm ionized component. This finding is consistent with previous galaxy-integrated observations of outflows from SFGs at high-z (Steidel et al. 2010; Pettini et al. 2000; Weiner et al. 2009). With an observed wind outflow velocity of 440 km s^{-1}, the brightest and most massive clump in ZC406690 falls very closely on the v_{out}-M_* and v_{out}-SFR relations observed by Weiner et al. (2009) for high-z galactic outflows. This suggests that whatever is driving the relation between star-formation and feedback on galactic scales still holds on the kpc-scales of giant clumps.

This compelling evidence for massive, galactic scale outflows originating in ~1 kpc clumps has motivated us to follow-up on these original observations. We exploit here the deep SINFONI+AO data to create individual spectra of not just the clumps, but of the surrounding regions, whose signal is dominated by the outflowing component projected onto the disk. With excellent S/N we are able to create emission line maps of [NII]λ6584 and [SII]λ6716 as well as the broad and narrow components of the Hα emission line, enabling us to probe the spatially resolved structure and density of the wind. With new seeing-limited J and H band data of the galaxy, we obtain emission line fluxes of [OIII]λ5007,4959, Hβ, and [OII]λ3726,3729. This new data enables us to put the clumps in the BPT diagram (Baldwin et al. 1981; Veilleux & Osterbrock 1987), along with local SFGs and starbursts as well as other high-z SFGs. We can then compare the ISM properties (ionization state, SFR, density, metallicity, star-formation history) of spatially-resolved high-z star-forming clumps with those of different types of local star-forming regions to better understand the conditions required for these massive outflows and how the clumps fit into the overall picture of galaxy evolution.

In section 2.2, we outline the observations used as well as our reduction and analysis techniques. In section 2.3, we present the new spectra of individual regions, emission-line maps, and shock-diagnostic diagrams based on more detailed examination of the K-band data and the new H- and J-band data. In section 2.4, we compare the results to those of local and high-z star forming galaxies and discuss the implications. In section 2.5, we summarize our findings. Throughout this paper, we adopt a ΛCDM cosmology with $\Omega_m = 0.27$, $\Omega_b = 0.046$, and $H_0 = 70 \mathrm{kms}^{-1}\ \mathrm{Mpc}^{-1}$ (WMAP7, Komatsu et al. 2011), as well as a Chabrier (2003) initial stellar mass function (IMF).

2.2 Observations, Data Reduction and Analysis Techniques

2.2.1 Observations and Data Reduction

We observed ZC406690 with SINFONI/VLT integral field unit spectroscopy (Eisenhauer et al. 2003; Bonnet et al. 2004) using natural guide star adaptive optics (AO) in K band for 10 hours to achieve a spatial resolution of 0.22" (1.85 kpc) FWHM (as presented in Genzel et al. (2011)). Each observation block (OB) consisted of an "O-S-O-O-S-O" sequence, with 4 on-source exposures and 2 others taken on empty 'sky' positions about 20 arcsec away from the target. For each on-source frame, the object's position was varied around the center by ± 0.4" to avoid redundancy. Off-source "sky" frames were necessary because the source fills a significant fraction of the 3.2" x 3.2" FOV at that pixel scale. Individual exposure times were of 600s, giving 2400s on-source per OB, and thus a total on-source integration time of 10h (for 15 OBs). The resulting cube has 0.05" spatial pixels and 0.000245 μm spectral pixels.

We also observed the galaxy in seeing-limited mode in J– (100 minutes) and H–band (120 minutes), obtaining ∼0.6" FWHM with a pixel size of 0.125" x 0.000195 μm. With this pixel scale, the larger FOV of 8" x 8" allowed an on-source dithering strategy, such that each OB consisted of six on-source exposures, with the source positioned alternatively in one or the other half of the FOV, with additional small dithering of ∼1/10 of the FOV to avoid redundant positions. Individual exposure times were all of 600s, giving 3600s on-source per OB, and a total on-source integration time of 2h per band (for 2 OBs each). Note that we only use 100 minutes of integration time in the reduced J–band cube, as the first two exposures had faulty pointings.

For all AO and no-AO OBs, images of the acquisition star taken before the science exposures were used to monitor the positioning and the PSF for the OBs. Standard stars of O or early-B types were observed each night, at similar airmass as the science data, and used to correct for the telluric transmission and to provide the absolute flux calibration.

For the data reduction, we used the software package SPRED (Schreiber et al. 2004) and custom routines for optimizing the background/OH airglow subtraction. For combining the individual exposures, we determined the relative offsets between frames using the known offsets for frames within individual OBs and using the position of the aquisition star, for frames in different OBs. The effective PSF FWHM was determined from the combined PSF data sets associated with all OBs in a given band (fitting a 2D gaussian profile to the image made by averaging over all spectral channels). For more on the data reduction procedure, see Förster Schreiber et al. (2009) and Mancini et al. (2011).

We calculate the SFR from the Hα luminosity using the Kennicutt (1998) conversion adjusted to our adopted Chabrier (2003) IMF, and corrected for extinction. The extinction correction is described in Section 2.3.1.

2.2.2 Emission Line Maps

With the reduced K-band data cube, we create Hα, [NII]λ6584, and [SII]λ6716,6731 maps by simultaneously fitting Gaussian components to each of the emission lines, holding the nebular [NII]λ6584/6548 ratio fixed at the atomic value (3.28) and using the kinematics (line center, dispersion) derived from Hα and errors determined from the noise cube. Prior to fitting the emission lines, we smooth the data by 3 spatial pixels in each direction and 3 spectral pixels (5x3 for the [SII] map) to boost the S/N for the fainter nebular lines. Note that we only include a map for [SII]λ6716, since [SII]λ6731 is strongly affected by an OH sky line in some spatial elements. For all line maps, we show only pixels with S/N greater than 3σ.

We use the same reduction procedure for the H- and J-band cubes, but use a different technique to produce the emission-line maps. Since the S/N is not high enough to fit each line individually for each spatial pixel, the maps were obtained by spectrally integrating over the full width of each line. We further increase the S/N of the maps by smoothing over 3x3 spatial pixels. After the smoothing, all three maps were clipped by a S/N ratio of 3 and were overlayed with [OIII] intensity contours.

Broad and narrow Hα emission line maps are created by fitting a two-component Gaussian to the emission lines. The resulting broad Hα map is used to visualize the trend in broad emission surrounding one of the clumps, but the map itself has very low S/N, so we generate an alternate map for display purposes. This other broad Hα map is created by spectrally integrating over the wings of the Hα line for the velocity intervals [-430, -140 km s^{-1}] and [280, 570 km s^{-1}] around the centroid of the narrow component. The two maps of the broad Hα emission line are qualitatively similar.

2.2.3 Extraction of Spectra from Individual Regions

We create spectra of individual regions from our K-band data (Figures 2.1 and 2.2) by averaging the spectra over both narrow-line (clump) and broad-line (wind) regions. We select the 'wind' component based on the region of elevated [NII]/Hα around the clumps (see section 2.3.3). We fit the broad emission lines using two-component Gaussian fits with the velocity and width of all lines held equal to that of the Hα line. In some cases, the lines were fit equally well with a single Gaussian, which we assumed to be the case if the difference in χ^2 values over the Hα and [NII] region of the spectrum between the one- and two-component fits was less than 10%. For those spectra (clumps C and D), we use the single Gaussian fit. We find that the emission line profiles in all regions are well described by either one or two Gaussians. We report the relative contribution to the flux by the narrow and broad components in the next section and Table 2.1. We derive the error for the fit parameters (velocity dispersion, velocity, etc) by generating 1000 monte carlo realizations of the fit and taking the standard deviation for each parameter.

Table 2.1: Emission Line Data from the Clumps

Region	% broad	σ_{narrow}	σ_{broad}	[NII]/Hα	[SII]/Hα	% shock[a]	χ^2 fit
Clump A	50 ± 4.8	82.7 ± 4.2	199 ±11.9	0.11 ± 0.014	0.14 ± 0.029	5 ± 5	0.78
Wind A	44 ± 7.2	84.7 ± 4.9	197 ± 20.5	0.15 ± 0.036	0.21 ± 0.061	$10\ ^{+10}_{-5}$	0.64
Clump B	46 ± 4.6	81.9 ± 4.6	244 ± 68.2	0.20 ± 0.031	0.20 ± 0.055	$15\ ^{+25}_{-15}$	0.59
Wind B	71 ± 2.9	97.7 ± 6.0	291 ± 12.7	0.32 ± 0.032	0.27 ± 0.068	$30\ ^{+30}_{-20}$	0.58

[a]The shock contribution is calculated by comparing the data to Figure 10 of Rich et al. (2011).

For the H- and J-band spatially integrated spectra, we fit each of the [OIII]λ4959,5007, Hβ, and [OII]λ3726,3729 lines with a single Gaussian component because these lines have too low S/N to fit the underlying broad component. For H-band, we fit all of the lines using the kinematics of the [OIII]λ5007 line, and for J-band we constrain the two [OII] lines to have the same kinematics as Hα and fix their wavelength separation to the known value, but allow their relative intensities to vary. For emission line ratios that contain lines from multiple bands, we employ an extinction correction as outlined in Section 2.3.1 with an E(B-V) as determined from Hα/Hβ for clump A. In addition, for all ratios (except [NII]/Hα and [SII]/Hα), we use emission line fluxes derived from single-component Gaussian fits. When comparing K-band (higher spatial resolution) and H-band emission lines, we resample the K-band cube to match the H-band cube, and convolve the new K-band cube with the H-band PSF. The H- and J-band cubes have the same spatial and spectral resolution. We therefore use the exact same spatial pixels when extracting spectra of individual regions from H, K and J bands.

To create the [SII] line profiles (Figure 2.2) and ratios, we generate a "velocity-shifted" cube to increase the S/N. This is done by shifting the spectrum of each pixel based on the measured Hα velocity such that all pixels have their Hα peak at the same wavelength. This method has been shown to increase the S/N of region-integrated spectra (Shapiro et al. 2009). To negate the effects of an OH sky line that lies near the [SII]λ6731 emission line for parts of the galaxy, we create clump A and clump B spectra that have maximal S/N ratios in the wavelength range of this line. To this end, we define the spatial regions of the clumps by only adding spatial pixels to the spectra such that each additional pixel increases the S/N over a given threshold. Essentially, we only add pixels with a [SII]λ6731 S/N ratio ≥ 4. In this way, we only use measurements of the [SII]λ6731 line in pixels that are minimally affected by the OH sky line. In order to maximize the S/N, these regions must be quite extended, so to get [SII]λ6731 measurements for smaller areas within these larger regions (i.e. for the broad regions surrounding the clumps), we assume the measured [SII]λ6716/[SII]λ6731 ratio within the larger regions is constant. We can then estimate [SII]λ6731 fluxes based on the measured

[SII]λ6716 flux in the smaller regions and the measured [SII] ratio from the corresponding larger region.

The Hβ line is obstructed by an OH atmospheric line for about half of the galaxy. Therefore, to obtain an Hβ flux estimate for clump B (which falls in this right half), we assume clump B follows the extinction of the dense, clump gas and has the same observed Hα/Hβ ratio as clump A. We obtain an Hβ flux using this ratio and the Hα measurement for clump B, although this estimate is much more uncertain than the clump A Hβ flux.

2.3 Results

2.3.1 The Clumps are More Highly Extincted than the Surrounding Gas

The extinction correction used to calculate the SFR is based on the best-fit visual extinction derived from stellar population modeling of the UV to mid-IR spectral energy distribution (SED) presented by Mancini et al. (2011), for a Calzetti et al. (2000) reddening law. Following Calzetti et al. (2000), we assume that the Hα line emission is more attenuated than the bulk of stellar continuum light and thus correct the observed Hα luminosity for $A_{V(nebular)} = A_{V(SED)}$ x 2.5 (see also Förster Schreiber et al. 2009; Mancini et al. 2011; Wuyts et al. 2011b).

We also calculate the extinction for clump A and the left-half of the galaxy (which is unaffected by an OH sky line near the Hβ line) based on the Hα/Hβ ratio and using the Calzetti et al. (2000) reddening law, assuming an intrinsic ratio of 2.86 (Osterbrock 1989) appropriate for an electron density of 100 cm^{-3} and a temperature of 10^4 K. We find that the SED-based A_V (described above) assumed in Genzel et al. (2011) and Mancini et al. (2011) of 1.3 $\pm$ 0.5 (E(B-V) = 0.33 $\pm$ 0.1) is consistent with the diffuse emission from the galaxy (as calculated with Hα/Hβ from the left-half, A_V = 1.5 $\pm$ 0.8, E(B-V) = 0.37 $\pm$ 0.18) and that the nebular emission in clump A is more highly extincted (A_V = 2.0 $\pm$ 0.8, E(B-V) = 0.49 $\pm$ 0.17), as one would expect for a star-forming region. All of the forthcoming calculations use the clump Hα flux as calculated and corrected for extinction in Genzel et al. (2011). If we were to apply an extinction correction based on the Hα/Hβ measurement for clump A, the main clump properties ($L_{H\alpha}$, SFR, $\dot{M}_{\rm out}$, Σ_{gas}) would be increased by about 50%, and therefore the calculations made in Section 2.4 based on these quantities would be scaled accordingly. This relatively small factor will not affect any of the conclusions made in this paper.

2.3.2 Spectra of the Clumps and their Surroundings are Indicative of Localized Superwinds

We explore the properties of the star-forming clumps by creating individual spectra of both the clumps and their surrounding regions. In the regions surrounding the clumps, we find broader Hα emission lines and enhanced [NII]/Hα and [SII]/Hα ratios as compared to the clump regions. Enhancement of these emission line ratios could be due to several physical processes including the presence of shocks in a large-scale outflow or an AGN.

In this case, however, it is very unlikely that these large line ratios are due to an AGN. First, the region in which we find these large [NII]/Hα and [SII]/Hα ratios is extended, unlike an AGN point source. Second, these regions are located around clumps in the disk (or ring) of the galaxy, far from the center, where one would expect to find an AGN. The velocity field of the ring is also very regular and characteristic of face-on rotation, unlike what would be expected if clump A and clump B are the nuclei of merging galaxies. Third, the value of the elevated [NII]/Hα ratio in this region (0.3-0.5) is much less than those expected for AGN (at least 0.6-0.8). Fourth, we find that the [NII] emission is well fit by both a broad and a narrow component (see later in this section), which is inconsistent with classical broad-line regions around AGN. Finally, there is no evidence of an AGN from the ZCOSMOS optical spectra of this galaxy (Mancini et al. 2011).

We further discuss the possibility of shocks in Section 2.3.3, but even without the emission line ratios, the broad emission line wings (up to 800 km s^{-1}) in the spectra of the regions surrounding the clumps seem to indicate the presence of outflowing material. We therefore call these regions the clump A and clump B 'wind' regions.

In Figure 2.1, we show K–, H–, and J–band spectra from Clump A (the brightest and most massive clump) along with our best fit model. In Figure 2.2, we show emission line profiles of Hα and [NII]λ6584 for the four clumps in ZC406690 and the wind regions surrounding clumps A and B. Clumps A and B and the surrounding regions are well fit by two Gaussian profiles, with narrow components with FWHM = 200$\pm$8 km s^{-1} and FWHM = 210$\pm$9 km s^{-1} and underlying broad components with FWHM = 470$\pm$28 km s^{-1} and FWHM = 630$\pm$82 km s^{-1}, which we ascribe to outflowing material. On the other hand, clumps C and D can be well fit by one component with FWHM = 92$\pm$2 km s^{-1} and 89$\pm$2 km s^{-1}, suggesting little or no outflow from these clumps. The clump B wind spectrum is the most extreme example of a localized superwind with a very broad blue line wing, with the edge of the wing extending out to roughly 800 km s^{-1} from line center. In addition, the centroid of the broad component is blueshifted by 150$\pm$16 km s^{-1} from the narrow. This is consistent with the signature of a powerful outflow, as one would expect to see the majority of the outflowing material as blueshifted if the clumps are heavily obscured. The redshifted emission would fall behind the plane of the galaxy, and much of this emission would be extincted as it passes through the clumps as suggested by our Hα/Hβ measurements.

The fraction of Hα emission that comes from a broad-velocity component varies substantially for different regions in the galaxy. For the galaxy as a whole, broad emission accounts for roughly 33% $\pm$ 2% of the total Hα flux. For clumps A and B and wind A, the broad component accounts for about 50% $\pm$ 6% of the total Hα flux, while for wind B, broad emission comprises 70% $\pm$ 3% of the Hα flux. In all of the clump and wind regions, the narrow component likely derives from star-formation in the disk, while the broad component may come from a combination of turbulence and outflowing gas. In the case of wind B, the broad velocity-component peak wavelength is blueshifted slightly from the narrow-velocity

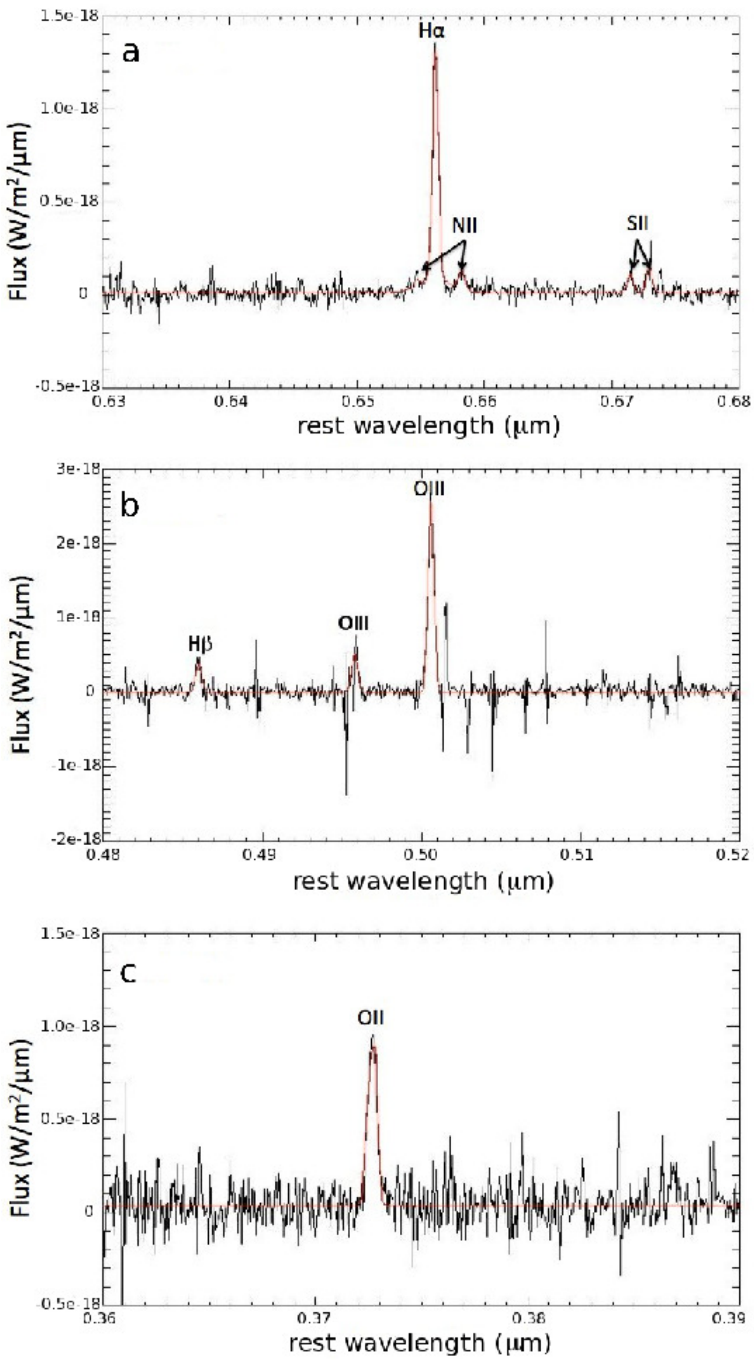

Figure 2.1: Panels a, b and c show K, H and J band spectra of clump A with the relevant emission lines labeled, respectively. The black line represents the data, while the red line shows our best fit. The wavelength axis is in rest-frame units.

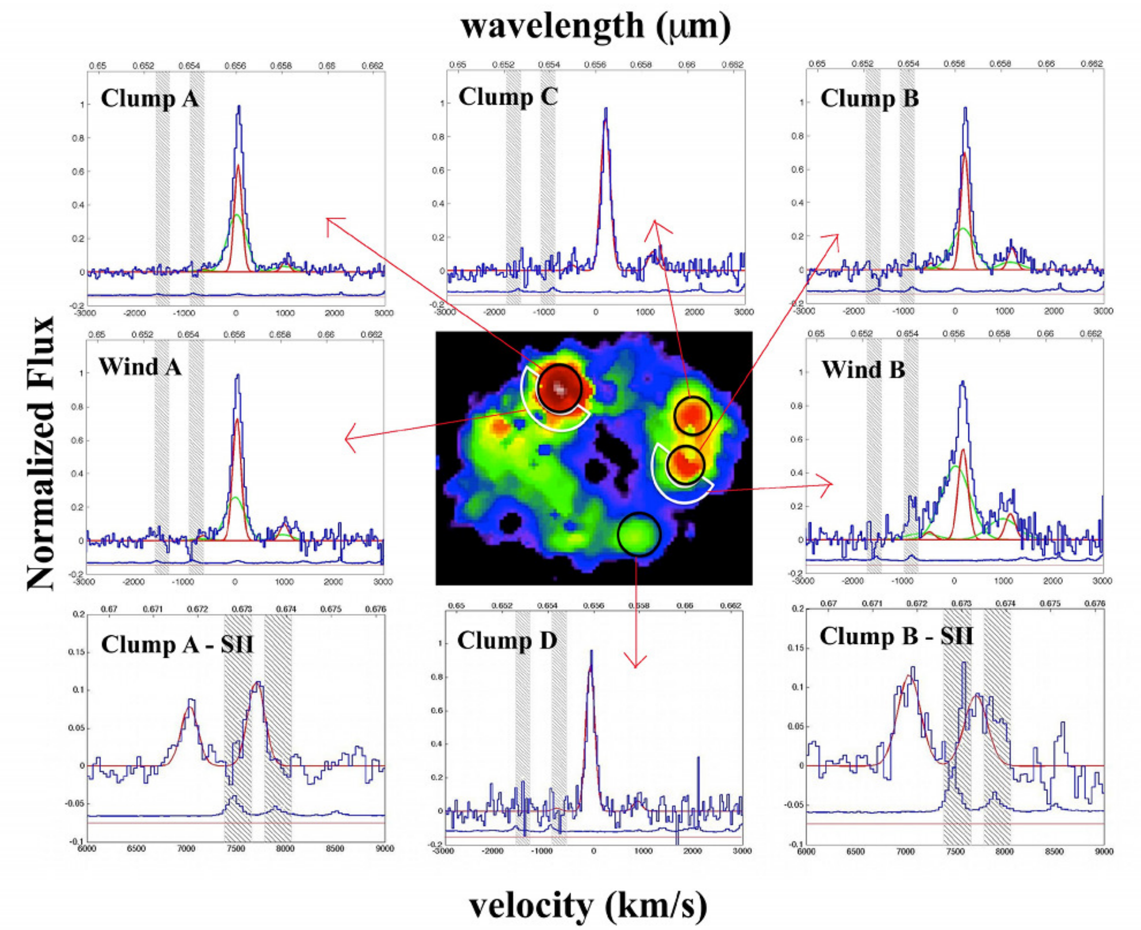

Figure 2.2: Emission line profiles and best fit to Hα and [NII]λ6584 features for six regions of ZC406690: clump A, clump A 'wind', clump B, clump B 'wind' and clumps C and D. Included with these spectra are one- or two-component Gaussian fits. For the two-component fits, the narrow component is shown in red and the broad in green. For the spectra with one-component fits, these are shown in red. The errors (1σ rms) are shown below in blue. Clumps A and B and their winds are well fit by two Gaussians, while clumps C and D can be well fit by one component. The lower right and left panels of Figure 2.2 compare the spectra and one-component Gaussian fits of the [SII] emission lines for clumps A and B, with regions selected by the method described in 2.3. For clump A, [SII]λ6716/[SII]λ6731 = 0.7 +/- 0.1, while for clump B, = 1.2 +/- 0.3, corresponding to electron densities of 1800 $\pm$ 1000 and 290 $\pm$ 300 cm^{-3}, respectively (Osterbrock 1989). The grey hatched lines in all figures show the wavelength range of strong sky OH emission features. The central panel is an Hα map of ZC406690, with each region outlined.

component peak, which indicates that a large fraction of the Hα flux from this region comes from an outflowing wind. The emission line profile for [OIII] is very similar to that for Hα, such that the clump A [OIII] line is slightly less broad than Hα, but for clump B, both lines are equally broad, with the asymmetric blue line wing also present for [OIII]. However, we note that the aforementioned comparisons are done by eye since the S/N for the H-band spectrum for each clump is too low to perform a rigorous two-component fit. Since [OIII] and [OII] likely have similar kinematics, our choice of using Hα kinematics to fit the [OII] lines is thus supported.

We derive the local electron density of the clumps using the ratios of the [SII] and [OII] doublets. The lower right and left panels of Figure 2.2 compare the spectra and one-component Gaussian fits of the [SII] emission lines for clumps A and B, with regions selected by the method described in 2.3. For clump A, [SII]λ6716/[SII]λ6731 = 0.7 +/- 0.1, while for clump B, = 1.2 +/- 0.3, corresponding to electron densities of 1800$\pm$1000 and 290$\pm$300 cm^{-3}, respectively (Osterbrock 1989). These densities likely come from a combination of both the star-forming regions in the disk and high-density shocked filaments or clouds in the outflow, from which the emission lines originate. Since the clump+wind B region has a larger broad Hα flux fraction than the clump+wind A region, we would expect that more of the [SII] emission for clump B derives from the outflow than for clump A. Therefore, the observed clump A electron density of 1800 cm^{-3} is probably a better estimate for the dense clump environment, while the clump B density of 290 cm^{-3} is likely an average of clump gas and less dense outflowing cloud gas. The clump B estimate is similar to the value assumed by Kewley et al. (2001a) in their starburst models (350 cm^{-3}), which is based on the average density of individual HII regions from their sample observed with a 1 kpc slit. Since the densities calculated here are for the clump and the wind together, we do not use these values in our wind models.

Densities calculated from the [OII] doublet are much more uncertain (as the lines are mostly blended together in our spectra), and are only consistent (given the uncertainty) with the [SII] derived densities for clump B (see Table 2.2). This discrepancy could could be due to the two tracers probing different regions in the wind. The 1σ ranges quoted in Table 2.2 for both the [SII]– and [OII]–derived densities are obtained by adding and subtracting the uncertainties derived from the emission line fits to the ratio value and finding the corresponding electron densities from Osterbrock (1989).

We interpret the wind B region as the projection of an outflowing component onto a low-inclination disk ($\sim 20^o$ ($^{+10}_{-5}$), as estimated in Genzel et al. (2011)). Since regions adjacent to the clumps would have much lower Hα luminosity from star formation than the clumps, the broad emission from the winds can account for much more of the total signal. Furthermore, if we assume the outflow has a biconic geometry (Veilleux et al. 2005, and references therein), then the distant parts of the outflow will have a larger spatial extent than the clump, further separating this "wind" region from the clump in projection. This notion of viewing the wind in projection is consistent with the presence of less of an offset broad component for clump A, as it is likely younger than clump B (see section 2.4.2) and therefore has had less time to produce an extended wind. The relative outflow velocities from the two clumps further supports this view (with $v_{out,B} >> v_{out,A}$), as most outflow models (Heckman et al. 1990; Veilleux et al. 2005) predict increasing wind velocity with distance from the galactic plane.

We can use this model of a projected wind to learn about the geometry and structure of the outflow. The offset between clump B and wind B is $\sim$ 1.8 kpc, so with an inclination of 20^o, the average distance of the line-emitting outflow from the disk is $\sim$ 5.3 kpc. Given that the HWHM of the broad component of wind B is 340$\pm$15 km s^{-1} , then the average timescale of the line-emitting part of the wind is 15 Myr. It is likely that the gas in clump B has been forming stars for much longer than this given its average metallicity (see Table 2.2), but we are only observing the portion of the outflow coming from dense, hot filaments in the wind, and the older parts of the outflow may be too diffuse or faint to observe.

Table 2.2: Observed Properties of the Clumps

	Clump A	Clump B
E(B-V)[a] (Hα/Hβ)	0.493 $\pm$ 0.165	0.493$\pm$ 0.165
E(B-V) (SED)	0.33 $\pm$ 0.1	0.33 $\pm$ 0.1
[OII]λ3729/3726	1.38 $\pm$ 0.41	1.51 $\pm$ 1.14
n_e ([OII]) (cm^{-3})[b]	80, [1–100][c]	5, [1–1000][c]
[SII]λ6716/6731[d]	0.7 $\pm$ 0.1	1.2 $\pm$ 0.3
n_e ([SII]) (cm^{-3})[b,d]	1800, [1100–3000] [c]	290, [30-750][c]
[OIII]/Hβ[a]	6.72 $\pm$ 1.31	4.62 $\pm$ 10.30
[NII]/Hα[e]	0.11 $\pm$ 0.018	0.21 $\pm$ 0.029
[SII]/Hα[e]	0.18 $\pm$ 0.049	0.18 $\pm$ 0.067
[OII]/[OIII][e]	0.99 $\pm$ 0.14	1.06 $\pm$ 0.35
U (from O_{32}) (cm^{-1})[a,g]	5.50x10^7, [4.75x10^7–1.1x10^8][c]	8.75x10^7, [3.75x10^7–1.2x10^8][c]
U (from O_{32}) (cm^{-1})[f,g]	...	1.03x10^8, [4.50x10^7–1.25x10^8][c]
SFR ($M_\odot$ yr^{-1})[f]	40 $\pm$ 12	11 $\pm$ 3.3
$r_{out,HWHM}$ (kpc)[f]	0.8 $\pm$ 0.3	1.2 $\pm$ 0.5
U (from SFR) (cms^{-1})	7.4x10^7 $\pm$ 6.1x10^7	8.3x10^7 $\pm$ 1.0x10^8
12 + log10(O/H)[h]	8.42 $\pm$ 0.12	8.62 $\pm$ 0.096

[a] For clump B, these numbers are estimated assuming Hα/Hβ is the same for clumps A and B.
[b] n_e is calculated from Osterbrock (1989) assuming collisional de-excitation with $T_e = 10^4$ K.
[c] 1σ range
[d] from Genzel et al. (2011)
[e] For regions including both the clump and the wind which are spatially consistent among H, J, and K-band cubes.
[f] For clump B, assuming Hα/Hβ is the same as for the diffuse gas.
[g] For this calculation, metallicities are assumed to be those as calculated using the combined method of Kewley & Dopita (2002).
[h] Using the [NII]/Hα conversion of Denicoló et al. (2002).

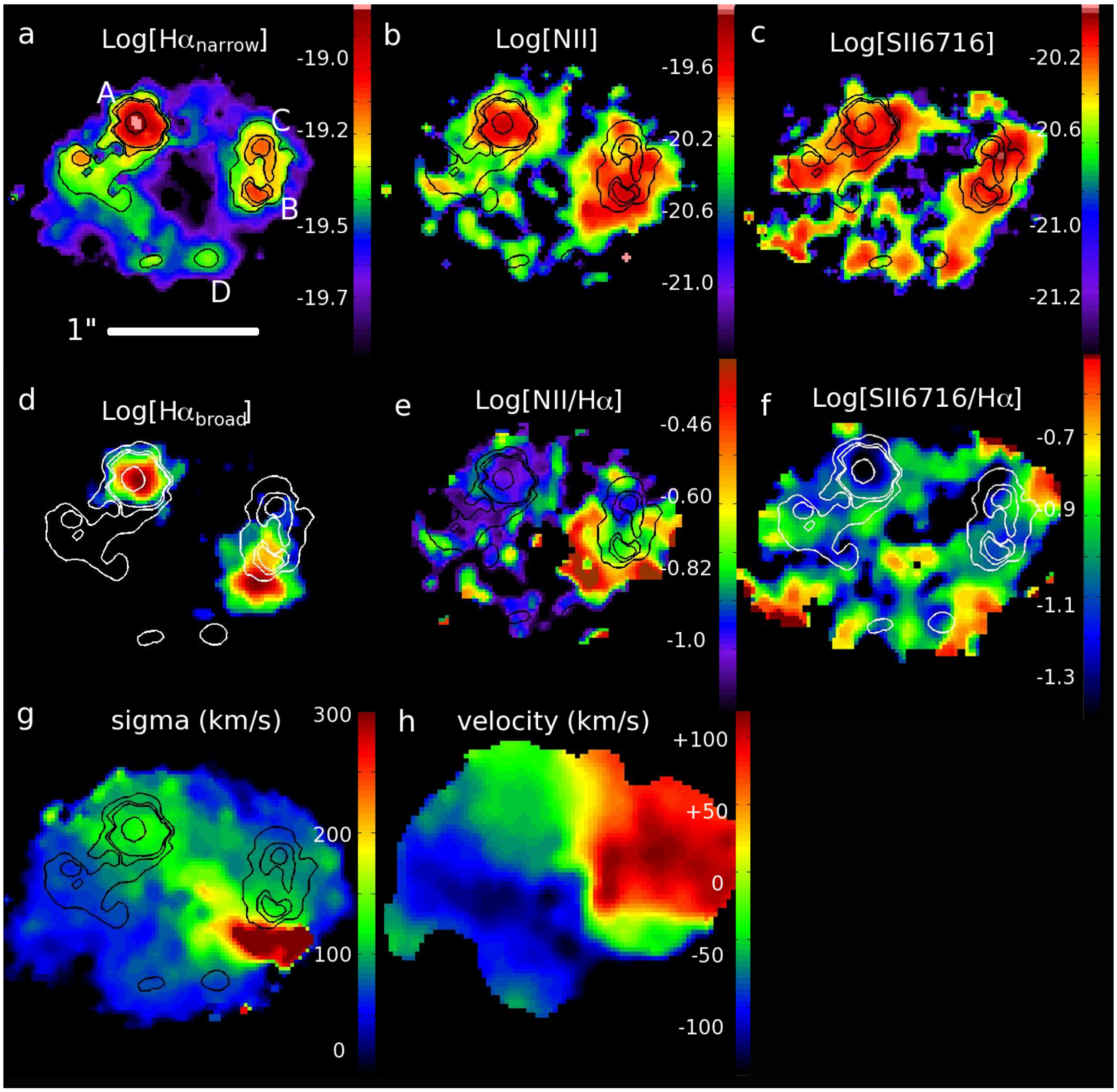

Figure 2.3: Spatially-resolved emission line maps for (a) log[Hα narrow], (b) log[[NII]λ6584], (c) log[[SII]λ6716], (d) log[Hα broad], (e) log[[NII]/Hα], (f) log[[SII]λ6716/Hα], (g) the Hα dispersion and (h) the Hα velocity field. The top three panels show the velocity-integrated flux and have a S/N per pixel (for the un-resampled maps with 0.05" pixels) near the clumps of 100-200, 10-40, and 10-40, respectively. [SII]λ6731 is not shown since it is affected by an OH sky line. All of the maps are rebinned by two pixels and smoothed by 3 pixels for the purpose of presentation and are overlaid with Hα intensity contours to highlight the locations of clumps A, B, C and D (labeled in panel a). The rebinning does not change the overall appearance of the maps as the S/N is very high, but merely accentuates features that are already present before rebinning. The spatial resolution of these maps is 0.2". From panels (d), (e), and (f), we find that broad emission surrounding clump B is spatially correlated with shock-like [NII]/Hα and [SII]/Hα ratios, indicating an energetic wind coming from the clump.

2.3.3 Broad Emission is Spatially Correlated with Shock-like Emission Line Ratios

Figure 2.3 shows spatially-resolved emission line maps for Hα, [NII]λ6584 and [SII]λ6716, which illustrate the effect of the outflowing gas on the region surrounding the clumps. The peak in [NII]λ6584 emission is located near the peak of Hα emission over the clumps but the [NII] emission is more extended around clump B than the Hα emission (by ∼1 kpc). This effect is seen even better in the ratio map of [NII]/Hα located in panel e of Figure 2.3. There is a semi-circle like structure centered on clump B that peaks in [NII]/Hα over the broad-line region, with an enhancement of about 80% from the clump value (see Table 2.1). The same effect is seen around clump A with a smaller enhancement. Errors for the different regions are over an order of magnitude lower, such that the uncertainty ∼ 2-5% on and near the clumps. These enhanced values of the [NII]/Hα ratio can be indicative of both higher metallicity and evidence of shocks and AGN (e.g. Dopita & Sutherland 1995). We previously discussed why an AGN explanation is unlikely in Section 2.3.2.

We can somewhat disentangle the effect of metallicity and shocks on the [NII]/Hα ratio by examining other emission line ratios and comparing the data to shock and photoionization models from the literature. Both the [SII]λ6716+6731/Hα and [OIII]/Hβ ratios are much more sensitive to the ionization parameter (and thus shocks) than to metallicity, in the metallicity regime of the clumps.

The [SII]λ6716 map (panel c) shows that much of the emission is located on or near the clumps, although it does not follow the Hα emission very closely. Panel f shows a map of [SII]λ6716/Hα, which serves as a lower limit for [SII]λ6716+6731/Hα which is omitted due to the aforementioned OH sky lines. Even with this underestimate, we see slightly higher ratios surrounding the clumps than over their centers (0.059 vs. 0.087 for clump A and 0.11 vs. 0.14 for clump B). This is consistent with the notion that the larger [NII]/Hα ratios are caused by shocks (and possibly also photoionization from star formation) as opposed to sharp metallicity gradients. The typical uncertainty for the [SII]λ6716/Hα ratio near the clumps is 5-10%, although the S/N drops off sharply away from the clumps.

It is possible that there is some variation in the [SII]λ6716/6731 ratio between the clump and wind regions that we are unable to measure because of the OH sky lines, and we have considered the scenario in which this variation could compensate for the gradient of [SII]λ6716/Hα from the clump to wind regions, thereby erasing the overall [SII]/Hα ratio gradient. However, if we calculate the variation in the [SII] ratio required to erase the [SII]/Hα gradient and assume the clump region has the observed value of the ratio, we get implausible values for the [SII] ratio of the winds, 1.6 for the clump A wind and 2.5 for the clump B wind, which are inconsistent with the collisional de-excitation model at 10^4 K from Osterbrock (1989). Thus the gradient in [SII]λ6716/Hα between the clump and wind regions implies a similar gradient in [SII]λ6716+6731/Hα, which cannot be washed out by density variations.

This region of enhanced emission line ratios surrounding clump B is spatially correlated with the bulk of the broad Hα emission, which we ascribe to an outflowing component. From the broad Hα map (Figure 2.3 panel d), it is evident that most of the broad emission comes from directly over clump A and to the SE of clump B, coinciding with the enhanced [NII]/Hα and [SII]/Hα ratios. This broad region near clump B, from which we extracted the 'wind B' spectrum, not surprisingly also shows up as a peak in the velocity dispersion in panel g, and is blueshifted relative to clump B, as seen in the velocity map (panel h). The latter statement is confirmed by examining the line centers of the narrow components for clump B and wind B. The kinematic maps are derived by fitting a single Gaussian component to the Hα line (for more on this see Genzel et al. (2011)). Thus, if active star formation in the clumps produces a large-scale, energetic outflow, this could explain both the broad emission lines and the enhanced emission line ratios in this region.

In order to visualize the emission line gradients around clump B and understand their errors, we show the average flux across a swath of the emission line maps with a slit width of 0.2" in Figure 2.4. This figure shows that there is a relative increase in emission for both [NII], [SII] and Hα broad relative to Hα narrow around clump B with errors from the noise cube that are much smaller than these gradients, and thus the emission line gradients seen in Figure 2.3 near clump B are real. While the errors increase dramatically for [SII]/Hα near the edge of Figure 2.4, the gradient is seen clearly near clump B where the S/N is relatively high. The Hα broad emission is calculated as described in Section 2.2.2 using a two-component fit to the Hα line.

In Figure 2.5, we show the emission line maps for [OIII], Hβ, and [OII]. As is clear from the first and last panels, the [OIII] and [OII] emission is coincident with the location of the clumps. Even with the final smoothing (see Section 2.2.2), the S/N in individual pixels for Hβ is very low, and thus only a small region near clump A remains after the S/N = 3 clipping. Fortunately, the Hβ line in the integrated spectrum for clump A has a S/N ratio ~ 5, and we are able to use this to derive [OIII]/Hβ ratios for the clumps.

Figure 2.6 shows the BPT diagram (Baldwin et al. 1981) with SDSS data from the latest DR7 release (Adelman-McCarthy & et al. 2009) along with the data for clumps A and B, to compare the latter to local star-forming galaxies and other high-z galaxies. Since the clump A and B data points use both high-resolution K- and low-resolution H-band data, we extract larger regions, which contain both the 'clump' and 'wind' regions. We are unable to get a direct measurement of the Hβ line for clump B, as it is shifted onto an OH sky line in that part of the galaxy, but we estimate the clump B Hβ value assuming a constant Hα/Hβ ratio for the clump regions (Hα/Hβ= 5.1 as measured from clump A). The position of the clump B point is therefore much more uncertain, and the lower error bar for [OIII]/Hβ extends off the figure. The errors come from the uncertainty of the fits to the emission lines. Clumps A and B fall in the ÒcompositeÓ region of the BPT diagram that is generally occupied by starburst and high-z galaxies, which are generally found to have higher SFRs, densities and ionization parameters than normal SFGs and HII regions (Shapley et al. 2005; Erb et al. 2006b; Liu et al. 2008; Brinchmann et al. 2008). Their offset could also be due to shocks, AGN, or a different N/O ratio. As the clumps occupy the same parameter space as these galaxies, it appears that their star-forming regions more closely resemble those of starbursting galaxies than of HII regions in normal local SFGs.

In order to differentiate the effects of metallicity, ionization parameter, and the contribu-

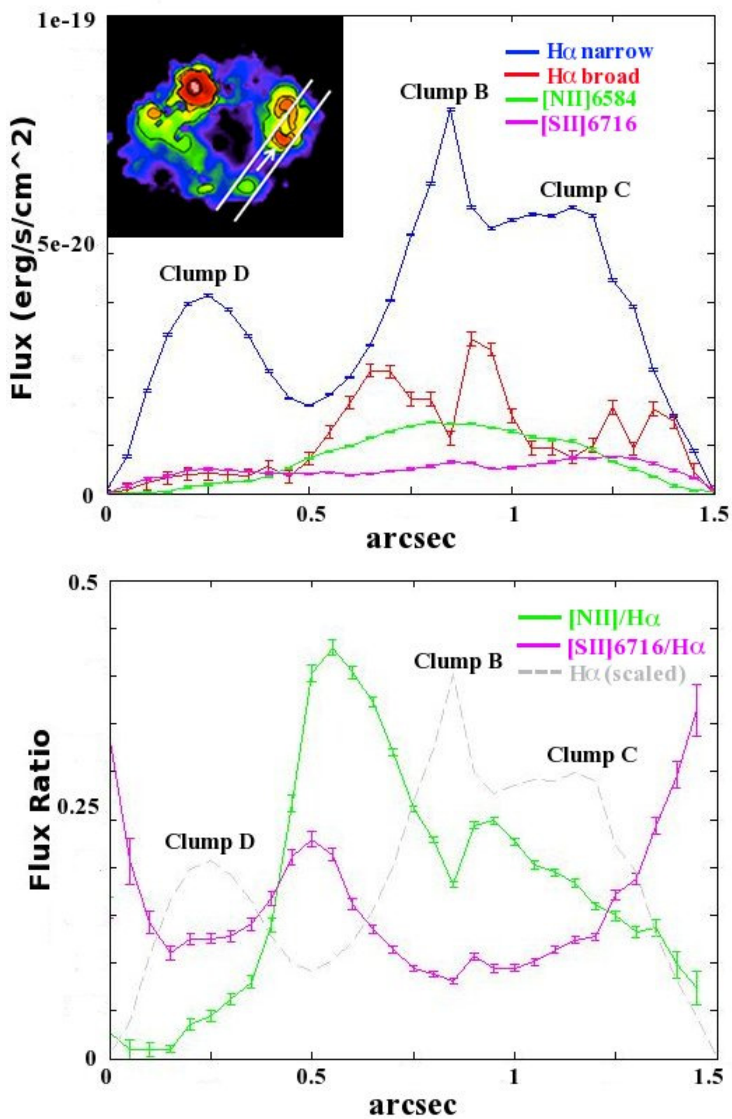

Figure 2.4: Averaged flux of several emission lines and ratios along a four pixel-wide (0.2") swath of the galaxy moving from clump D to B to C. (a) Average flux of Hα narrow, Hα broad, [NII]λ6584 and [SII]λ6716, along with error bars from the noise cube. (b) [NII]/Hα and [SII]λ6716/Hα and error bars from the noise cube with Hα narrow scaled in the background for reference. There is a relative increase in emission for both [NII], [SII] and Hα broad relative to Hα narrow around clump B and the errors are much smaller than these gradients. For [NII]/Hα, [SII]/Hα and Hα broad, the gradients from the peak of emission (or the peak of the ratio) to the minimum (near the clump B center) are over 10σ. The inset in the upper left corner of (a) shows the width, location and direction of the swath.

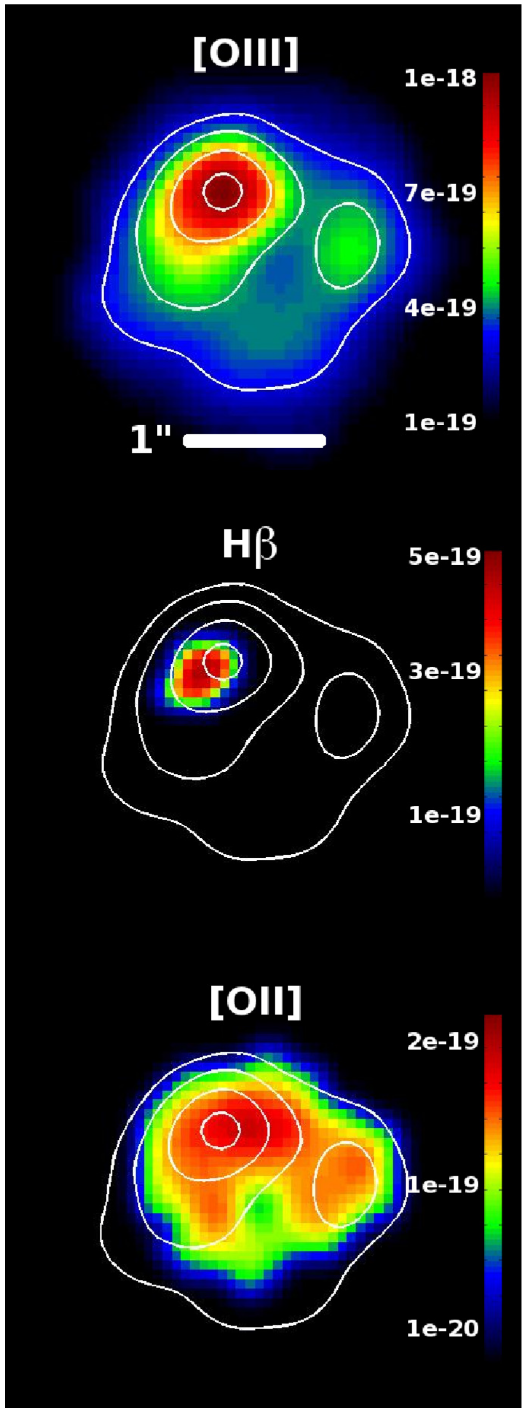

Figure 2.5: Spatially-resolved emission line maps for (top to bottom) [OIII], Hβ, and [OII]. The maps have been smoothed by 3x3 pixels to enhance the S/N and then clipped by S/N = 3. The maps were then rebinned by 2 spatial pixels and smoothed again by 3 pixels for the purpose of presentation. The white contours trace the [OIII] flux. The un-resampled cubes have 0.125" pixels and a PSF FWHM of 0.6".

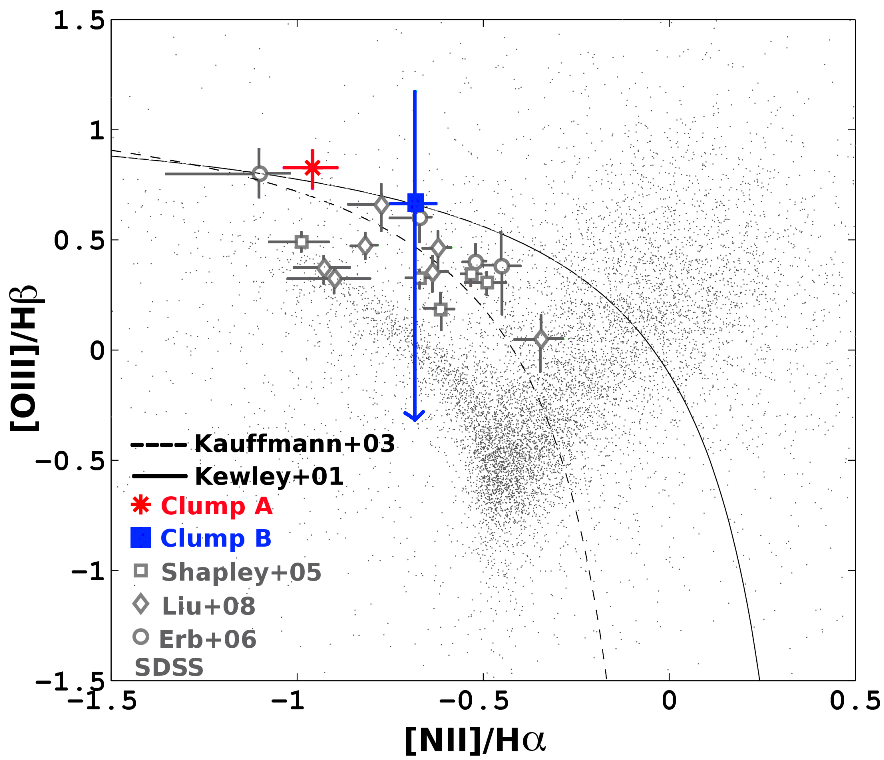

Figure 2.6: The BPT diagram including data from several high-z galaxies along with the clumps from ZC406690. Clumps A and B are shown as a red asterisk and blue square, respectively. The lower error bar for clump B extends beyond the figure boundaries. Other high-z data is shown as grey squares (Shapley et al. 2005), circles (Erb et al. 2006b), and diamonds (Liu et al. 2008). A subset of SDSS galaxies are shown in grey with the empirical AGN/HII boundary as the dashed line from Kauffmann et al. (2003) and the theoretical boundary as the solid line from Kewley et al. (2001b). The clump data points fall in the region offset from the main HII branch that is also occupied by other high-z galaxies and many local starbursts (as shown by Liu et al. 2008; Brinchmann et al. 2008).

tion of shocks, we compare our data to photoionization and shock models from Rich et al. (2011) and photoionization models from Levesque et al. (2010). These photoionization models are similar in many respects: they are both created with the codes Starburst99 (Leitherer et al. 1999) and Mappings III (Sutherland & Dopita 1993), use the same evolutionary tracks and both assume continuous star-formation histories, but they also differ somewhat in terms of model atmosphere, geometry and IMF. Although the Rich et al. (2011) shock models are for slow shocks (up to 200 km s^{-1}), they sample a large portion of the parameter space (in terms of metallicity and ionization parameter) which fits our observations, and the exact velocity of the shocks do not qualitatively effect our conclusions since there is a much bigger difference between photoionization and shock models than slow vs. fast shocks in terms of emission line ratios. While evidence for shocks indicates the presence of an outflow, emission from both shocks and photoionization could be present in a wind.

Figure 2.7 shows our data from the clump and wind regions as well as the photoionization and shock models in the [NII]/Hα vs. [SII]/Hα plane (with [SII]/Hα calculated as described in section 2.2.3), with varying metallicity, ionization parameter and shock velocity. We are able to get data for both the clump and wind regions here as we are only using the high-resolution K-band data while we could only get overall clump regions with lower resolution for Figure 2.6 since we used lower-resolution H-band data in addition to K-band. Thus the clump regions in Figures 2.6 and 2.7 cover different spatial areas and therefore they have emission line ratios with slightly different values. We also note that, as for Figure 2.6, the error bars come from the uncertainty in the emission line fits and are therefore larger than the error bars shown in Figure 2.4, which are derived from the noise cube.

The two photoionization models shown in Figure 2.7 (Rich et al. 2011; Levesque et al. 2010) are roughly the same for [O/H] = 8.39, however, the [O/H] = 8.69 line is offset to much larger values of the [NII]/Hα ratio for the Levesque et al. (2010) model. This is likely due to one of the differences between the models mentioned above. At first glance, the data points seem to be well fit by the photoionization-only models. Both wind regions appear to fall near the same metallicity line as their respective clumps, but offset to higher emission line ratios, indicating a lower ionization parameter. However, we can independently calculate the ionization parameter for the clumps, and compare that to the ionization parameter implied by the photoionization models.

We calculate the ionization parameter for the clumps using two different methods: 1) Using the O_{32} diagnostic with metallicity-dependent fitting curves based on Kewley & Dopita (2002) and 2) using the observed Hα luminosity and calculated electron density as follows:

$$U = \frac{Q}{4\pi r_0^2 n_e} \tag{2.1}$$

where Q = $L_{Lyc}/h\nu_{Lyc}$ is the rate of ionizing photons, L_{Lyc} = 16x$L_{H\alpha}$ (as given by Osterbrock 1989), r_0 is taken as the clump HWHM, and n_e is the electron density calculated from the [SII] doublet. The results are shown in Table 2.2 and the range of ionization parameters (for the corresponding metallicities), is denoted by the thick black lines in Figure 2.7. These ionization parameters are 3-10 times higher than those predicted from the

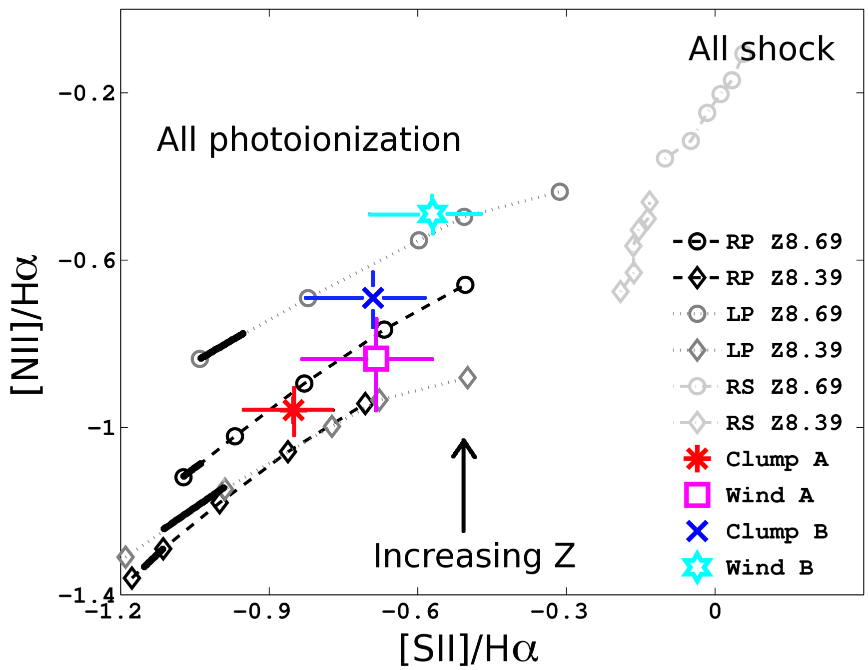

Figure 2.7: The [NII]/Hα vs. [SII]/Hα plane with data from the clump and wind regions as well as the photoionization and shock models (with [SII]/Hα calculated as described in section 2.2.3). The data are shown as a red asterisk, a purple square, a blue 'x' and a cyan star with error bars (for clump A, wind A, clump B and wind B, respectively). The Rich et al. (2011) and Levesque et al. (2010) photoionization and shock models are shown as the black and grey lines. The darkest/dashed lines are the Rich et al. (2011) photoionization models (RP), the medium/dotted lines are the Levesque et al. (2010) photoionization models (LP) and the lightest/dash-dot lines are the Rich et al. (2011) shock models (RS). Open circles denote the models with O/H = 8.69 and open diamonds denote models with O/H = 8.39. For the photoionization models the points along the line represent a varying ionization parameter, increasing to the left (logU = 7–8). For the shock-only models, the points along the line vary in shock velocity, increasing upward (v = 100–200 km s^{-1}). The solid black lines indicate the ionization parameter range for each metallicity line as calculated in section 2.3.3. These measured ionization parameters are offset from those implied by the photoionization-only models, indicating a shock contribution to the emission.

photoionization-only models of Rich et al. (2011) and Levesque et al. (2010). The data points appear to be offset towards the shock-only models, and are perhaps better fit by a model with contributions to the emission from both photoionization and shocks. In fact, if we compare the [NII]/Hα and [SII]/Hα ratios for the clumps along with the corresponding ionization parameters with Figure 2.10 from Rich et al. (2011), which shows the photoionization + shock models, we find that the clumps and their winds are best fit by models with some shock contribution. The clumps are well fit by models with $5 \pm 5\%$ and $10^{+10}_{-5}\%$ shock contribution to the nebular emission (for A and B), and the wind regions are well fit by models with $15^{+25}_{-15}\%$ and $30^{+30}_{-20}\%$ shocks, where the error bars come from fitting the 1σ values of the ionization parameter and emission line ratios to the models. Thus the data are also consistent with no shocks for the wind from Clump A.

Based on the offsets from the observed ionization parameters, it is reasonable to assume that the elevated emission line ratios in the wind regions compared to the clumps are due to a larger contribution to the flux by shocks, and that the offset of the clumps in the BPT diagram from normal SFGs is due in part to shocks generated by star formation feedback. The highly turbulent, fast outflows emanating from the clumps could easily produce shocks as the hot superwind fluid collides and mixes with cooler ISM gas.

2.4 Discussion

2.4.1 Properties of the clumps and their outflows

Based on the observed properties of the clump A and B winds, we can perform simple calculations to better understand the structure of these outflows and their relationship to local and high-z galactic-scale superwinds. For the following calculations, we use the SFRs, gas masses and mass outflow rates as calculated in Genzel et al. (2011). The SFR was calculated from the Hα flux using the Kennicutt (1998) calibration adjusted for a Chabrier IMF with the extinction correction described in Section 2.3.1.

The gas masses were derived from the SFRs using the Schmidt-Kennicutt relation as given in Genzel et al. (2010). There are systematic errors that arise from this calculation due to (1) scatter in the intrinsic relation, (2) the varying slope and zero point of the relation as quoted by different authors, (3) the extrapolation of the relation from low-z to high-z, and (4) the application of the relation on ∼kpc scales. We address each of these issues in Appendix A, and ultimately derive an overall systematic uncertainty for the gas masses of the clumps of +0.3/-0.8 dex.

The mass outflow rates were calculated assuming an outflow of warm ionized gas into solid angle Ω with radially constant outflow rate and velocity as derived in Genzel et al. (2011) and are quoted in Table 2.3. Details of the model are discussed in Appendix B. We note that for our outflow model, we only calculate the mass and mass outflow rate of the warm ionized component of the wind, and thus our numbers are lower limits.

The Winds from Individual Clumps Are Very Massive and Energetic

From our mass outflow rate derivation, we also obtain the mass of the warm ionized component in the wind (M_w) for each clump. We estimate the energy of the wind as $E_w = \frac{1}{2} M_w \text{x } v_{out}^2$, where v_{out} is the maximum outflow velocity determined from the width of the Hα emission line (see Table 2.3). Using an average wind velocity instead would only change E_w by a factor of 2 and will not affect any of the forthcoming conclusions.

We find that the mass and energy in the outflows of individual clumps lies in the range 1–2x10^8 $M_\odot$ and 3–7x10^{56} ergs, several times greater than what is observed in the warm component from entire ULIRG and dwarf starburst galaxies ($M_w \sim 10^{5-7}$ $M_\odot$ and $E_w \sim 10^{53-55}$ ergs) based on numbers compiled by Veilleux et al. (2005). We caution that our measurements must be carefully compared to those of local starbursts, as the mass estimates are strongly dependent on the extinction corrections used and the quoted local starburst energy estimates are taken from dwarf starbursts and spiral galaxies, which likely produce less energetic winds than ULIRGs.

The main point that should be gleaned from this section is that these clump-scale outflows are massive and very energetic even by local starburst standards.

Are the Outflows Energy or Momentum Driven?

Galactic-scale outflows are considered to be driven either by the energy released from supernovae and the UV luminosity from stars (McKee & Ostriker 1977; Matzner 2002) or through momentum transport by radiation pressure on dust and the momentum from stellar winds and supernovae (Murray et al. 2005, 2010). Momentum-driven winds tend to dominate in dense regions where much of the energy is radiated away, but the momentum remains (Murray et al. 2005). Murray et al. (2005) make several predictions for what one would expect given energy- or momentum-driven outflows from star-formation feedback in terms of $\dot{M}_{\rm out}$(the mass outflow rate), $\dot{p}_{\rm out}$(the momentum outflow rate) and η (the mass loading).

For a starburst in which 90% of the supernovae (SN) energy is radiated away, Murray et al. (2005) predict that $\dot{E}_{\rm SN,out} \sim 10^{-3} L_{bol}$, as 1% of the total luminosity released throughout a star's lifetime is ejected in the supernova, and 10% of the supernova energy is not radiated away. Thus, assuming the supernovae energy goes into the wind, $\dot{E}_{\rm wind}/L_{bol} \sim 10^{-3}$. For the clumps, we find that

$\dot{E}_{\rm wind}/L_{bol} \sim \frac{1}{2} \dot{M}_{\rm out} \text{x } v_{out}^2 \ / \ L_{bol} = 0.005$ and 0.05 with ranges of 7.6x10^{-5}–0.05 and 0.0002–0.3 for clumps A and B respectively.

Thus for a feedback efficiency of 10%, the clump A wind could just barely be explained by an energy-driven model. However, the clump B wind is inconsistent with a purely energy-driven wind unless none of the SN energy is radiated away. If however, the extinction in clump B is much greater than for clump A, L_{bol} from the disk would be underestimated more than $\dot{M}_{\rm out}$, which is coming from gas that is farther from the disk. This could lower $\dot{E}_{\rm wind}/L_{bol}$

for clump B, bringing it closer to a number that could be explained by energy-driven winds. In addition, the large error bars for these quantities (mostly derived from the large error in $\dot{M}_{out}$) do make them roughly consistent with the model, although due to the fact that $\dot{M}_{out}$ is likely an underestimate, the results are more likely skewed to larger values of $\dot{E}_{wind}/L_{bol}$.

For a purely momentum-driven wind, Murray et al. (2005) predict that $\dot{p}_{wind}/P_{rad} \sim 1$, and we find that

$\dot{p}_{wind}/P_{rad} \sim \dot{M}_{out}$x $v_{out}/$ $(L_{bol}/c) = 6$ and 30 with ranges of 0.5–65 and 2–245 for clumps A and B respectively.

This result indicates that clump A can also be explained by a momentum-driven wind, but clump B cannot ($\dot{p}_{wind}/P_{rad} = 30$), although again, the large error bars make this conclusion somewhat uncertain.

There are many factors that could be biasing this measurement. First, as mentioned in Genzel et al. (2011), our outflow velocities could be too high by a factor of 2, depending on the definition chosen for the maximum outflow velocity. Second, in an optically thick medium, the total effect of radiation pressure could be greater by a factor of $(1+\tau_{IR})$ due to multiple scattering of infrared photons, although it will likely not exceed a factor of a few. These two effects will bring down the value of $\dot{p}_{wind}/P_{rad}$. On the other hand, our mass outflow rates could be underestimated, both as a result of only including the warm ionized component of the wind and also due to overestimated wind densities (see next section), and this would mean our momentum wind efficiency is too low. These uncertainties are represented in the large systematic errors for $\dot{p}_{wind}/P_{rad}$.

Our results suggest that the clump A wind could be either energy- or momentum-driven but that the clump B wind is harder to explain by either driver. However, it is possible that current models do not fully encapsulate the physics in these extreme high-z star-forming regions. In the next section we further compare the relative contributions to feedback by SN and radiation pressure using the Ostriker & Shetty (2011) model. We note that Murray et al. (2005) predict that in both energy and momentum driven outflow models, the mass loading factor ($\eta = \dot{M}_{out}/SFR$) ~ 1 and this is roughly consistent with our observations ($\eta = 3$–8). Similarly, Hopkins et al. (2012) predict mass-loading factors in star-formation driven winds of 0.5–2. We compare these results to those of other high-z galaxies and local starbursts in Section 2.4.3.

The Source of the High Velocity Dispersions

We also investigate the pressure balance in the star-forming clumps to determine whether star-formation feedback is a viable source of the large velocity dispersions seen throughout the galaxy and by extension, in other high-z galaxies. We calculate the contributions to the gas pressure from the weight of the gas at the midplane (P_{weight}), from star-formation generated turbulence (P_{turb}), from radiation pressure (P_{rad}) and from the observed velocity dispersion (P_{kin}) from the model of Ostriker & Shetty (2011), hereafter OS11. The model of OS11 is based on the assumption that in equilibrium, the weight of the gas balances the pressure from feedback. In the model, there are two different regimes defined by the surface density, where the feedback is either dominated by turbulence or radiation pressure; turbulence dominates in the galactic center from $\Sigma_{gas}\sim$ 100–10^4 $M_\odot pc^{-2}$, and radiation pressure takes over for $\Sigma_{gas}>10^4$ $M_\odot pc^{-2}$. The pressures are defined as follows:

$$P_{kin} = \rho_0 \sigma_z^2 \tag{2.2}$$

$$P_{weight} = \pi G \Sigma^2/2 \tag{2.3}$$

$$P_{turb} = \frac{f_p}{4}\frac{p_*}{m_*}\Sigma_{SFR} \tag{2.4}$$

$$P_{rad} = \epsilon c \kappa_{IR} \Sigma \Sigma_{SFR}/4 \tag{2.5}$$

where ρ_0 is the midplane density (which we take as the electron density), σ_z is the observed (narrow-line) velocity dispersion, Σ and Σ_{SFR} are the surface densities of gas and the SFR, f_p is a factor of order 1-2 which describes the strength of turbulent dissipation, p_*/m_* is the mean momentum injected by SN per unit mass of stars formed (which we take as 3000 km s^{-1}, following OS11), ϵ is the mass-to-radiation conversion efficiency from stars (which we take as 6.2×10^{-4}, following OS11) and κ_{IR} is the mean opacity (which we take as 10 $cm^2 g^{-1}$, following OS11).

From these calculations, we find that for clump A, P_{kin} balances P_{weight}, as proposed by OS11, and that $P_{turb}\sim P_{rad}$ (see Table 2.3 for details). This latter finding is consistent with the fact that clump A is close to the boundary between the turbulent and radiation pressure dominated regimes defined by OS11, with $\Sigma \sim 8000$ $M_\odot pc^{-2}$. However, our results are inconsistent with the OS11 model in that $P_{turb} + P_{rad} < P_{kin}$ (by about an order of magnitude, even with the errors), meaning that the pressure generated from star-formation feedback, both from SN and radiation pressure, does not fully account for the observed turbulence in the disk. This result also follows from applying equation 22 of OS11 to the star-formation efficiency derived from Genzel et al. (2010) of 0.017, wherein the OS11 model predicts an observed velocity dispersion of 19–37 km s^{-1} (where the range reflects the the choice of f_p), while we observe dispersions of 50–100 km s^{-1}.

This issue of the source of the high dispersions in high-z galaxies has been explored by several authors (Genzel et al. 2008, 2011; Green et al. 2010; Law et al. 2009; Epinat et al. 2009; Kassin et al. 2007; Burkert et al. 2010) with no consensus yet reached concerning the dominant mechanism. Our conclusions on this matter are dependent on the exact choice of parameters used, on the uncertainty in our observations, and on the method applied to derive the intrinsic dispersion (Davies et al. 2011). However, we are fairly confident in our calculation of P_{kin}, as the midplane density that we derive from the [SII] doublet is roughly consistent with what is observed in dense star-forming regions in other galaxies (Kewley et al. 2001b), and several authors have found that the high velocity dispersions observed from Hα in z $\sim$ 1-2 galaxies is consistent with the dispersions in molecular gas as observed from CO; for example Tacconi et al. (2010, 2013) for normal SF-galaxies and Tacconi et al. (2008) and Engel et al. (2010) for SMGs.

For clump B, we find slightly different results. As for clump A, P_{turb}+ P_{rad}<P_{kin}, but unlike for clump A, P_{kin}>P_{weight} and P_{turb}>P_{rad}. We note that the first two relations are less significant than for clump A since the errors are much higher as a result of the more uncertain electron density measurement. The fact that P_{turb}>P_{rad} can be explained by the lower surface density of clump B (1200 $M_{\odot}pc^{-2}$) which falls squarely in the turbulence-dominated regime (100–10^4 $M_{\odot}pc^{-2}$). The results from these calculations support the claim of OS11 that the weight of the gas balances the turbulence in the disk, which suggests a self-regulatory mechanism for SF feedback. However, we find that while SF feedback does contribute to the observed turbulence it cannot fully account for it. Roughly 85–90% of the velocity dispersion remains unaccounted for and must have some other source, such as clump-clump interaction, clump-stream interaction, or the release of gravitational energy as gas or clumps fall inward.

The Outflow Can Escape the Disk of the Galaxy

To test whether or not the outflow can escape the plane of the galaxy, we compare the pressures derived from the OS11 model with the ram pressure in the wind:

$$P_{ram} = \rho_w v_{out}^2 \tag{2.6}$$

where ρ_w is the density in the wind and is somewhat uncertain. Genzel et al. (2011) adopted a value of 100 cm^{-3} based on [SII] doublet observations of local outflows from Heckman et al. (1990) and Lehnert & Heckman (1996). However, more recent work has shown that the actual density of the warm ionized component in superwinds could be almost 2 orders of magnitude lower (Cecil et al. 2001). Using the larger density estimate (100 cm^{-3}) for clump A, P_{ram} $\sim$ P_{weight}, which suggests that the wind would barely be able to break out of the plane of the disk, while for the lower density estimate (4 cm^{-3}), P_{ram} << P_{weight}. The situation is reversed for clump B which has a more evolved and therefore faster wind (see models by Heckman et al. (1990) which suggest that winds become faster with increasing radius), such that both density estimates yield P_{ram} >> P_{weight}. In this case, the wind would have no trouble escaping the disk.

Alternatively, we can estimate the wind density by assuming that P_{ram} balances P_{weight}. With the pressures calculated as before, we get n_{wind} = 67 $\pm$ 74 cm^{-3} for clump A and 0.4 $\pm$ 0.5 cm^{-3} for clump B. This result is consistent with clump B having a more extended and therefore more diffuse outflow.

We can also test whether or not gas can escape the galaxy by comparing the outflow velocities of the clump winds with the escape velocities of the clumps and the galaxy. This test is physically the same, but uses measurements obtained independently. At the distance of the clump HWHM and estimating the clump mass as 2 x M_{gas} (assuming half of the clump mass is in stars), we find that for clumps A and B v_{out}/v_{esc} = 0.75 $\pm$ 0.39 and 2.4

± 1.3, respectively. Therefore, some of the warm ionized gas could escape the gravitational potential of the clumps. In fact, some of this material could escape the galaxy as well since $v_{out}/v_{esc,galaxy} = 0.54 \pm 0.26$ and 0.99 ± 0.48 for clumps A and B. Thus analysis of both the ram pressure of the wind and v_{out}/v_{escape} suggests that a significant fraction of the gas could escape the gravitational potential of the clumps distributing the warm ionized gas elsewhere in the galaxy and even into the IGM.

How Clumpy are the Clumps?

We can estimate the 'clumpiness' of the clumps (or a volume filling factor of high density molecular gas) using the observed electron density (from the [SII] doublet) and the calculated molecular surface density. This number can be compared to that for Milky Way GMCs and central starburst regions to better understand how the star-forming regions are distributed within the clumps. We define it as follows:

$$clumpiness = \frac{n_{avg,H_2}}{n_{local,H_2}} = \frac{\Sigma}{4/3 r_{cl} \mu m_h} \frac{1}{n_{H_2}} \quad (2.7)$$

$$n_{H_2} = n_{HII} \frac{T_{HII}}{T_{H_2}} \quad (2.8)$$

where the latter equation is simple thermal pressure balance to obtain the density in the colder molecular gas from the hotter ionized gas, and n_{HII} is the local electron density derived from the [SII] doublet. We note that this thermal pressure balance gives us an upper limit for the molecular density since it neglects any non-thermal pressure due to turbulent cloudlet motion, which would likely be more similar for the ionized and molecular phases. A volume filling (clumpiness) factor of 1 would mean that the high density star-forming gas occupies all of the volume of the clumps, whereas a factor of 0 would mean it takes up none of the volume. We set $T_{HII} = 10^4$ K and $T_{H_2} = 30$ K (Elbaz et al. 2011; Hwang et al. 2011) to obtain $n_{H_2} = 6\text{x}10^5$ and $1\text{x}10^5$ cm^{-3} for the clumps. For clumps A and B, we get volume filling factors of $3.7\text{x}10^{-4}$ and $2.3\text{x}10^{-4}$ with 1σ ranges of 0–$7.6\text{x}10^{-4}$ and 0–$6.3\text{x}10^{-4}$, respectively. If, however, we adopt the molecular density found by Danielson et al. (2011) for a lensed $z \sim 2.3$ SMG of 10^4 cm^{-3}, we find much higher volume filling factors of 0.022 and 0.0023 for clumps A and B, respectively. These different values serve as our lower and upper limits for the volume filling factors of the clumps and are reflected in the errors (Table 2.3).

The volume filling factors based on the local electron density of the clumps are almost 2 orders of magnitude smaller than what we find in Milky Way (MW) GMCs. Assuming an average density ~ 100 cm^{-3} and a local/core density $\sim 10^4$ (Stahler & Palla 2005), then n_{avg}/n_{local} (MW) $\sim 10^{-2}$. Our clump estimates, however, are more similar to the volume filling factor in local starburst galaxies, based on models of M82. In the cloud-cluster starburst region model of Förster Schreiber et al. (2001), they estimate that clouds of molecular material are roughly 0.5 pc in radius surrounded by a layer of neutral and ionized gas up to 1 pc with a spacing of 2–7 pc between them. This gives an average volume filling factor of 3.6x10^{-3} for the cold molecular gas. This suggests that the star forming regions in the clumps are more concentrated than regions in both MW GMCs and starburst regions unless we adopt the Danielson et al. (2011) molecular gas density, in which case, our values are comparable to those from MW GMCs and local starbursts.

This should not be surprising as the molecular densities in the clumps are over an order of magnitude larger than what is found in star-forming cores in MW GMCs and the pressure in the disk (as seen in 4.1.3 and Table 2.3) is several orders of magnitude larger than what is found in the MW (P $\sim 10^{-10}$ ergs cm^{-1}) and is more comparable to the pressure in local ULIRGs (P $\sim 10^{-7}$ ergs cm^{-1}) (Downes & Solomon 1998). Thus, the clumps more closely resemble starburst regions in ULIRGs than MW GMCs, both in terms of physical properties and spatial distribution of dense gas. This result implies that the very large SFRs of the clumps are not because a higher fraction of the volume is involved in star-formation (in fact less volume is forming stars than for MW GMCs), but because the regions that are forming stars have much higher gas fractions.

2.4.2 Do the Clumps Represent an Evolutionary Sequence?

In this section, we explore the evolution of the clumps through their winds and whether they could typify different stages in clump development and evolution. We have seen throughout this paper that while both clumps A and B are actively forming stars and produce powerful winds, their individual properties are quite different. Clump B contains more enhanced shock-like emission line ratios and broad emission spatially offset (and therefore further away) from the clump as well as larger line widths, both indicative of a more mature outflow. The clumps also differ in their volume and surface densities (clump A is denser). This could be the result of the expulsion of high density gas from star formation feedback from clump B or it could be due to the fact that the luminosity and density measurements from clump B include not only clump gas but a large amount of the more diffuse gas from the wind. Both explanations further support the presence in clump B of a more mature outflow, suggesting that clump B has been forming stars for a longer period of time and thus clump B is older than clump A.

This notion is supported by the difference in gas phase metallicity between the clumps as calculated from [NII]/Hα which suggests an age difference. We calculate how long it would take clump A to be as metal enriched as clump B (assuming the [NII]/Hα ratio reflects the abundance only and is unaffected by shocks as a simplification). Using the closed and leaky box models outlined in Erb (2008) (see Genzel et al. 2011, Appendix C), we find this timescale ranges from 170 Myr – 1.7 Gyr. If the value of [NII]/Hα is more strongly affected by shocks for clump B (as is suggested by Figure 2.7), then the resulting timescale would be reduced, but it is likely that at least some of the [NII]/Hα enhancement in clump B is due to a higher metallicity, and thus more mature clump.

Given that clump B is likely older than clump A, we estimate how long it would take a clump A like object to turn into clump B, which has half of the clump A M_{gas}, assuming that the clumps start out with roughly the same M_{gas}. Although the gas masses are uncertain by

70–85% due to the fact that the physical conditions in these ∼kpc size clumps could be very different from the galaxies from which we derived the KS relation, it is hard to imagine that the relative masses between the clumps would be that far off, given that the physics and CO to H conversion factor in both the clumps are likely similar. If all of the extra gas from clump A is turned into stars, this would take $\sim$ 200–700 Myr (with the range reflecting the SFRs of clumps A and B). However, if outflows are removing gas from the clumps as well, then this timescale is much shorter; with an η of 1, the timescale is twice as fast and with an η of 3 (corresponding to clump A), the timescale is four times as fast. In the previous section, we found that a significant fraction of the outflowing gas could be lost from the clumps and perhaps even the galaxy. Based on our finding that $\eta > 1$, the age difference between the clumps obtained from the SFR and M_{gas} is at most 350 Myr, and for this to be consistent with our results based on [NII]/Hα, shocks must play an important role in the emission. To put these timescales in context with other observational work, Förster Schreiber et al. (2011b) find clump ages at $z \sim 2$ of ∼25–500 Myr and Elmegreen et al. (2009a) find average clump ages at z∼1–3 of 100 Myr, but find some clumps as old as 1 Gyr. Using hydrodynamic simulations, Dekel & Krumholz (2013) have found that on average clumps spiral inwards by dynamical friction in 250 Myr, and that most of their clumps last that long, as do the long-lived clumps of Immeli et al. (2004a), Bouché et al. (2007), and Ceverino et al. (2012). On the other hand, Genel et al. (2012b) find that clumps are disrupted very quickly, in 50–100 Myr, when strong feedback is included.

We can also compare clumps A and B with C. Clump C has a similar flux and SFR as clump B, and the extended [NII] emission from clump B continues to the region around clump C, indicating that it is somewhat enriched from star-formation. However, clump C has a narrow Hα line profile compared to clumps A and B and has no indication of outflows. Perhaps clump C could be placed further down the evolutionary sequence of clumps A and B: it is declining from it's major episode of star formation and its outflows are too diffuse to be observed or are projected onto clump B due to the inclination of the galaxy.

2.4.3 Comparison of Star-forming and Outflow Properties of ZC406690 to those of Galaxies at Low- and High-z

High-z SFGs, like ZC406690, in many ways resemble both local starburst galaxies and local normal disk galaxies. The results from this work and others suggest that the overall structure and star-forming history (steady as opposed to bursty) of these galaxies more closely resembles normal local SFGs (Wuyts et al. 2011a; Elbaz et al. 2011), while properties of the star-forming regions and their outflows are more comparable to those of local nuclear starbursts.

The overall structure and large-scale properties of high-z rotation-dominated SFGs are in many ways similar to local disk galaxies. First, they both have disk-like morphologies (although local galaxies have much thinner disks) and most of the star-formation in these high-z galaxies occurs in an extended disk or ring and not in a central and compact star-burst region. Second, they are not considered extreme star-formers for their redshift (unlike

SMGs), and many of these observed galaxies have kinematic structures suggestive of no major interactions (Genzel et al. 2006, 2008, 2011; Shapiro et al. 2008; Förster Schreiber et al. 2009; Cresci et al. 2009; Gnerucci et al. 2010; Jones et al. 2010). Third, with the steady accretion of cold gas (in agreement with the ΛCDM model), these high-z galaxies can sustain star formation for long timescales (∼ 1-2 Gyr).

In local properties, however, high-z SFGs more closely resemble local starbursts. From the BPT diagram (Figure 2.6, as well as Shapley et al. 2005; Erb et al. 2006b; Liu et al. 2008), we see that normal SFGs at z∼1–3 are offset from normal local SFGs and better coincide with the region occupied by local starburst galaxies. As shown by Liu et al. (2008) and Brinchmann et al. (2008), this is due in part to variations in ionization parameter, SFR, sSFR, and density, between normal SFGs at high and low-z, and that in terms of these parameters local starbursts are more similar to the high-z SFGs. It should be noted that in the Liu et al. (2008) and Brinchmann et al. (2008) studies, they compared SDSS galaxies that were part of the main star-forming branch and ones that were offset from this branch, using similar stellar mass ranges for both samples. If we compare the properties (SFR, Σ_{gas}, P, n_{H_2}, σ, U, volume filling factor) of clumps A and B of ZC406690 with local galaxies, we find a closer correspondence with starbursts than with normal star-forming galaxies (see Table 2.4).

The outflows are dictated by the properties of the star-forming regions and not the overall structure of the galaxy, and are therefore similar to winds observed from local starbursts. We find that the mass-loading factor for the clumps is consistent with those observed from local starburst galaxies: 0.26 for a sample of several IRGs and ULIRGs (Rupke et al. 2005) and 2.5 for Mrk 231 (Rupke & Veilleux 2011). In addition, for Mrk 231, $\dot{E}_{\rm wind}/L_{bol} \sim 0.007$ (Rupke & Veilleux 2011), which is similar to our estimate for clump A. The measurements for Mrk 231 are lower limits; thus if the mass-loading and $\dot{E}_{\rm wind}/L_{bol}$ factors are larger, then Mrk 231 would be more similar to clump B rather than clump A. It is important to note that the measurements for Mrk 231 may not be directly comparable to the observations presented here, as they are made using the NaID absorption feature and are therefore sampling a different (and possibly more massive and energetic) component of the outflow. We also find similar mass loading factors when comparing our observations ($\eta \sim$ 3–8) to those of warm ionized outflows from local dwarf starbursts, where Martin (1999) finds $\eta \sim$ 1–5.

The outflow properties of individual clumps in ZC406690 resemble those from integrated data of other high-z SFGs. As for the local starbursts, most outflows from high-z galaxies have $\eta \geq 1$ (Pettini et al. 2000; Weiner et al. 2009; Steidel et al. 2010). We also find that the clumps fit the v_{out}-M_* and v_{out}-SFR relations found at z∼1.4 by Weiner et al. (2009). In addition, in their study of high-z outflows observed in absorption of light from background galaxies, Steidel et al. (2010) find maximum outflow velocities of 700–800 km s^{-1}, similar to what is found for the more rapid clump B outflow (810 km s^{-1}). These similarities suggest that the outflows observed in previous work from galaxy-integrated spectra could originate from massive clumps in those galaxies. They also indicate that the star-forming properties in high-z galaxies could scale from clump to galaxy size, suggesting that the lessons learned from studying individual star-forming clumps could be applied to entire galaxies and vice versa.

If some of the gas can escape the gravitational potential of these galaxies (as is likely for the hot and fast wind fluid, see Strickland & Heckman (2009) and perhaps also part of the warm ionized component), these numerous and powerful winds are likely significant in enriching the IGM at early times. Such enrichment from outflows is supported by theoretical models; Erb (2008) found that in their models of metal enrichment by star-formation paired with infall and outflow, $\eta \sim 1$ is required to fit the mass-metallicity relation at z $\sim$ 2. In addition, the results of cosmological simulations by Davé et al. (2011) indicate that $\eta \sim 1$ is a necessary condition to reproduce the mass-metallicity relation as well as IGM abundances. On the observational side, Steidel et al. (2010) find enriched gas as far as 125 kpc away from nearby galaxies in a sample of ∼100 z∼2–3 Lyman-break SFGs. On the other hand, if some of the gas falls back onto the clumps (as suggested by the fact that $v_{wind} < v_{esc,clump}$ for clump A), this could prolong the clump star-formation timescales.

Evidence for shocks in the clump outflows allows us to draw additional comparisons between ZC406690 and local and high-z SFGs. The finding that some shock contribution to the emission is necessary to explain the observed emission line ratios in the clumps and their winds is consistent with observations of outflows from local starbursts, which are dominated by shock-like emission line ratios even in the absence of AGN. However, if shocks are a common feature of high-z outflows, which in turn are ubiquitous in z∼2–3 galaxies, then this has important consequences for abundance measurements at high-z. As suggested by Shapley et al. (2005) and Erb et al. (2006b), using [NII]/Hα alone as an abundance indicator could be flawed in the presence of shocks or AGN. As they note, many of these emission line ratio abundance indicators are calibrated from galaxies and star-forming regions that populate the 'HII' branch of the BPT diagram. Therefore, galaxies that are offset from this branch (mainly in terms of [NII]/Hα), such as local starbursts and high-z SFGs, require a different calibration. Another option is to use photoionization and shock models with multiple emission line diagnostics to get more accurate abundances. It is not yet clear whether abundances are overestimated due to shocks in most observed high-z SFGs, but this is an issue that deems more attention through continued high-resolution AO emission line measurements in these systems.

2.5 Conclusions

Using high S/N SINFONI/VLT observations with AO, we find powerful outflows localized to the star-forming ∼kpc-size clumps of the $z \sim 2$ SFG, ZC406690. Spectra of the clumps and surrounding regions have broad, blue Hα line wings extending up to 800 km s^{-1} from line center. Much of this broad emission is coming from a region offset from the center of clump B that also has enhanced [NII]/Hα and [SII]/Hα ratios, indicative of a superwind laden with shocks. The outflow velocities derived from the line widths are comparable to and slightly in excess of the escape velocity of the clumps (and the galaxy), indicating that some of the wind material could fall back on other parts of the galaxy or perhaps escape out to the IGM.

By comparing the energy and momentum injection rates of the wind to the Murray et al. (2005) model of a starburst-driven wind, we find that the clump A wind satisfies the predictions for both energy- and momentum-driven winds, but that the clump B wind cannot be explained by either within the context of this model. Star formation feedback from the winds could greatly contribute to the large velocity dispersions seen in ZC406690 and other z $\sim$ 2–3 galaxies, although based on measurements from the clumps, feedback alone cannot account for this turbulence.

The clumps have a large range in ages (from metallicity), which is reflected in the maturity of their outflows (as seen in the variation in outflow velocity, physical extent, mass-loading and shock-like emission line ratios), and they appear to be more extincted than the surrounding regions, as one would expect for dense star-forming regions. It is possible that the younger clump (A) resembles what clump B looked like at an earlier time and that the current state of the galaxy gives us a snapshot of various stages of clump formation and evolution.

In terms of global properties (disk-like morphology, location of star-formation, star-formation timescale), ZC406690 is similar to local disk galaxies, while in terms of local properties of the star-forming regions and the outflows (SFR, Σ_{SFR}, n_{H_2}, pressure, ionization parameter, v_{out}, mass-loading, volume filling factor), its clumps more closely resemble star-forming regions in local starburst galaxies. The outflow properties of the clumps are also similar to those of outflows observed in other galaxies at z $\sim$ 1–3, suggesting that massive clumps could be the source of a significant fraction of outflowing material in these galaxies as well, and that although ZC406690 is quite massive, it may not be very unusual for $z \sim 2$ SFGs in terms of star-formation feedback.

These types of winds coming from kpc-size regions could have a significant effect on galaxy evolution during this epoch. They could inhibit star-formation with the injection of heat into the ISM and the mass-loss associated with the outflowing material in the wind could reduce the lifetime of the clumps. They also influence the chemical composition of the ISM and the IGM by expelling metal-rich gas from star-forming regions. The results presented in this paper inform our understanding of the properties, evolution, and feedback of star-forming regions at high-z, which in turn teaches us about the role that these star-forming regions play in galaxy evolution on Gyr timescales.

2.6 Appendix A: Systematic errors for M_{gas}

In this section, we derive the systematic errors in our M_{gas} calculation from a combination of (1) scatter in the intrinsic relation, (2) the varying slope and zero point of the relation as quoted by different authors, (3) the extrapolation of the relation from low-z to high-z, and (4) the application of the relation on ~kpc scales.

First, we consider the scatter of Σ_{gas} within an individual Kennicutt-Schmidt (KS) relation. Bigiel et al. (2011) compare Σ_{gas} and Σ_{SFR} for thousands of positions in 30 nearby disk galaxies, and find that the 1σ scatter is roughly 0.3 dex or 70% (see their Figure 1).

Genzel et al. (2010) find a similar systematic uncertainty for Σ_{gas} of 0.3 dex in the KS relation for both local and high-z galaxies.

Second, we consider the systematic uncertainty resulting from extrapolating the low-z KS relation to a high-z galaxy. As seen in Genzel et al. (2010) and Daddi et al. (2010a), high and low-z galaxies on the star-forming 'main sequence' (that is, neglecting local ULIRGs and high-z SMGs) fit on the same KS relation with an offset in zero point of less than a few x 0.1 dex, in the sense that high-z galaxies could have slightly lower gas masses than the local relation would predict. ZC406690 falls on the upper SFR and M_* end of the SF main-sequence.

Third, we consider the scatter between different versions of the KS relation by looking at the most recent observational results (Genzel et al. 2010; Daddi et al. 2010a; Kennicutt et al. 2007). We do not consider the slope and zero-point of the Bigiel et al. (2011) relation, as they note that theirs is not a 'rigorous' fit. From the three other relations, the maximum difference in Σ_{gas} for our clumps is around 50%. Both the Kennicutt et al. (2007) and the Daddi et al. (2010a) relations have slightly larger slopes, so the effect of using these would be to lower the resulting gas masses. We note that the gas masses rely on the extinction correction based on the galaxy-integrated SED fitting and not on the $H\alpha/H\beta$ measurements (which are uncertain for clump B). As mentioned in section 3.1, applying the Balmer decrement-based extinction correction would increase the gas masses by 50%, the opposite effect of using the other KS laws.

The statements made above rely on the KS conversion for normal Òmain sequenceÓ star-forming galaxies. While ZC406690 is in fact on the star-forming main sequence, there is some indication that the clumps might follow the ULIRG KS law, both because the clumps have similar properties to local starburst regions and also based on recent work by Sargent et al. (2012) suggesting that $z \sim 2$ normal SFGs can simultaneously have a normal star-forming component and a starburst component. Using the ULIRG law to determine the gas masses for our clumps would lower the resulting masses. From Genzel et al. (2010), Figure 4, we find that the offset from the main-sequence KS law to the ULIRG law is around 0.8 dex for Σ_{SFR}s relevant for the clumps. Therefore, we assume a lower limit for the gas masses of 0.8 dex.

Fourth, we believe it is reasonable to assume the global KS relation for regions of ~1 kpc in size. Bolatto et al. (2008), find that many of the gas properties of extra-galactic GMCs are consistent with properties of the MW. In addition, Bigiel et al. (2011) find that their binned 1 kpc-scale relation is almost identical to the relation binned from global literature data. Kennicutt et al. (2007) also look at the KS relation on the scale of 0.5 and 2 kpc in M51a and find a very similar slope to that from the global relation from Kennicutt (1998), and an offset in zero-point of around 0.4 dex. It should be noted that the M51a integrated point falls 0.24 dex below the global law, so a good estimate for the offset in zero-point from extrapolation of the global to local KS relation would be around 0.15 dex. In addition, recent observations of the lensed cosmic eyelash galaxy at z~2.3 by Swinbank et al. (2011) and Danielson et al. (2011), probe the KS relation on the scale of 100 pc submillimeter-bright clumps. They find that the global KS relation should hold on scales of roughly ~kpc, but should break down below 100 pc, and that globally, the galaxy is consistent with local ULIRGs (as expected for a high-z SMG). Finally, Leroy et al. (2012) study Hα–, UV–, and IR-derived SFRs in addition to IRAM CO data at 1 kpc resolution for 30 disk galaxies, and find that the Hα–derived $\Sigma_{SFR}s$ could be off by about 0.3 dex at small vs. large scales, comparable to the 0.3 dex systematic uncertainty we assume.

The systematic uncertainties from applying the local KS relation to high-z galaxies, from the scatter between relations, from extrapolating to ∼kpc scales and from propagating the Σ_{SFR} error are all less than or equal to the intrinsic scatter from the Bigiel et al. (2011) and Genzel et al. (2010) relations of 0.3 dex, so we therefore use this as the upper limit of the systematic uncertainty for our derived clump Σ_{gas} and as mentioned above, we use 0.8 dex as a lower limit.

2.7 Appendix B: Derivation of mass outflow rates

In this section we discuss the model used to derive the mass outflow rates of the clumps, which is identical to the derivation used in Genzel et al. (2011). We derive the mass in the outflow and the mass outflow rates assuming two different geometric models. For both, we assume an outflow of warm, ionized gas into a solid angle Ω with radially constant outflow rate and velocity. As we are only calculating the mass outflow rate for the warm-ionized component and neglecting other components of the wind (neutral, molecular, and hot), our masses and rates are therefore lower limits. We assume case B recombination of photoionized gas with T $= 10^4$K, giving a volume emissivity of $\gamma_{H\alpha} = 3.56 \times 10^{-25}$ erg cm^{-3} s^{-1}. We then calculate the mass of outflowing material from the extinction-corrected Hα luminosity:

$$L_{H\alpha} = \gamma_{H\alpha} \int \Omega R^2 n_e(R) n_p(R)\,\mathrm{d}R, \tag{2.9}$$

$$M_{HII,He} = 1.36 \times m_p \int \Omega R^2 n_p\,\mathrm{d}R = \frac{1.36 \times m_p L_{H\alpha}}{\gamma_{H\alpha} n_{eff}}, \tag{2.10}$$

$$\dot{\mathrm{M}}_{\mathrm{out}} = \Omega R^2 1.36 \times m_p n(R) v_{out} = M_{HII,He} \times \frac{v_{out}}{R_{out}} \tag{2.11}$$

where L$_{H\alpha}$ is the extinction-corrected Hα luminosity, v$_{out}$ is the outflow velocity derived from the Hα line profiles and given in Table 2.3, and R$_{out}$ is the maximum radial extent of the outflow, which is model dependent, as is n$_{eff}$ (electron density). The extinction-corrected Hα luminosity is taken from the broad-component of the line only, and is multiplied by an additional factor of 2 to account for the asymmetry of the broad line wing (i.e. much of the red wing is obscured, see Figure 2).

For our first model, we assume that the average electron density in the outflow scales like R^{-2}, but the local electron density of clouds and dense filaments in the outflow (from which we observe Hα emission) is constant at n$_e$ = 100 cm^{-3}. In this model, R$_{out} \sim R_{HWHM}$ and is given in Table 2.2. As mentioned in section 4.1.4, the density in the wind could be closer to 4 cm^{-3} and this is reflected in the uncertainties for $\dot{M}_{out}$. In fact, the value of n_{eff} is the dominant source of uncertainty for M_w and $\dot{M}_{out}$ and for subsequent calculations that depend on these quantities. We find that the lower limit for n_{eff} (10 cm^{-3}) gives unrealistic upper limits for the mass-loading factor of 30–60 (see Table 2.3).

For the second model, we assume that the entire outflow cone is filled with the ionized, Hα-emitting gas, and that n_{eff} still scales like R^{-2}. Thus, $n_{eff} = n_{in}R_{in}/R_{out}$, where R_{in} is the radius at which the outflow is launched and n_{in} is the corresponding electron density at that radius. Assuming the outflow is very extended (Steidel et al. 2010), we take $R_{out} \sim R_{disk} \sim 10R_{in}$. From the n_e^2 scaling of the Hα emission, $R_{HWHM} \sim 2.3R_{in}$. For n_{in} we take an approximate average of the clump electron densities derived from the [SII] doublet, $\sim 1000\ cm^{-3}$. Thus, for the second model, R_{out} = 4.3 kpc and n_{eff} = 100 cm^{-3}. These two models likely span the lower and upper limits for R_{out} and so we take the average of the results from the two models as our wind mass and mass outflow rates (see Table 2.3).

Table 2.3: Calculated Properties of the Clumps and their Outflows

	Clump A	Clump B
SFR ($M_\odot$ yr^{-1})[a]	40 ± 12	11 ± 3.3
$\dot{M}_{out}$($M_\odot$ yr^{-1})[a]	117^{+1110}_{-95}	78^{+590}_{-50}
v_{out}(km s^{-1})[a]	440 ± 150	810 ± 270
$v_{out}/v_{escape,clump}$	0.75 ± 0.39	2.4 ± 1.3
$v_{out}/v_{escape,galaxy}$	0.54 ± 0.26	0.99 ± 0.48
t_{dyn} (Myr)	1.8 ± 0.9	1.5 ± 0.8
M_w($M_\odot$)	$1.79x10^{8}\,{}^{+1.96\times10^{9}}_{-1.43\times10^{8}}$	$1.09x10^{8}\,{}^{+8.36\times10^{8}}_{-9.45\times10^{7}}$
E_w(ergs)	$3.46x10^{56}\,{}^{+3.81\times10^{57}}_{-3.21\times10^{56}}$	$7.16x10^{56}\,{}^{+5.50\times10^{57}}_{-7.06\times10^{56}}$
$M_{gas,mol}$ ($M_\odot$)	$1.6x10^{10}\,{}^{+1.1\times10^{10}}_{-1.3\times10^{10}}$	$7.8x10^{9}\,{}^{+5.5\times10^{9}}_{-6.6\times10^{9}}$
Σ_{gas}($M_\odot pc^{-2}$)[a]	8000^{+5600}_{-6800}	1200^{+840}_{-1000}
Σ_{SFR} ($M_\odot pc^{-2} yr^{-1}$)[a]	13.5 ± 4.0	1.6 ± 0.5
P_{kin}(dyne cm^{-2})	$2.9x10^{-7}$ ± $1.6x10^{-7}$	$5.3x10^{-8}$ ± $5.5x10^{-8}$
P_{weight}(dyne cm^{-2})	$3.0x10^{-7}\,{}^{+2.9\times10^{-7}}_{-2.6\times10^{-7}}$	$6.7x10^{-9}\,{}^{+6.6\times10^{-9}}_{-8.0\times10^{-9}}$
P_{turb}(dyne cm^{-2})	$6.8x10^{-9}$ (± $2.1x10^{-9}$) x f_p	$8.4x10^{-10}$ (± $2.5x10^{-10}$) x f_p
P_{rad}(dyne cm^{-2})	$7.1x10^{-9}\,{}^{+5.4\times10^{-9}}_{-6.4\times10^{-9}}$	$1.3x10^{-10}\,{}^{+1.0\times10^{-10}}_{-1.2\times10^{-10}}$
P_{ram} (dyne cm^{-2})	$4.4x10^{-7}$ $({}^{+1.8\times10^{-6}}_{-4.0\times10^{-7}})$ x $(\rho_w/100)$	$1.5x10^{-6}$ $({}^{+6.0\times10^{-6}}_{-1.3\times10^{-6}})$ x $(\rho_w/100)$
ρ_{wind} (cm^{-3})[b]	67.3 ± 73.7	0.4 ± 0.5
L_{bol} (ergss^{-1})	$1.6x10^{45}$ ± $4.8x10^{44}$	$4.4x10^{44}$ ±$1.3x10^{44}$
$\dot{M}_{out}$x v_{out}^2/ L_{bol}	0.0045, [$7.64x10^{-5}$–0.048][c]	0.046, [0.00021–0.33][c]
$\dot{p}_{out}/P_{rad}$	6.2, [0.5–65.1][c]	33.7, [2.1–244.5][c]
η ($\dot{M}_{out}$/SFR)[a]	$2.9^{+27.6}_{-2.5}$	$8.6^{+53.7}_{-7.5}$
E_{shock} (ergs)	$3.46\ x10^{55}\,{}^{+3.81\times10^{56}}_{-3.46\times10^{55}}$	$2.15x10^{56}\,{}^{+1.66\times10^{57}}_{-2.15\times10^{56}}$
E_{turb} (ergs)	$3.28x10^{57}\,{}^{+2.31\times10^{57}}_{-2.77\times10^{57}}$	$1.89x10^{57}\,{}^{+1.33\times10^{57}}_{-1.59\times10^{57}}$
f_v (n_{avg}/n_{local})	$2.2x10^{-2}$–$3.7x10^{-4}$	$2.3x10^{-3}$–$2.2x10^{-4}$

[a] from Genzel et al. (2011)
[b] assuming $P_{ram} \sim P_{weight}$
[c] 1σ range

Table 2.4: Comparison of Clump and Galaxy Properties

	Clumps	ZC406690	Milky Way	ULIRGs
SFR ($M_\odot$ yr^{-1})	10–40	300	3	100–1000
Σ_{gas}($M_\odot$pc^{-2})	1200–8000	1100	200	3000–30,000
f_{gas}	0.4–0.7	0.3	0.1	0.1
log10(P/k)[a]	8.6–8.9	9.0	5.9	9.3
log10(n_{H_2})	4.0–5.8	...	2	3–4
σ (km s^{-1})	85	63	5	50–100
log10(U) (cms^{-1})	7.8–8	...	7.5	7.7
η[b]	3–8	...	...	0.1–2.5
P/(L_{bol}/c)[b]	6–33	...	...	0.1–0.5
$\frac{dE}{dt}/L_{IR}$[b]	0.04-0.005	...	...	0.0001-0.007
f_v (n_{avg}/n_{local})	2x10^{-2}–4x10^{-4}	...	10^{-2}	3.6x10^{-3}

[a] from P_{kin}

[b] These values are derived from Hα for ZC406690 and from Na ID for ULIRGs (Rupke et al. 2005; Rupke & Veilleux 2011). However, this might not be a fair comparison since these measurements sample very different components of the wind. In addition, the largest values for ULIRGs (for η and $\frac{dE}{dt}/L_{IR}$), which come from Mrk231, are lower limits (Rupke & Veilleux 2011).

Chapter 3

The SINS/zC-SINF Survey of $z \sim 2$ Galaxy Kinematics: Outflow Properties

Using SINFONI Hα, [NII]and [SII] AO data of 27 $z \sim 2$ star-forming galaxies (SFGs) from the SINS and zC-SINF surveys, we explore the dependence of outflow strength (via the broad flux fraction) on various galaxy parameters. For galaxies that have evidence for strong outflows, we find that the broad emission is spatially extended to at least the half-light radius ($\sim$ a few kpc). Decomposition of the [SII] doublet into broad and narrow components suggests that this outflowing gas probably has a density of $\sim$10–100 cm^{-3}, less than that of the star forming gas (600 cm^{-3}). There is a strong correlation of the Hα broad flux fraction with the star formation surface density of the galaxy, with an apparent threshold for strong outflows occurring at 1 $M_\odot yr^{-1}$ kpc^{-2}. Above this threshold, we find that SFGs with logM_*>10 have similar or perhaps greater wind mass loading factors ($\eta = \dot{M}_{out}/SFR$) and faster outflow velocities than lower mass SFGs, suggesting that the majority of outflowing gas at $z \sim 2$ may derive from high-mass SFGs. The mass loading factor is also correlated with the SFR, galaxy size and inclination, such that smaller, more star-forming galaxies launch more powerful outflows, and these are more readily observed when they are face-on. We propose that the observed threshold for strong outflows and the observed mass loading of these winds can be explained by a simple model wherein "break-out" of winds is governed by pressure balance in the disk.

3.1 Introduction

Most high-z SFGs from rest-UV/optical samples show evidence for powerful galactic outflows, as indicated by UV absorption spectroscopy (Pettini et al. 2000; Shapley et al. 2003; Steidel et al. 2010; Weiner et al. 2009; Kornei et al. 2012) and broad Hα emission-line profiles (Shapiro et al. 2009; Genzel et al. 2011; Newman et al. 2012a). This 'star formation feedback' may be an essential ingredient in the evolution of high-z star forming galaxies, particularly between z $\sim$ 1–3, at the peak of the star formation rate density (Hopkins &

Beacom 2006). However, little is yet known about how galaxy parameters determine the prevalence and strength of these outflows.

Current theoretical models suggest that outflows could be driven by energy or momentum feedback (e.g. Murray et al. 2005). In the simple momentum driven wind scenario of Oppenheimer & Davé (2006, 2008), the mass loading parameter of the wind primarily depends on the circular velocity of the disk v_d, $\eta \propto v_d^{-1} \propto M_{baryon}^{-1/3}$, if the wind outflow velocity is near the escape velocity (Murray et al. 2005). Hopkins et al. (2012) have recently carried out high-resolution SPH simulations of isolated galaxies with different types of input feedback, including that from supernovae, stellar winds, expanding HII regions and radiation pressure and find an overall scaling of $\eta \propto v_d^{-1}\Sigma_{gas}^{-1/2}$ and $\eta \sim 1$ for the parameters of typical high-z massive SFGs and with energy-driven winds. The scaling with v_d^{-1} is consistent with that found by Oppenheimer & Davé (2006, 2008), yet the dependence on $\Sigma_{gas}{}^{-1/2}$ is contrary to the findings of Chen et al. (2010), who found a positive correlation of Na D equivalent width (EW) with Σ_{SFR} from SDSS data of ∼100,000 galaxies, where Na D EW is used here as a proxy for the mass loading (η).

In this paper we analyze the outflow properties of 27 $z \sim 2$ SFGs, discussed in more detail in Förster Schreiber et al. (2013a) and based on new high-quality Hα emission line SINFONI/VLT integral field (IFU) spectroscopy with adaptive optics (AO) (Eisenhauer et al. 2003; Bonnet et al. 2004). We adopt a ΛCDM cosmology with Ω_m =0.27, Ω_b=0.046 and H_0=70 km/s/Mpc (Komatsu et al. 2011), and a Chabrier (2003) initial stellar mass function (IMF).

3.2 Observations, Data Reduction and Analysis Techniques

The galaxy sample discussed here (see Table 3.1) is described in Mancini et al. (2011) and Förster Schreiber et al. (2013a). Our 27 z∼2–2.5 SFGs are drawn from the SINS and zC-SINF surveys of Hα+[NII] integral field spectroscopy with SINFONI on the ESO VLT (Förster Schreiber et al. 2009; Mancini et al. 2011; Förster Schreiber et al. 2013a). They were selected either from their U_nGR colors satisfying the 'BX' criteria (Steidel et al. 2004; Adelberger et al. 2004; Erb et al. 2006b; Law et al. 2009) or based on K band imaging via the 'BzK' criterion for 1.4 <z <2.5 SFGs (Daddi et al. 2004b). They sample the z∼2.2 star-forming 'main sequence' for stellar masses between $10^{9.5}$ to $10^{11.5}$ $M_\odot$. Our sample includes 25 galaxies observed with AO-mode with sufficient SNR for analysis (0.05" pixels, typical FWHM 0.2–0.25") in addition to 2 galaxies observed in seeing limited mode that have very extended disks and thus are well resolved with 0.125" pixels and FWHM∼0.5". The data are of high quality (∼ 6h average integration time per galaxy, with a range from 2 to 22h, and a total integration time for the entire sample of 180h) and were reduced with our standard data reduction methods and analysis tools (Schreiber et al. 2004; Davies 2007; Förster Schreiber et al. 2009; Mancini et al. 2011).

Stellar masses and ages are derived from SED modeling in Förster Schreiber et al. (2009)

Table 3.1: Galaxy Properties

Galaxy ID	**Reference**	$\mathbf{M_*}$ ($10^{11}M_\odot$)	**SFR (Hα)** ($M_\odot$/yr)	Σ_{SFR} ($M_\odot yr^{-1} kpc^{-2}$)
Q1623-BX455	1,2	0.10 ± 0.031	63 ± 19	1.66 ± 0.52
Q1623-BX502	1,2	0.023 ± 0.0070	40 ± 12	2.86 ± 0.90
Q1623-BX543	1,2	0.094 ± 0.028	183 ± 55	2.38 ± 0.98
Q1623-BX599	1,2	0.57 ± 0.17	131 ± 39	3.95± 1.63
SSA22a-MD41	1,2,3	0.077 ± 0.010	131 ± 39	0.80 ± 0.24
Q2343-BX389	1,2	0.41 ± 0.080	196 ± 59	0.74 ± 0.22
Q2343-BX513	1,2	0.27 ± 0.081	28 ± 8	1.00 ± 0.36
Q2343-BX610	1,2	1.00 ± 0.27	212 ± 64	1.15 ± 0.35
Q2343-BX482	1,2	0.18 ± 0.080	121 ± 36	0.61 ± 0.19
GMASS-2303	4	0.072 ± 0.022	30 ± 9	0.52 ± 0.16
GMASS-2363	4	0.22 ± 0.065	50 ± 15	1.17 ± 0.37
ZC-401925	5,6,7	0.052 ± 0.016	13 ± 4	0.19 ± 0.060
ZC-404221	5,6,7	0.11 ± 0.050	60 ± 18	1.80 ± 0.57
ZC-405501	5,6,7	0.10 ± 0.030	68 ± 20	0.26 ± 0.10
ZC-405226	5,6,7	0.092 ± 0.028	82 ± 25	0.34 ± 0.17
ZC-406690	5,6,7	0.44 ± 0.13	480 ± 144	1.87 ± 0.57
ZC-407376	5,6,7	0.20 ± 0.060	283 ± 85	2.43 ± 0.77
ZC-407302	5,6,7	0.30 ± 0.090	260 ± 78	2.72 ± 0.83
ZC-409985	5,6,7	0.12 ± 0.036	40 ± 12	0.81 ± 0.25
ZC-410041	5,6,7	0.042 ± 0.013	105 ± 31	0.72 ± 0.22
ZC-410123	5,6,7	0.042 ± 0.013	40 ± 12	0.30 ± 0.090
ZC-411737	5,6,7	0.040 ± 0.015	60 ± 18	1.06 ± 0.33
ZC-412369	5,6,7	0.18 ± 0.050	182 ± 55	1.72 ± 0.60
ZC-413507	5,6,7	0.088 ± 0.025	92 ± 28	1.19 ± 0.43
ZC-413597	5,6,7	0.070 ± 0.020	86 ± 26	1.72 ± 0.55
ZC-415876	5,6,7	0.084 ± 0.022	42 ± 13	2.33 ± 0.80
SA12-6339	5,6,7	0.26 ± 0.077	681 ± 204	17.34 ± 9.41

References for parent sample. (1) Erb et al. (2006b), (2) Steidel et al. (2004), (3) Erb et al. (2003), (4) Kurk et al. (2009), (5) Lilly et al. (2007), (6) Lilly et al. (2009), (7) McCracken et al. (2010).

and Mancini et al. (2011) assuming constant or exponentially declining star formation histories with Bruzual & Charlot (2003) tracks. The SFRs are derived from the SED modeling and from Hα (SFR=$L_{H\alpha}$/2.1x10^{41} erg/s, Kennicutt (1998), corrected for a Chabrier (2003) IMF) with a Calzetti et al. (2000) reddening law with $A_{V,gas} = 2.3 \times A_{V,SED}$. Half light radii ($R_{1/2}$) were computed from the cumulative Hα flux profile determined after fitting a 2D exponential (Sersic n = 1) to the data. We calculate molecular gas masses (M_{gas}) and surface densities (Σ_{gas}= 0.5 $\times$ $M_{gas}/(\pi R^2_{1/2})$) from the Hα-derived SFRs using the molecular gas to star formation surface density relation with $M_{gas}(M_\odot)$ = 5.8$\times10^8$ x SFR ($M_\odot yr^{-1}$) (Tacconi et al. 2013).

To isolate the broad emission for coadding, we remove large-scale rotational velocity gradients from the data cubes by aligning the spectral axis of each pixel, such that the Hα peak lies at the same velocity throughout the cube. This technique minimizes the width of the galaxy integrated spectrum due to large scale motions (e.g. rotation) in the narrow velocity component, and thus maximizes the contrast between the broad and narrow components. Shapiro et al. (2009) demonstrated that this method does not create artificial broad wings. From these velocity-shifted data cubes, we create spatially-integrated spectra for each galaxy by collapsing the cubes onto a single spectral axis (see: Förster Schreiber et al. 2009; Shapiro et al. 2009). Various stacks of spectra are generated by removing a fitted continuum from each spectrum, placing the spectra on a common rest-frame wavelength axis, weighting each spectrum by the signal to noise ratio (SNR) of Hα, and coadding the final spectra.

Broad emission has previously been detected in SINS/zC-SINF galaxies by Shapiro et al. (2009), Genzel et al. (2011), and Newman et al. (2012a) and attributed to galactic outflows. We quantify the fraction of the emission line flux in this underlying broad component by simultaneously fitting two Gaussian functions to each of the Hα, [NII]$\lambda\lambda$6548,6584 and [SII]$\lambda\lambda$6716,6731 emission lines, setting the kinematics (velocity, line width) of all of the narrow Gaussian components to be equal to each other, and likewise setting the kinematics of the broad Gaussian components equal to each other. We allow the broad Hα flux to vary, but set the [NII]/Hα ratio in the broad component to the [NII]/Hα ratio in the narrow component (and likewise for [SII]/Hα). Genzel et al. (2011) demonstrated that in the absence of a broad component, and after removal of large scale velocity shifts as described above, the remaining velocity profiles can be well fit by Gaussians. The 'broad flux fraction' is defined as the ratio of the flux in the broad Hα emission line to the flux in the narrow Hα emission line.

We also generate position-velocity (pv) data by extracting the spectra along the major galaxy axis for each shifted cube with a slit wide enough to cover most of the minor axis emission. The data are then co-added and re-sampled onto a normalized spatial scale of 0.07x$R_{1/2}$ (FWHM $\sim$ 0.3x$R_{1/2}$) and spectral scale of 40 km/s/pixel ($\sim$90 km/s FWHM).

3.3 Outflow Properties in $z \sim 2$ SFGs

We ascertain that the outflows are driven by the star formation activity and not by an AGN as we have excluded any known AGN from our sample, find that the broad emission is extended and not concentrated towards the kinematic or morphological center (see section 3.3.1), and measure [NII]/Hα ratios compatible with the expected metallicity based on the $z \sim 2$ mass-metallicity relation (Erb et al. 2006b) and too low to be consistent with the presence of an AGN. In two cases we trace the origin of the outflows to individual giant star forming clumps embedded in the disk (Genzel et al. 2011; Newman et al. 2012a). We note that Genzel et al. (2011) suggest that the bright emission coming from a clump in one of our galaxies (ZC407302) could be due to AGN activity if this clump is an external minor merger, rather than a star forming clump formed within the disk. However, there is no other evidence that this galaxy contains an AGN.

3.3.1 Outflows are Spatially Extended

The broad emission (FWHM ∼450 km/s) is spatially extended over the half-light radii ($R_{1/2}$), which corresponds to a few kpc in the small galaxies and up to 6 kpc in the larger disks. This is demonstrated in the bottom panel of Figure 3.1, where we show a co-added pv diagram of the line emission (large-scale velocity gradients removed) along the morphological major axis for the galaxies. Broad emission is detected at least out to $R_{1/2}$, and its width between 0.5 x $R_{1/2}$ and $R_{1/2}$ (FWHM = 423 ± 19 km/s) is nearly as broad as within 0.5 x $R_{1/2}$ (FWHM = 475 ± 12 km/s). The upper panel of Figure 3.1 shows that the emission in the outer regions of the galaxies is almost as broad as in the inner regions, and implies a constant or decreasing mass-loading with increasing galacto-centric radius.

The 10 galaxies used in this coadd (BX455, BX513, BX543, BX599, SA12-6339, ZC404221, ZC407306, ZC407302, ZC412369, ZC415876) are selected such that they have noticeable broad line wings without the need for stacking and an absence of OH residuals near Hα. All but one have $R_{1/2}$<3 kpc and all have Σ_{SFR}>1 $M_{\odot} yr^{-1} kpc^{-2}$. However, their stellar masses and SFRs span the ranges seen in our full sample. We note that although most of the galaxies from this stack are small (with $R_{1/2}$ <3 kpc), we also observe broad emission from stacks of larger galaxies that also have Σ_{SFR}>1 $M_{\odot} yr^{-1} kpc^{-2}$ (see next section).

3.3.2 The Broad Flux Fraction is Strongly Dependent on the SF Surface Density

We explore the dependence of the broad flux fraction on galaxy properties by dividing the entire sample into two bins each (low/high) in star formation rate, stellar mass, size, inclination and star formation surface density. We then co-added the spectra in each of the bins and computed the ratio of the broad to narrow Hα emission. The results are summarized in Table 3.2.

Table 3.2: Broad flux fraction for high and low bins of different galaxy properties

Property	F_{broad}/F_{narrow} (Hα)		FWHM$_{broad}$ (km/s)		$\Delta v_{\rm broad-narrow}$ (km/s)		Significance	Dividing
	High bin	Low bin	High bin	Low bin	High bin	Low bin	of difference	value
SFR	0.65 ± 0.074	0.50 ± 0.041	510 ± 12	423 ± 47	-23 ± 4	-21 ± 8	2σ	100 $M_\odot$/yr
$\mathbf{R_{1/2}}$	0.50 ± 0.054	0.76 ± 0.082	503 ± 15	432 ± 19	-15 ± 6	-35 ± 6	3σ	3 kpc
Σ_{SFR}	0.77 ± 0.027	0.16 ± 0.030	500 ± 16	423 ± 75	-27 ± 4	-43 ± 23	20σ	1 $M_\odot yr^{-1}kpc^{-2}$
inclination	0.47 ± 0.055	0.77 ± 0.091	510 ± 44	514 ± 12	-39 ± 14	-32 ± 5	3σ	49–55^o
$\mathbf{m_*}^1$	0.63 ± 0.056	0.41 ± 0.042	528 ± 13	423 ± 45	-32 ± 5	-20 ± 8	4σ	1x10^{10} $M_\odot$
$\mathbf{m_*}^2$	0.23 ± 0.21	0.12 ± 0.040	423 ± 66	423 ± 80	-28 ± 18	-48 ± 42	0.5σ	”
$\mathbf{m_*}^3$	0.85 ± 0.097	0.71 ± 0.10	520 ± 11	428 ± 30	-25 ± 4	-13 ± 7	1.5σ	”

The high/low bins for SFR, M_*, Σ_{SFR}, $R_{1/2}$, and inclination are divided above and below the value(s) shown in column 9 and have roughly an equal number of galaxies in each bin. The spectrum from each stack was fit constraining the narrow FWHM to between 190 and 210 km/s, so that the broad component was not fit as a very broad narrow component, and allowing the relative velocities of the two components and the broad line width (FWHM) to vary. The best fit broad FWHM and the relative velocities for each bin are shown in columns 4–7. For the M_* bins, (1) is for all galaxies, (2) is for galaxies with Σ_{SFR}<1 $M_\odot yr^{-1}kpc^{-2}$, and (3) is for galaxies with Σ_{SFR}>1 $M_\odot yr^{-1}kpc^{-2}$.

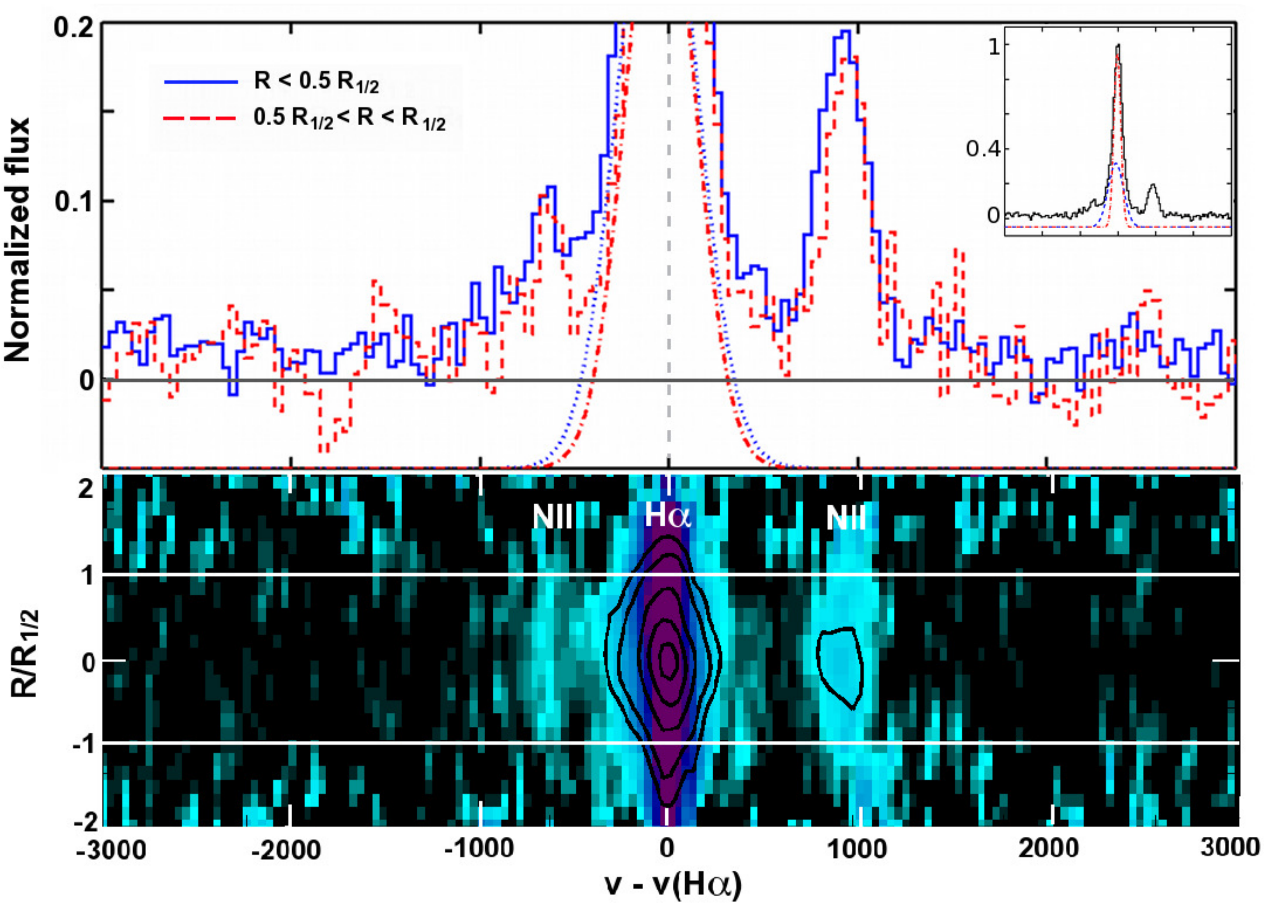

Figure 3.1: Lower panel: Co-added position-velocity (pv) diagram for the 10 sources with the best evidence for broad emission, with the vertical (spatial) axis normalized to $R_{1/2}$. The black contours show the unnormalized stack, while the colors have been normalized according to the peak Hα flux for each spatial row. The broad emission in light blue (>200–300 km/s from the systemic velocity) is spatially extended (vertical axis) out to at least $R_{1/2}$. Upper panel: Spectra from the inner (R<0.5 x $R_{1/2}$, blue, solid line) and outer (0.5 x $R_{1/2}$<R<$R_{1/2}$, red, dashed line) regions of the galaxies, with the broad fitted components shown by the blue dotted line (inner) and red dash-dotted line (outer). The inner and outer region spectra have F_{broad}/F_{narrow} = 1.31 ± 0.075 and 1.13 ± 0.12 with broad to narrow component velocity shifts of -41 ± 5 km/s and -33 ± 9 km/s, respectively. The inset shows the entire Hα line for the inner spectrum (black) with the broad component (blue, dashed) and narrow component (red, dash-dot) overplotted.

The star formation surface density has the largest effect on the broad flux fraction, such that galaxies with Σ_{SFR}>1 $M_{\odot} yr^{-1} kpc^{-2}$ drive the strongest outflows, which confirms and strengthens a similar finding in Genzel et al. (2011). This result is also consistent with what was observed in z ∼ 0 SFGs by Chen et al. (2010), where they found a strong correlation of Na D absorption equivalent width (from SDSS data of ∼ 100,000 galaxies) with Σ_{SFR}.

In Figure 3.2, we see the dependence of the broad Hα flux fraction on Σ_{SFR} from 5 Σ_{SFR}-binned points as well as three massive star-forming clumps. The trend seen in Figure 3.2 can be well described as a 'threshold' for outflows. All of the data points with Σ_{SFR} >1 $M_{\odot} yr^{-1} kpc^{-2}$ have $F_{broad}/F_{narrow} > 0.7$, while all those below this threshold have $F_{broad}/F_{narrow} \leq 0.25$. We also compare the spectra and broad component fits for stacks of galaxies above and below the Σ_{SFR} threshold in the lower panels of Figure 3.2. For these high Σ_{SFR} and low Σ_{SFR} stacks, the two-component fits yield a reduced χ^2 of 1.15 and 1.55, respectively, while an imposed single-component fit yields reduced χ^2 values of 16.9 and 3.27, indicating that a two-component fit is much better in the stack with a higher F_{broad}/F_{narrow} ratio, and thus stronger wind signature, and somewhat better in the stack with a smaller outflow signature.

The broad flux fraction also varies (to a lesser extent) with M_*, SFR, $R_{1/2}$ and inclination such that higher F_{broad}/F_{narrow} values and thus stronger outflows are observed for massive, high SFR, compact, face-on galaxies. We further explore the M_* trend by dividing each of the high and low Σ_{SFR} bins into high and low M_* bins. Unsurprisingly, we find that both of the M_* bins below this threshold show negligible evidence for broad emission, and both high Σ_{SFR} bins show strong outflows. Above the Σ_{SFR} threshold, the broad flux fraction is similar or perhaps somewhat larger in the high M_* bin. The FWHM of the broad line is larger for the high M_* bin (520 ± 11 km/s vs. 428 ± 30 km/s) and more blueshifted (-25 ± 4 km/s vs. -13 ± 7 km/s). This increase is smaller than a 'virial' scaling, $v_{out} \leq v_{esc} \sim v_c \sim {M_*}^{0.33}$ (Murray et al. 2005; Martin 2005), which would imply a factor of ∼1.8 in v_{out} between the two mass bins (logM_*= 9.85 and 10.61).

The SFR trend is linked to that of M_*, due to the strong correlation of M_* and SFR for 'main-sequence' SFGs at all redshifts. The $R_{1/2}$ trend is likely due to the higher Σ_{SFR} values for the more compact galaxies. The trend with inclination supports a bipolar outflow emerging perpendicularly from the plane of the star-forming disk, consistent with the results of Kornei et al. (2012, at z ∼ 1), Chen et al. (2010, at z ∼ 0), Bouché et al. (2012) and Bordoloi et al. (2011) (but see Law et al. (2012b)).

3.3.3 Local Electron Density of the Outflow

We estimate the ratio of the [SII] doublet in the broad and narrow components for a stack of the galaxy spectra, in order to constrain the star-forming gas and wind densities. The 14 galaxies used in this stack are selected such that they do not have strong OH sky features close to the location of the [SII] lines and have noticeable broad Hα components. We follow the fitting method described earlier in the text, except here we allow the amplitudes of the broad and narrow components in all nebular lines to vary, as opposed to, for instance, setting

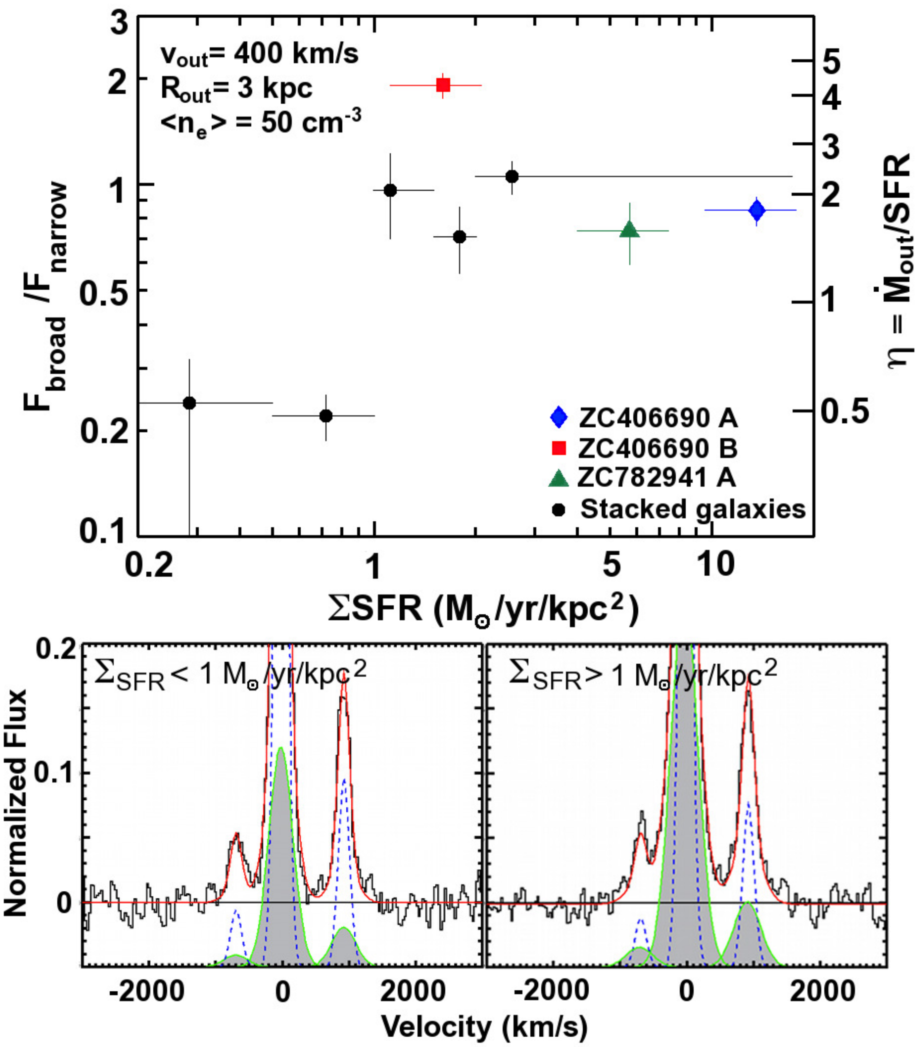

Figure 3.2: Dependence of the broad to narrow Hα flux ratio on Σ_{SFR}. Above: Stacks in 5 star formation surface density bins with 5–8 galaxies each. The right vertical axis shows the corresponding mass loading with the model explained in the text and wind parameters listed in the figure. The black points are the stacked galaxies and the colored symbols are individual star-forming clumps. The horizontal error bars for the binned points represent the range in Σ_{SFR} for the galaxies in each bin. The vertical error bars represent the rms of the range in F_{broad}/F_{narrow} values achieved by varying the stacks (for the binned points) and the measurement error (for the clumps). Below: Co-added Hα+[NII] spectra of low and high Σ_{SFR} bins with the data in black, the best fit shown in red, the narrow components shown in blue, and the broad components shown in green with grey shading.

[NII]/Hα (broad) equal to [NII]/Hα (narrow). The reduced χ^2 of the fit in the region of the Hα line is 1.71 and in the region of the [SII] lines is 0.97, while an imposed one-component fit yields reduced χ^2 values of 26.1 and 1.24, respectively, highlighting the challenges of attempting such a measurement.

For the narrow component, we find F([SII]λ6716)/F([SII]λ6731) = 0.99 $\pm$ 0.27, and for the broad component, we find that the ratio = 1.43 $\pm$ 0.40, corresponding to electron densities of 600 (+1000/-450) and 10 (+590/-10) cm^{-3}, respectively (Osterbrock 1989). The errors come from the fit uncertainties. Although our estimate is uncertain, the inferred local gas density in the outflow could be more than an order of magnitude less than the density of the star-forming regions (traced by the narrow component), consistent with a diffuse outflow. In Newman et al. (2012a), we assumed a mass outflow density of 100 cm^{-3}, based on two different outflow geometries and estimates of outflow density from local starburst galaxies (see e.g. Heckman et al. 1990). Thus we assume that these two values are upper and lower limits and take an average, resulting in a wind density of 50 cm^{-3}. Figure 3.3 shows the co-added spectrum along with the best fit.

A comparison of the narrow and broad [NII]/Hα ratios (0.17 $\pm$ 0.017 and 0.31 $\pm$ 0.028, respectively) with those of Newman et al. (2012a) in the clump and wind regions of ZC406690 shows that the narrow [NII]/Hα ratio is quite similar to the clump value and the broad ratio is very similar to that of the wind regions, which are affected by shocks. Therefore, not only does the broad [SII] ratio tell us about the density in the wind, but the broad [NII]/Hα value provides further evidence that the broad component derives from outflows.

3.3.4 Mass-loading of High-z Galactic Outflows

We assume the simplified outflow model of Genzel et al. (2011) and Newman et al. (2012a) for a warm ionized outflow with a radially constant outflow velocity and mass loss rate, to convert the F_{broad}/F_{narrow} ratio in Figure 3.2 into a mass-loading factor $\eta \equiv \dot{\mathrm{M}}_{\mathrm{out}}/\mathrm{SFR}$,

$$\dot{\mathrm{M}}_{\mathrm{out}} = M_w \times \frac{v_{out}}{R_{out}} = \frac{1.36 m_H}{\gamma_{H\alpha} n_e} \left(L_{H\alpha} \times \frac{F_{broad}}{F_{total}} \right) \frac{v_{out}}{R_{out}} \tag{3.1}$$

where $\dot{\mathrm{M}}_{\mathrm{out}}$ is the mass outflow rate, M_w is the instantaneous mass in the outflow, v_{out} is the average velocity of the outflow, R_{out} is the radial extent, m_H is the atomic mass, $\gamma_{H\alpha}$ is the Hα emissivity at $\mathrm{T}_e = 10^4$ K ($\gamma_{H\alpha} = 3.56 \times 10^{-25}$ erg cm^3 s^{-1}), n_e is the local electron density in the outflow, $L_{H\alpha}$ is the total extinction-corrected Hα luminosity, and F_{broad}/F_{total} is the fraction of the total flux in the broad component. We assume v_{out} = 400 km/s (see section 3.4) and R_{out} = 3 kpc. The latter is based on the spatial offset of outflowing gas from a massive star-forming clump described in Newman et al. (2012a), and from the finding in section 3.3.1 that the broad emission is extended to several kpc from the galaxy center. The emission line based estimate is independent of the collimation of the outflow. We adopt n_e = 50 cm^{-3} as the average *local* electron density, derived in the previous section. We note that if we assume a model wherein the average electron density varies as R^{-2}, as considered in Genzel et al. (2011), then our mass outflow rates will be lower by a factor of 4–5.

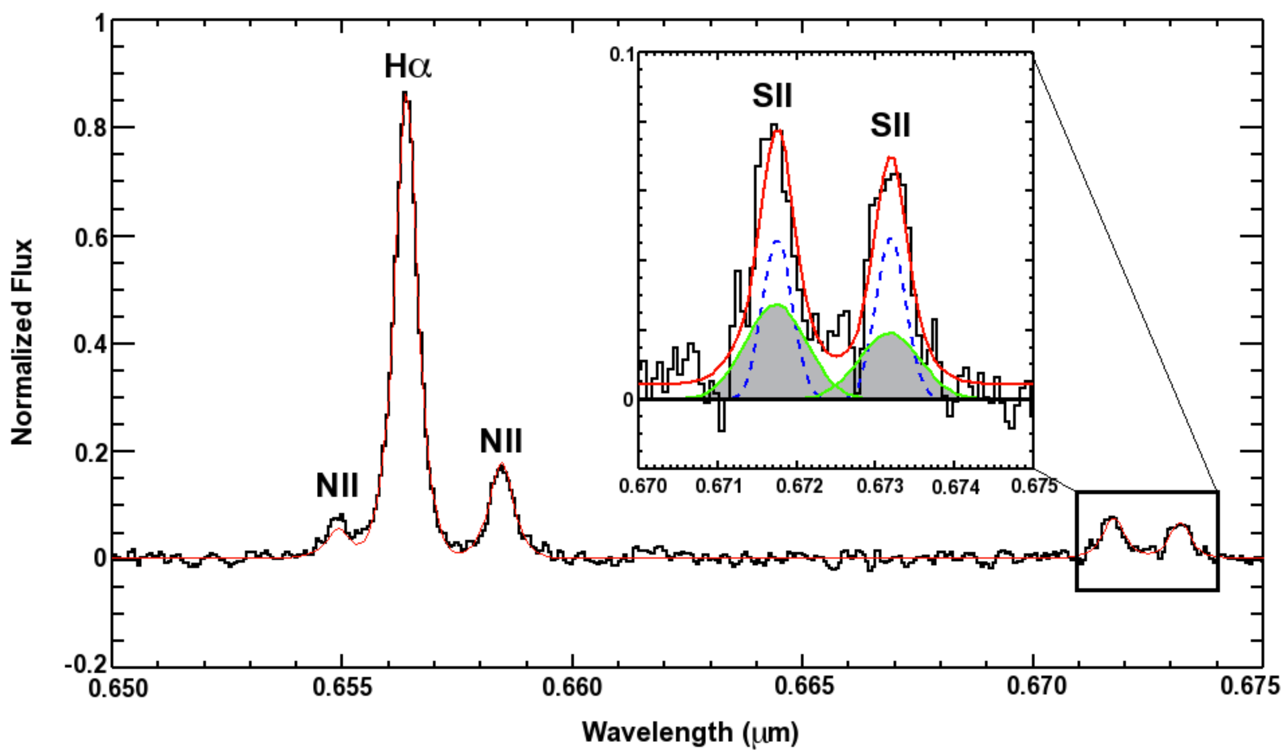

Figure 3.3: Co-added spectrum of 14 SFGs with [SII] detections that are free of OH contamination. The black line is the data, the red line is the best fit, and the green lines with grey shading (with FWHM = 407 km/s) and blue dashed lines (with FWHM = 197 km/s) (seen in the inset) are the broad and narrow Gaussian fits, respectively.

The inferred mass loading factors corresponding to the broad flux fraction are shown on the right-most y-axis in Figure 3.2. The mass-loading factors for galaxies below the Σ_{SFR} threshold are ~ 0.5 and above the threshold are ~ 2, albeit with an overall absolute uncertainty of at least a factor of 3. Despite the uncertainties, a mass loading factor of 2 is consistent with observations of both local starbursts (Heckman et al. 1990; Veilleux et al. 2005; Chen et al. 2010) and high-z SFGs (Pettini et al. 2000; Weiner et al. 2009; Steidel et al. 2010; Genzel et al. 2011; Bouché et al. 2012), as well as theoretical predictions (Murray et al. 2005; Davé et al. 2011; Hopkins et al. 2012).

3.4 Why Do the Outflows Depend so Strongly on Σ_{SFR}?

We propose that the strong dependence of η on Σ_{SFR} discussed in section 3.3.4 is mainly caused by the threshold that governs when star formation feedback can break out of the dense gas layer in the disk.

Following Ostriker & Shetty (2011) (see Equations 1 and 7), in a baryon dominated galactic disk in pressure equilibrium, the weight of the disk balances the pressure generated from star-formation feedback in the form of supernovae, stellar winds, HII regions, cosmic rays and radiation from the star-forming layer. If that pressure exceeds the weight of the disk, then a momentum-driven outflow is launched perpendicular to the galactic plane, with a threshold Σ_{SFR} ($M_\odot yr^{-1} kpc^{-2}$) of,

$$\Sigma_{SFR,th} = \frac{\pi G f_g}{2(P_{tot}/m_*)}\Sigma_d^2 = 0.9 \times \frac{f_{g,0.5} \times \Sigma_{d,500}^2}{(P_{tot}/m_*)_{1000}} \tag{3.2}$$

where G is the gravitational constant, (P_{tot}/m_*) is the characteristic total momentum injection per mass, Σ_d is the disk surface density, and f_g is the gas fraction, with fiducial values of 1000 km/s (Ostriker & Shetty 2011; Murray et al. 2005), 500 $M_\odot pc^{-2}$ (Erb et al. 2006b; Förster Schreiber et al. 2009) and 0.5 (Tacconi et al. 2010; Daddi et al. 2010a), respectively. Here, we have equated the weight of the gas above the disk (see: Ostriker & Shetty 2011, Equation 1, with an added dependency on f_{gas} since we only care about infalling gas) with the pressure from star formation feedback (see: Ostriker & Shetty 2011, Equation 7). This is similar to the 'Eddington limit' of momentum driven winds (Murray et al. 2011), which gives $\Sigma_{SFR,threshold} \propto v_c^{5/2} R^{-2}$, where v_c is the circular velocity.

The wind has a total momentum outflow rate,

$$\dot{M}_w v_\infty \leq \left(\frac{P_{tot}}{m_*}\right) SFR \tag{3.3}$$

where v_∞ is the outflow velocity at large distances from the mid-plane, implying a mass-loading factor,

$$\eta = \frac{\dot{M}_w}{SFR} \leq \frac{(P_{tot}/m_*)}{v_\infty} = 2.5 \times \frac{(P_{tot}/m_*)_{1000}}{v_{\infty,400}} \tag{3.4}$$

with $v_{\infty,400}$ in units of 400 km/s. This velocity is motivated by the observed outflow velocities in both low-z and high-z SFGs (Pettini et al. 2000; Martin 2005; Veilleux et al. 2005; Weiner et al. 2009; Steidel et al. 2010; Genzel et al. 2011) as well as from this work. The adopted value of the characteristic momentum injection is chosen assuming P_{tot}/m_* from radiation pressure $\sim$ 200–300 km/s (Ostriker & Shetty 2011) and that the direct momentum injection contributions of supernovae, stellar winds, HII regions and radiation pressure are all roughly comparable (Murray et al. 2005, 2010), giving a total (P_{tot}/m_*) of 1000 km/s. Here, we have assumed that energy-driven winds are unimportant and that the bulk of the ram pressure from SNe does not play a strong role until the gas has been lifted out of the disk (see: Murray et al. 2011).

This simple model predicts that for constant η the ability of an outflow to break out of the disk strongly depends on the star formation surface density, and this threshold value scales linearly with gas fraction and as the square of the disk surface density. Second, the mass loading of galactic winds above breakout and the threshold star formation surface density for breakout both depend on (P_{tot}/m_*). Thus, if one of these quantities can be determined for a galaxy of known properties, then the other can be predicted. The model also predicts that it is harder to launch a wind from a more massive galaxy (with larger v_c^4/R^2). This final prediction is also acquired by writing the threshold in terms of M_* by assuming (1) the $R_{1/2}$-M_* relation of Ichikawa et al. (2012) ($R_{1/2}\sim M_*^{0.14}$), (2) the SFR-M_* relation for normal SFGs (SFR = $M_*^{0.7}$ x $((1+z)/3.2)^{2.6}$) (Elbaz et al. 2007; Noeske et al. 2007) and (3) a constant gas depletion timescale ($t_{depl} = M_g/\mathrm{SFR} \sim 6.4$ x 10^8 yr, Tacconi et al. 2013). We note that the Ichikawa et al. (2012) relation was derived using K band continuum emission, while our $R_{1/2}$ are derived using Hα, so there may be some inconsistency. This gives an M_* threshold of $\sim$ few x 10^{10} $M_\odot$, such that it is easier for outflows to 'break-out' from galaxies below this threshold.

The first two predictions are met by the available data. For z$\sim$0 normal SFGs with $f_g \sim 0.07$ and $\Sigma_d \sim 500$ $M_\odot pc^{-2}$ (Catinella et al. 2010), Equation 3.4 suggests a critical breakout star formation surface density of $\sim$0.1 $M_\odot yr^{-1} kpc^{-2}$. And indeed, winds are only detected in compact star forming dwarfs and/or starbursts above $\sim$0.1 $M_\odot yr^{-1} kpc^{-2}$(Heckman et al. 1990; Veilleux et al. 2005; Chen et al. 2010), see also Murray et al. (2011). Mass loading factors for local galaxies with winds are estimated to be around 1 (Martin et al. 2012).

For the typical high-z SFGs presented in this paper ($f_g \sim 0.5$, $\Sigma_d \sim$ 500–1000 $M_\odot pc^{-2}$), Equation 3.2 suggests a breakout star formation surface density near or slightly above 1 $M_\odot yr^{-1} kpc^{-2}$, in remarkable agreement with our findings in section 3.3.2 and Figure 3.2. Above this threshold, Equation 3.4 predicts a mass loading of $\sim$2.5, again in good agreement with our observations. We caution that our determination of the mass loading factor in the previous section is dependent on a simplified model with fairly uncertain parameters, yet the agreement is encouraging.

A positive correlation of η with Σ_{SFR} (which was also observed by Chen et al. (2010)) is possible evidence against the scenario in which winds are launched by the energy of hot supernovae bubbles, as in this case the shorter cooling time of the dense gas suggests $\eta \propto \Sigma_{SFR}^{-1/2}$ (Hopkins et al. 2012), and could support the momentum-driven wind model.

However, the third prediction of the simple model (massive galaxies are less efficient at driving winds) does not appear to be met by our data. For the SFGs in the 'wind regime' ($\Sigma_{SFR} > 1$ $M_{\odot} yr^{-1} kpc^{-2}$) we do not see any significant variation of F_{broad}/F_{narrow} as a function of v_c, which is expected theoretically for momentum driven winds ($\eta \propto v_c^{-1}$, Murray et al. 2005; Oppenheimer & Davé 2006, 2008; Hopkins et al. 2012).

This finding as well as the approximate M_* independence of the observed F_{broad}/F_{narrow} ratio in our data surprisingly suggest that massive SFGs have mass loading factors that are similar to or higher than those of low mass SFGs (since $\eta \sim v_{out}$ in our model, and v_{out} scales positively with the SFR). If so, the volume averaged outflow rate and metal enrichment of the circum-galactic/inter-galactic medium at $z \sim 2$ may be dominated by massive galaxies just around the Schechter mass (logM_* ~ 10.65, Peng et al. 2010). Indeed, with a slope α of the main-sequence of SFGs (SFR $\propto m_*^{\alpha}$) ~ 0.7 or higher, the SFR (and thus the outflow rate, with constant η) increases faster with M_* than the volume density of SFGs decreases ($\Phi(M_*) \sim {M_*}^{-0.5}$, Peng et al. (2010)). We note that a massive galaxy dominance in the metal enrichment of the intracluster medium (ICM) is demanded by the fact that in clusters $\sim 2/3$ of the metal mass is contained in the ICM whereas only $\sim 1/3$ is still locked into stars and galaxies (Renzini 1997).

Further, the $z \sim 2$ M_* dependence of the mass-metallicity relation (Z $\sim {M_*}^{0.24}$, Erb et al. 2006b) may be primarily driven by the larger (diluting) gas fractions in low M_* SFGs, besides these galaxies driving winds more effectively ($M_g/M_* = t_{depl}$ x SFR/$M_* \sim {M_*}^{-0.3}$). In addition, if high-M_* galaxies are indeed ejecting this much mass, we may have uncovered a mechanism contributing to the quenching of star formation near the Schechter mass (Peng et al. 2010).

Chapter 4

The SINS/zC-SINF Survey of $z \sim 2$ Galaxy Kinematics: The Nature of Dispersion Dominated Galaxies

We analyze the spectra, spatial distributions and kinematics of Hα, [NII] and [SII] emission in a sample of 38, z $\sim$ 2.2 UV/optically selected star forming galaxies (SFGs) from the SINS & zC-SINF surveys, 34 of which were observed in the adaptive optics mode of SINFONI and 30 of those contain data presented for the first time here. This is supplemented by kinematic data from 43 z $\sim$ 1–2.5 galaxies from the literature. None of these 81 galaxies is an obvious major merger. We find that the kinematic classification of high-z SFGs as 'dispersion dominated' or 'rotation dominated' correlates most strongly with their intrinsic sizes. Smaller galaxies are more likely 'dispersion-dominated' for two main reasons: 1) The rotation velocity scales linearly with galaxy size but intrinsic velocity dispersion does not depend on size or may even increase in smaller galaxies, and as such, their ratio is systematically lower for smaller galaxies, and 2) Beam smearing strongly decreases large-scale velocity gradients and increases observed dispersion much more for galaxies with sizes at or below the resolution. Thus, out of our sample of 38 galaxies, only 2 or 3 would be classified as 'dispersion dominated' with higher resolution data. 'Dispersion dominated' SFGs may thus have intrinsic properties similar to 'rotation dominated' SFGs, but are primarily more compact, lower mass, less metal enriched and may have higher gas fractions, plausibly because they represent an earlier evolutionary state.

4.1 Introduction

At the peak of the galactic formation epoch at z$\sim$1–3, the rest-frame UV and Hα morphologies of most star forming galaxies near the 'main sequence' of the stellar mass-star formation plane (henceforth 'SFGs': Noeske et al. 2007; Daddi et al. 2007; Rodighiero et al. 2011; Peng et al. 2010) are typically irregular and in some cases dominated by several giant (kpc-size) star forming clumps (Cowie et al. 1995; van den Bergh et al. 1996; Elmegreen et al. 2004b, 2009b; Elmegreen & Elmegreen 2005, 2006; Genzel et al. 2006, 2008, 2011; Law et al. 2007, 2009, 2012c; Förster Schreiber et al. 2009, 2011a; Wuyts et al. 2012; Swinbank et al. 2012b,a). The ionized gas kinematics of these clumpy galaxies range from rotationally supported disks, especially among the more massive ($M_* \geq$ a few 10^{10} $M_\odot$) and bright (Ks AB $\leq$ 21.8) SFGs, to galaxies dominated by apparently random motions (Förster Schreiber et al. 2006, 2009; Law et al. 2007, 2009; Genzel et al. 2008, 2011; Wright et al. 2007, 2009; Shapiro et al. 2008; Cresci et al. 2009; van Starkenburg et al. 2008; Epinat et al. 2009; Lemoine-Busserolle & Lamareille 2010; Jones et al. 2012; Wisnioski et al. 2012; Swinbank et al. 2012b,a; Epinat et al. 2012). The latter class, which are especially common among the smaller and lower mass systems, often have average intrinsic velocity dispersions (corrected for instrumental broadening and beam smearing, and determined here from the outer regions of the galaxies), σ_0, larger than the inclination-corrected rotation velocities, v_{rot} (hereafter, 'dispersion dominated' SFGs) (Förster Schreiber et al. 2009). Despite these irregular morphologies, the fraction of major mergers is probably less than 30% (Shapiro et al. 2008; Förster Schreiber et al. 2009; López-Sanjuan et al. 2013) and stellar mass maps of z$\sim$1–2 SFGs are typically smoother and more symmetric than the light distributions (Wuyts et al. 2012). As a rule, rest-frame UV and optically-selected high-z SFGs exhibit large local random motions, with ratios of v_{rot} to σ_0 of less than 8. Hence even the rotationally dominated systems are thick ($H_z \sim$ 1 kpc: Elmegreen & Elmegreen 2006) and highly turbulent. Observations of CO rotational line emission indicate that z$\sim$1–3 massive SFGs have large ($\sim$30–60%) baryonic cold gas fractions and this cold molecular gas has a large velocity dispersion comparable to that of the warm ionized gas traced by Hα (Daddi et al. 2008, 2010b; Tacconi et al. 2008, 2010, 2013; Swinbank et al. 2011).

These basic observational properties (irregular morphologies, high gas fractions and large velocity dispersions) can be understood in a simple physical framework, in which global gravitational instability and fragmentation in marginally stable ($Q_{Toomre} \leq 1$), gas-rich disks naturally leads to large turbulence and the formation of giant star forming clumps (Noguchi 1999; Immeli et al. 2004a,b; Bournaud et al. 2007; Elmegreen et al. 2008; Genzel et al. 2008, 2011; Dekel et al. 2009; Bournaud et al. 2010; Genel et al. 2012a). The buildup of these marginally stable disks in z>1 SFGs is plausibly fueled mainly by smooth accretion of gas and/or minor mergers (Kereš et al. 2005, 2009; Dekel & Birnboim 2006; Bower et al. 2006; Kitzbichler & White 2007; Ocvirk et al. 2008; Davé 2008; Dekel et al. 2009; Oser et al. 2010; Cacciato et al. 2012; Ceverino et al. 2012).

While the buildup of early star forming disks may be explained by this scenario, it is less clear how the dispersion dominated galaxies fit in. There are several possible explanations for what they are (see e.g.: Förster Schreiber et al. 2009; Law et al. 2007, 2009, 2012c; Jones et al. 2010; Epinat et al. 2012), including:

(1) an earlier evolutionary stage with higher gas fractions and lower masses, in which case the simple fragmentation scenario discussed above would lead to larger velocity dispersions,

(2) intrinsically smaller rotationally supported disks that masquerade as dispersion dominated because the instrumental 'beam smearing' hides the rotational signal,

(3) the result of dissipative major mergers that would drive chaotic motions,

(4) giant clumps in face-on star forming disks, where the rest of the disk material has too low surface brightness to be detected, or

(5) some combination thereof.

In this paper we present and analyze new high-quality SINFONI/VLT integral field (IFU) spectroscopy with natural and laser guide star adaptive optics (AO) (Eisenhauer et al. 2003; Bonnet et al. 2004) of 30 z∼2 SFGs. We combine this with 4 AO and 4 seeing-limited data sets which have been presented previously by our group (Förster Schreiber et al. 2009; Cresci et al. 2009; Genzel et al. 2011), but contain new analysis here. For these 38 SINS/zc-SINF galaxies, we find that 43% were classified as 'dispersion dominated' based on previous seeing limited observations and according to the criteria of Förster Schreiber et al. (2009). We add to our measurements another 35 AO data sets and 8 spatially well-resolved (with $R_{1/2}$>4.5 kpc) seeing limited data sets of z = 1–2.5 SFGs from the literature. The combined data of 81 SFGs provide interesting new constraints on the nature of the 'dispersion dominated' SFG population. We adopt a ΛCDM cosmology with Ω_m=0.27, Ω_b=0.046 and H_0=70 km/s/Mpc (Komatsu et al. 2011), as well as a Chabrier (2003) initial stellar mass function (IMF).

4.2 Observations and Analysis

4.2.1 Source selection, observations and data reduction of SINS/zC-SINF galaxies

Our base sample are 34 SFGs from the SINS and zC-SINF surveys of Hα+[NII] integral field spectroscopy in z ∼ 1.5–2.5 SFGs obtained with SINFONI on the ESO VLT that were observed in both seeing-limited and AO mode. These galaxies are drawn from the parent seeing-limited SINFONI samples described in Förster Schreiber et al. (2009) and Mancini et al. (2011). The main criteria for selecting these galaxies from the seeing-limited sample were a clear detection of Hα in one hour seeing-limited SINFONI data, the proximity of a suitably bright AO reference star, and the goal of ultimately covering as much of the range in stellar mass, SFR and kinematic properties of the parent no-AO SINS/zC-SINF sample as possible. The resulting AO sample has nearly identical distributions in M_* and SFR as the parent no-AO sample in terms of range, median and offset from the main sequence. In addition to the SINS/zC-SINF AO sample, we include 4 large galaxies ($R_{1/2}$>4.5 kpc) observed only in seeing-limited mode with sufficient signal to noise ratio (S/N) and spatial resolution to robustly determine the kinematics (Förster Schreiber et al. 2009; Mancini et al. 2011). Adding these larger objects does not bias our results as we do not aim for a 'complete' sample, merely one that has as large a range in galaxy properties and kinematic types as possible. Thus these galaxies only give us more information on rotationally-supported objects. We exclude obvious major mergers from our sample, but keep possible minor mergers, assuming that the central object in a minor merger retains its kinematic integrity to a significant extent. Note, however, that this criterion only eliminated 5 out of originally 86 objects (when including the additional datasets from the literature - see next Section).

The SINS and zC-SINF surveys were selected either from their U_nGR colors satisfying the 'BX' criteria (Steidel et al. 2004; Adelberger et al. 2004; Erb et al. 2006b; Law et al. 2009) or based on K band imaging via the 'BzK' criterion for 1.4 <z <2.5 SFGs (Daddi et al. 2004b). In addition, a few galaxies were included based on their stellar masses and SFRs from the GMASS Spitzer 4μm survey (Kurk et al. 2009, 2013), and one galaxy was selected from the GDDS survey based on a secure redshift and evidence for on-going star-formation from the UV data (Abraham et al. 2004).

These galaxies sample the $z \sim 2$ SFG 'main sequence' in the stellar mass – star-formation rate plane between stellar masses of $10^{9.2}$ and $10^{11.5}$ $M_\odot$, and star formation rates between ∼13 and 850 $M_\odot yr^{-1}$ (see Figure 4.1), covering the same range in M_* and SFR as the parent samples. For the AO data, we employed SINFONI in the 0.05"x0.1" pixel scale, with either laser guide star (LGS) or natural guide star (NGS) AO, resulting in angular resolutions of ∼0.20" (equivalent to 1.7 kpc at $z \sim 2$) full width at half maximum (FWHM) after median filtering by 3x3 pixels. The 4 larger rotationally supported systems were observed in SINFONI's seeing limited mode and 0.125"x0.25" pixel scale, resulting in a median FWHM ∼0.56", sufficient to resolve these SFGs (Förster Schreiber et al. 2009). These sources are included in the analysis (and not other seeing-limited only galaxies), because their large spatial extents allow well-resolved kinematical analysis. The on-source integration times for each galaxy from our sample range between 2 and 23 hours, with a median of about 5.8 hours, resulting in high quality, spatially resolved spectra for most sources. This sample includes 6 AGN, identified by the presence of AGN signatures in their rest-UV spectrum, [NII]/Hα ratio, and/or X-ray or MIPS 24μm data when available (e.g., see Förster Schreiber et al. 2009). These would not affect our σ_0 measurements, which are taken away from the center, but could potentially affect σ_{tot} (the total Gaussian line width integrated over the source). A discussion of the properties of 9 individual galaxies of the AO sample can be found in several of our earlier SINS papers (Genzel et al. 2006, 2011; Cresci et al. 2009; Förster Schreiber et al. 2009; Newman et al. 2012a), with new data here for 5 of those objects. A detailed discussion of the full AO sample will be presented in Förster Schreiber et al. (2013a).

We used the software package SPRED and custom routines for optimizing the background/OH airglow subtraction for the data reduction. The point spread function (PSF) FWHM was measured by fitting a 2D Gaussian profile to the combined images of the PSF calibration star taken throughout the observations of a galaxy. More information on the specifics of these observations and the data reduction can be found in Förster Schreiber et al. (2009), Mancini et al. (2011), and Förster Schreiber et al. (2013a).

We created Hαemission line, velocity and velocity dispersion maps from the reduced data cubes by using the Gaussian-fitting procedure LINEFIT (Davies et al. 2011), with errors derived from the noise cube. For more information on our standard SINS data reduction methods and analysis tools we refer to Schreiber et al. (2004), Davies (2007), Förster Schreiber et al. (2009), and Mancini et al. (2011).

4.2.2 Additional datasets from the literature

We also include in our analysis 43 additional z $\sim$ 1–2.5 SFGs from the literature (Table 4.1) deriving from IFU datasets with beam-smearing corrected kinematic information. These include:

- 9 galaxies from the BX- (rest-UV color/magnitude) selected z = 1.5–2.5 AO sample from Law et al. (2009, 2012a) taken with OSIRIS.
- 6 galaxies from the BM-selected z = 1.5–1.7 AO sample from Wright et al. (2007, 2009) taken with OSIRIS.
- 12 galaxies from the z = 1.3–1.45 AO sample from Wisnioski et al. (2011) selected for strong [OII] emission from the Wiggle-Z Dark Energy (UV-selected) survey, also taken with OSIRIS.
- 5 z $\sim$ 1.45 galaxies from Swinbank et al. (2012b,a), taken from the HiZELS imaging survey of the COSMOS and UDS fields, selected for narrow band Hα flux and observed with SINFONI in the AO mode.
- 8 z = 1-1.6 MASSIV galaxies selected from the VVDS spectroscopic survey observed in seeing-limited mode with SINFONI (Lemoine-Busserolle & Lamareille 2010; Epinat et al. 2012; Contini et al. 2012; Vergani et al. 2012). Here we only chose galaxies with $R_{1/2}$>4.5 kpc, such that their kinematics could be well resolved without AO.
- 3 additional z = 1.2–1.4 galaxies from Epinat et al. (2012) observed in the AO mode of SINFONI.

These galaxies were selected such that they were in the redshift interval 1–2.5, were not classified as major mergers, and had either AO data or seeing-limited data with $R_{1/2}$>4.5 kpc. We do not include z<1 studies (Puech et al. 2007, 2009; Neichel et al. 2008, e.g.), or z$\sim$1 slit spectroscopy (Weiner et al. 2006; Kassin et al. 2007) in the analysis, but emphasize that these investigations also find evidence for large random motions.

Figure 4.1 shows the location of our entire sample in the SFR-M_* plane. As can be seen from the left panel, SFGs are well-sampled from a SFR of 10 to 500 $M_\odot$/yr and over 2 decades of stellar mass, from $\sim$2x10^9 to 2x10^{11} $M_\odot$, and from the right panel, we see that both rotation and dispersion-dominated galaxies are widely distributed.

Table 4.1: Source Selection

Dataset	**z**	**Galaxies**	**AO?**	**Instrument**	**Reference**
SINS/zC-SINF	1.5—2.5	34	AO	SINFONI/VLT	this paper[1]
SINS/zC-SINF	1.5—2.5	4	seeing-lim.	SINFONI/VLT	Förster Schreiber et al. (2009)[2]
BX/BM-selected	1.5–2.5	15	AO	OSIRIS/Keck	Wright et al. (2007, 2009); Law et al. (2009, 2012a)[3]
Wiggle-Z	1.3–1.45	12	AO	OSIRIS/Keck	Wisnioski et al. (2011)
HiZELS	1.4–1.5	5	AO	SINFONI/VLT	Swinbank et al. (2012b,a)
MASSIV	1.2–1.4	3	AO	SINFONI/VLT	Epinat et al. (2012); Contini et al. (2012)[4]
MASSIV	1–1.6	8	seeing-lim.	SINFONI/VLT	Lemoine-Busserolle & Lamareille (2010) and Epinat et al. (2012); Contini et al. (2012)

[1] Seeing-limited data of all of these galaxies has been presented in Förster Schreiber et al. (2009) and Mancini et al. (2011). Data of 9 of these galaxies have been presented in Genzel et al. (2006, 2011), Cresci et al. (2009), Förster Schreiber et al. (2009), and Newman et al. (2012a), although 5 of these now contain new observations. The full AO data set will be described in detail in the forthcoming Förster Schreiber et al. (2013a).
[2] New analysis of this data is presented here.
[3] 3 galaxies from this sample were not included as they overlap with the SINS/zC-SINF sample.
[4] These galaxies were selected from the total sample such that they had kinematic information based on the Hα line from either H- or K-band, as the AO system on the VLT does not work as well in the J-band.

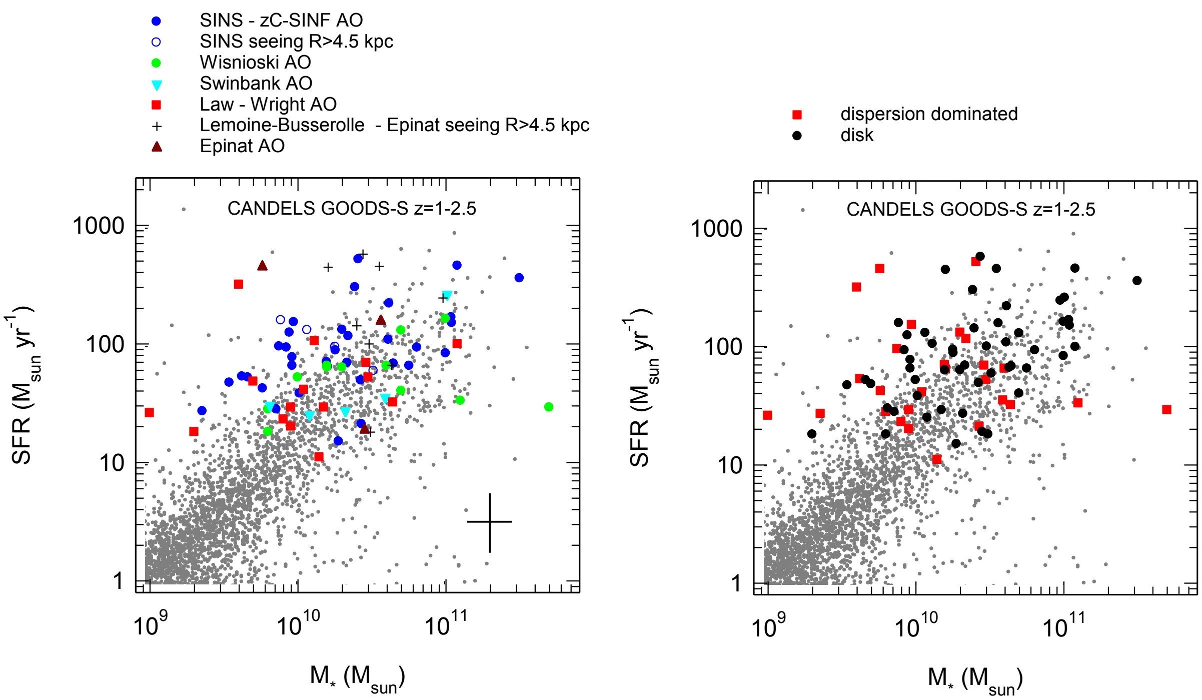

Figure 4.1: The star-formation rate/stellar mass plane. The grey points are from z = 1–2.5 galaxies from the CANDELS survey in the GOODS-S field. The left panel shows the distribution of galaxies from different parent samples used in our analysis. The blue closed (and open) circles are from the SINS/zC-SINF galaxies presented in this paper observed in AO (seeing-limited) mode. The red squares are from Law et al. (2009, 2012a) and Wright et al. (2009), the cyan inverted triangles are from the SHiZELS survey presented in Swinbank et al. (2012b,a), the maroon triangles denote the AO galaxies from Epinat et al. (2012), the green circles represent the AO data from the WiggleZ survey (Wisnioski et al. 2011), and the black '+'s denote galaxies from Epinat et al. (2012) and Lemoine-Busserolle & Lamareille (2010) that have $R_{1/2}$>4.5 kpc and were observed in seeing-limited mode. The right panel shows the same distribution of galaxies according to their identification as dispersion- or rotation-dominated. Here, black circles represent galaxies determined to be rotation dominated, and red squares denote galaxies determined to be dispersion-dominated. Note that wherever possible, we used averages of the Hα- and SED-derived SFRs.

4.2.3 Determination of Galaxy Properties for the SINS/zC-SINF sample

Stellar masses, star formation rates and stellar ages are derived from SED modeling of broad-band photometry in Förster Schreiber et al. (2009), Mancini et al. (2011) and Förster Schreiber et al. (2011a) and assume either constant star formation histories or exponentially declining models with Bruzual & Charlot (2003) tracks. The ages are highly uncertain and should be interpreted in the sense that the bulk of galaxy light comes from stars younger than this "age", and as such are best used as relative and not absolute ages. The star formation rates are taken as an average of those calculated from SED modeling and Hα-based star formation rates, derived using SFR=L(Hα)/(2.1x10^{41} erg/s) ($M_{\odot}yr^{-1}$) (Kennicutt 1998, corrected for a Chabrier (2003) IMF), where L(Hα) is extinction corrected based on the Calzetti et al. (2000) reddening law with $A_{V,gas}$=2.3x$A_{V,SED}$. Förster Schreiber et al. (2009) and Wuyts et al. (2011b) have shown that an extra attenuation factor of ∼2.3 is a good representation of the global extinction towards HII regions relative to the bulk of starlight for $z \sim 2$ SFGs.

We calculate molecular gas masses (M_{gas}) and surface densities (Σ_{gas}= 0.5x$M_{gas}/(\pi(R_{1/2})^2)$ from the Hα- and SED-derived SFRs using the star formation rate/molecular gas mass relation calibrated from the IRAM Large Program of CO in z∼1–2 SFGs ($t_{depl} = 1.5 \times (1+z)^{-1}$ Gyr, Tacconi et al. 2013). This simple linear relation has been shown to hold for both local and high-z SFGs, yielding $M_{gas}(M_{\odot}) = t_{depl} \times$ SFR ($M_{\odot}$/yr) (Bigiel et al. 2008; Tacconi et al. 2010, 2013; Saintonge et al. 2012) down to ∼1 kpc scales, with scatter in the relation of ∼0.3 dex due to the variation in slope and normalization from various studies and also intrinsic scatter in the relation (see: Genzel et al. 2010; Daddi et al. 2010a; Tacconi et al. 2013). The dynamical mass is calculated as, $M_{dyn} = 2R_{1/2}(v_{rot}^2 + 3.4 \times \sigma_0^2)/G$, where v_{rot} is the inclination-corrected rotation velocity and σ_0 is the intrinsic galaxy dispersion. The factor of 3.4 accounts for pressure support (asymmetric drift) in an exponential distribution.

Inclinations were determined from the minor axis to major axis ratio of the Hαsurface brightness distribution. We found overall good agreement between the morphological axes and those determined from kinematics, however smaller objects tended to exhibit a large scatter in the position angles determined from the two methods. In addition, some of the larger, more face-on systems have their axis ratios and position angles partially affected by small-scale regions of enhanced surface brightness. Following Law et al. (2012c), we considered the intrinsic z-thickness of high-z SFGs in deriving sin(i) (assuming $<z>/<R>$=0.2), although the inferred inclinations are not significantly different from those in the thin disk approximation. This technique assumes that the light distribution is intrinsically circularly symmetric. However, Law et al. (2012c) find fewer b/a∼1 systems than expected for a population of randomly oriented inclined disks. Wuyts et al. (in prep.) find the same trend at all z from 0 to 2, although with lower amplitude at lower redshift. Independent of whether this deviation from circular symmetry in the light distribution is due to an intrinsically triaxial light or matter distribution or whether it's due to the distribution of clumps distorting the symmetry, this results in additional uncertainties in our derived inclinations, mainly for face-on systems.

Intrinsic (corrected for the spatial resolution) half-light radii are based on 2D exponential profile (i.e. Sersic profile, I(R) = ln(I_0) - k$R^{1/n}$, with index n = 1) fits to the Hα surface brightness distributions using the code GALFIT (Peng et al. 2002) following the methodology described by Förster Schreiber et al. (2011a) (details for the present SINS/zC-SINF AO sample are given by Förster Schreiber et al. (2013a)). For six cases (BX389, BX482, GMASS-2540, ZC405501, ZC406690, and ZC410041), a Gaussian profile (Sersic n = 0.5) was found to provide a significantly better representation of the data and we adopted the sizes derived from these Gaussian fits. Sersic profiles with n $\lesssim$ 1 are motivated by the previous analysis of a subset of six SINS galaxies (Förster Schreiber et al. 2011a), and the more recent result from a larger sample of z $\sim$ 1.5 SFGs by Nelson et al. (2013).

The oxygen abundances are derived from the observed [NII]/Hα flux ratio using the Pettini & Pagel (2004) calibration: 12+$\log_{10}$(O/H) = 8.90 + 0.57 $\times$ $\log_{10}$([NII]/Hα). This calibration is most often used for high-z galaxies with emission line data of only H$\alpha$and [NII], and thus we choose it for simplicity of comparison with previous work. We note that there are several uncertainties associated with this particular calibration (see e.g., Kewley & Ellison 2008), so it is taken as a relative measure of gas-phase abundance among our objects.

4.2.4 Determination of Kinematic Properties

For each galaxy, we computed the observed velocity gradient (Δv_{grad}) as the maximum velocity difference across the source from the velocity map produced from the data cube. The total Gaussian line width integrated over the source (σ_{tot}) is calculated from the width of the Hαline from the spatially integrated spectrum for each galaxy. For SFGs with a substantial component of rotation or large-scale orbital motion, σ_{tot} is strongly affected or even dominated by beam-smeared rotation. However, all of the SINS/zC-SINF galaxies presented in this paper are resolved well enough in either the AO or seeing-limited data to estimate the average intrinsic local velocity dispersion (σ_0) from the velocity dispersion maps, and we minimize the effects of beam smearing by measuring the observed velocity dispersion in the outer parts of the source. Note that all quoted velocity dispersions have been corrected for the instrumental response function and are thus intrinsic quantities of the source. We determine the rotational velocity (v_{rot}) by correcting Δv_{grad} for our best-fit inclination.

In determining the kinematic properties for the other galaxies in our larger sample, we attempt to use as consistent a method as possible. Epinat et al. (2012) and Lemoine-Busserolle & Lamareille (2010) use a similar method to ours for determining v_{rot} and σ_0, so we use the values presented in their papers. As with our method, they create maps of the velocity and dispersion fields for their galaxies that are corrected for instrumental resolution and additionally subtract (in quadrature) a beam-smearing component as estimated from thin rotating-disk models. Davies et al. (2011) has shown that deriving kinematic parameters from such modeling has the advantage of not being systematically biased by beam smearing and most often produces more correct results. However, there can be some inaccuracy in the resulting parameters due to low S/N, and Davies et al. (2011) suggest that extracting σ_0 from the outer regions of the galaxy (as we do with the SINS/zC-SINF galaxies) could help alleviate this issue. Either way, these two techniques should provide similar results. For the SHiZELS galaxies from Swinbank et al. (2012b), we take v_{rot} and σ_0 from their Figure 4.4, assuming the values in the outer regions of the galaxies, for consistency with our method. We note the the values they give for σ are almost all larger than the ones we assume. This is consistent with the bias towards higher σ_0 values demonstrated by Davies et al. (2011), which is found when correcting for beam smearing without generating disk models or without ignoring the central regions of the galaxy. We do the same for the Wright et al. (2009) galaxies, using their velocity and velocity dispersion maps. For the Law et al. (2009, 2012a) galaxies, we take their v_{rot} and σ_0 values, which were derived from fitting a Gaussian to the line profile from each pixel and flux-weighting to determine an average. As mentioned in their work and Davies et al. (2011), this produces an upper-limit for σ_0 once beam-smearing is accounted for, and this is reflected in Figures 4.5 through 4.9. Wisnioski et al. (2011) do not derive σ_0 values in a way that is comparable to our values, so we use their dataset for v_{rot} comparison only.

We follow Förster Schreiber et al. (2009) and operationally define 'dispersion dominated' and 'rotation dominated' SFGs as having $\Delta v_{grad}/2\sigma_{tot}$ <0.4 and ≥0.4, respectively, for both AO and seeing-limited data. This operational divide is based on disk models of masses and sizes roughly spanning the range observed in our sample and with typical beam-smearing of seeing-limited data. Once corrected for inclination and beam smearing, it closely corresponds to the more intuitive physical definition $v_{rot}/\sigma_0<1$ and ≥1. None of the galaxies in our sample are obvious major mergers but several may be minor mergers with a kinematically related companion galaxy within 10–20 kpc. For these, we consider the kinematic properties of the entire system.

We caution that a detection of a velocity gradient is certainly required but is by itself not sufficient to prove that a galaxy is rotating. If the velocity gradient is along the morphological major axis and at the same time, a peak of velocity dispersion is present near the morphological centroid, the evidence becomes more convincing. This second line of evidence is present for most of the galaxies in the SINS/zC-SINF sample. The ultimate, but hardest, criterion is the detection of a symmetric 'spider diagram' pattern in the iso-velocity contours whose shape/curvature is consistent with the inclination estimated from the minor to major axis ratio (van der Kruit & Allen 1978). This most demanding proof is not reached by any of the compact dispersion dominated systems, and only by very few of the large disks/rings.

4.3 The Nature of Dispersion Dominated SFGs

As discussed in the Introduction, all investigations of the spatially resolved ionized gas dynamics have consistently found that z∼1–3 SFGs possess large internal random motions, in addition to large scale ordered velocities, such as rotation (in a disk), or orbital motion (in an interacting or merging system). In a significant fraction (anywhere from 20-90%, depending

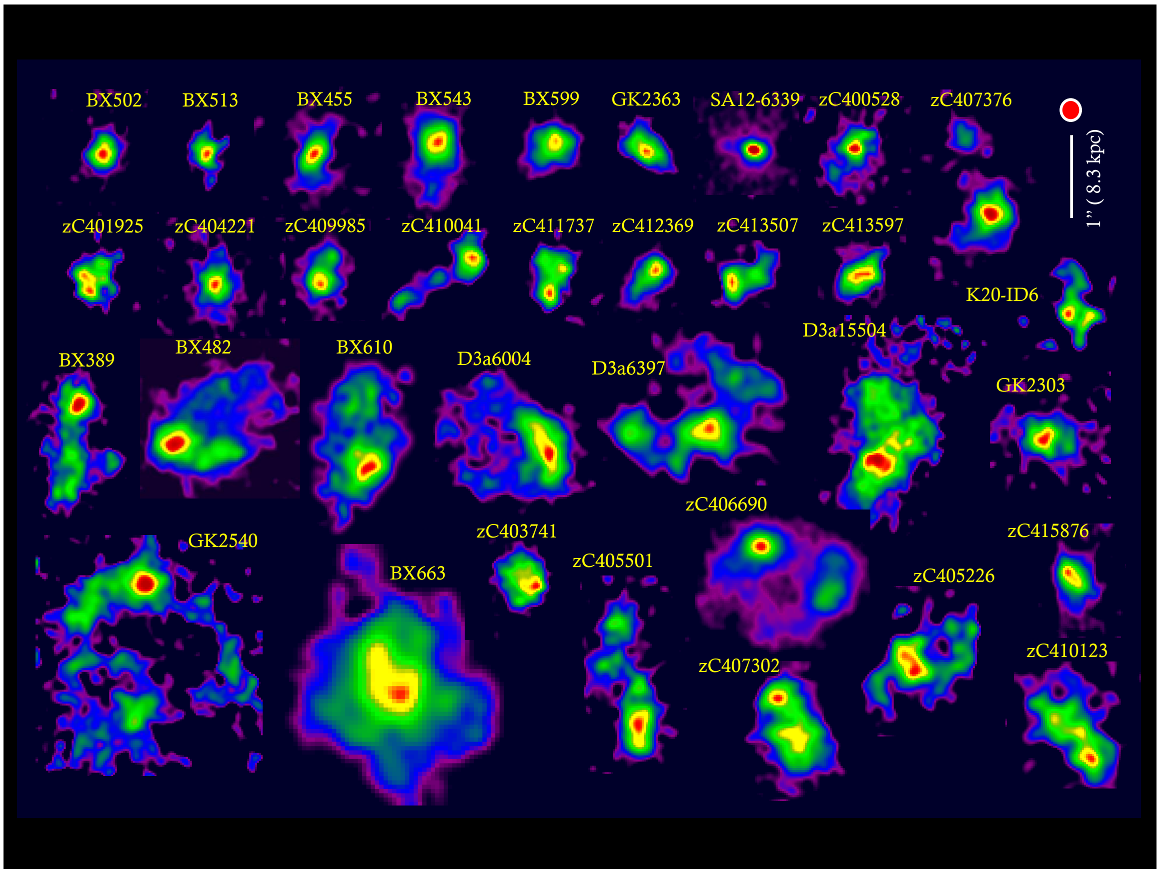

Figure 4.2: Integrated Hαmaps in AO mode (0.2–0.3" FWHM) of the 34 SFGs in our (AO) sample. The top two rows contain the dispersion dominated SFGs (as defined by the criterion $(\Delta v_{grad}/(2\text{x}\sigma_{tot}))_{seeing} \leq 0.4$, Förster Schreiber et al. (2009), and the rest are rotation dominated. The maps were interpolated on a pixel scale of 0.025" and are all plotted on the same angular scale. The typical FWHM resolution is shown as a red circle. The dispersion dominated galaxies tend to be more compact than the rotation dominated galaxies with the peak of their Hαemission in the center.

on the sample and definition of kinematic parameters) of the available IFU samples, the random motion component even appears to dominate, similar to what is seen in spheroidal galaxies. This characteristic feature of high-z galaxies is surprising, since in a gas rich system, supersonic turbulence should dissipate on a dynamical time scale ($\sim 10^{7-7.5}$ yr), unless it is continuously replenished.

4.3.1 Dispersion Dominated Galaxies are Small

Figure 4.2 shows postage stamps of the velocity-integrated Hα emission maps of 34 of the SINS and zC-SINF AO data sets. The galaxies are ordered such that the 17 galaxies in the top two rows have $\Delta v_{grad}/2\sigma_{tot}$ below or very near 0.4, and are thus classified as 'dispersion dominated' based on the seeing limited data of Förster Schreiber et al. (2009) and Mancini et al. (2011). According to the same criterion, the other 17 galaxies in Figure 4.2 are rotationally supported. None of the 34 is an obvious major merger, but the presence of a spatially well-separated secondary component in six of these SFGs (BX543, BX513, zC409985, zC410041, zC407376, zC407302) may be evidence for an ongoing minor merger (mass ratio >3:1), although in some cases it is difficult with the data in hand to distinguish unambiguously between bright clumps in large disks and minor merger systems.

Figure 4.2 immediately shows that the most obvious characteristic of dispersion dominated systems is their small size. If we look at those galaxies with $R_{1/2} \leq 3$ kpc, then most of these 13 smaller systems fulfill one or several of the kinematic definitions of dispersion dominated galaxies as introduced in Section 4.2.4,

$$(\Delta v_{grad}/(2 \times \sigma_{tot}))_{seeing} \leq 0.4 \tag{4.1}$$

$$(\Delta v_{grad}/(2 \times \sigma_{tot}))_{AO} \leq 0.4 \tag{4.2}$$

$$v_{rot}/\sigma_0 \leq 1 \tag{4.3}$$

Comparison of seeing limited (FWHM ∼0.56") and AO-scale (FWHM ∼0.20") data of the same galaxies shows that the classification as dispersion or rotation dominated can depend strongly on angular resolution. This is demonstrated in Figures 4.3 and 4.4, which show the velocity and velocity dispersion fields for Q1623-BX455 and GMASS-2363 in both seeing and AO modes. As the galaxies are small ($R_{1/2}$∼0.2"), the seeing limited data (resolution ∼ 0.5") do not resolve them and appear to confirm their dispersion dominated classification. However, with the AO data (resolution ∼ 0.2"), both galaxies appear to be inclined rotating disks, based on the first two criteria for rotation outlined at the end of section 4.2 (velocity gradient along the morphological major axis and peak in velocity dispersion near the morphological center), yet like most high-z galaxies, neither exhibit the 'spider diagram' required for a more definitive proof.

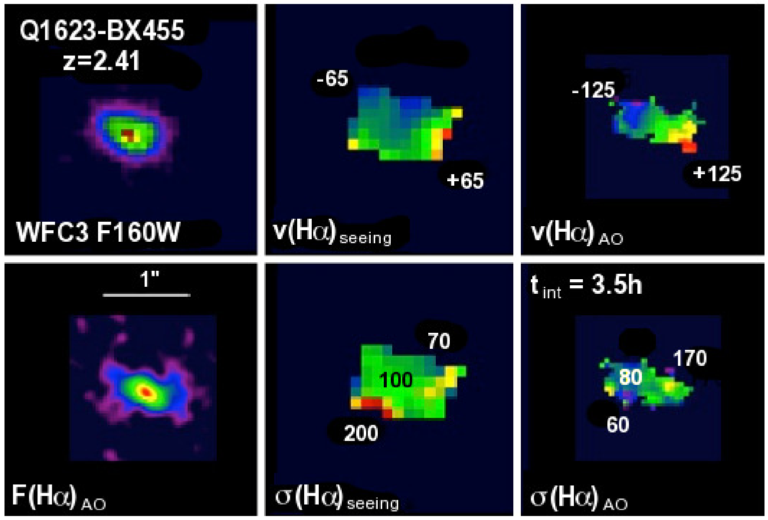

Figure 4.3: Top row, left to right: HST WFC3 (Law et al. 2012c) image, seeing-limited velocity field, AO velocity field. Bottom row, left to right: HαAO image, seeing-limited velocity dispersion field and AO velocity dispersion field of Q1623-BX455 (Förster Schreiber et al. 2009). Much of the rotation apparent from the AO velocity field is beam-smeared out with the seeing-limited data.

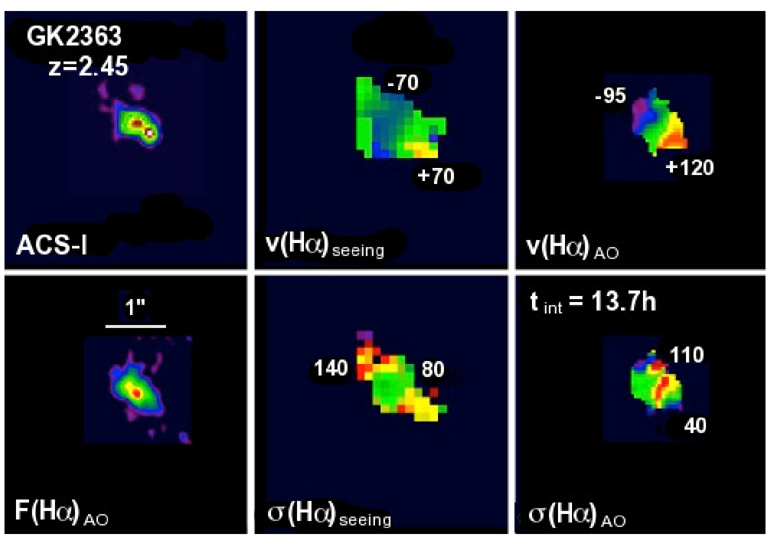

Figure 4.4: Top row, left to right: HST ACS I-band image, seeing-limited velocity field, AO velocity field. Bottom row, left to right: HαAO image, seeing-limited velocity dispersion field and AO velocity dispersion field of GMASS-2363 (Förster Schreiber et al. 2009).

4.3.2 Impact of Resolution on Kinematic Classification

In order to explore the impact of instrumental resolution on the classification (scenario 2 from Section 4.1) of galaxies as dispersion- or rotation-dominated, we used the sample of 34 SINS/zC-SINF galaxies, for which we have both seeing limited and AO resolution data, taken with the same instrument and analyzed with the same tools. We compare the location of these galaxies in the $\Delta v_{grad}/(2 \times \sigma_{tot})$ vs. $R_{1/2}$ plane in Figure 4.5 for both seeing-limited data (left panel) and AO data (middle panel). The shift to higher $\Delta v_{grad}/(2 \times \sigma_{tot})$, and thus more rotation-dominated classification, with higher resolution data is clear. We also show our entire sample in the v_{rot}/σ_0 versus $R_{1/2}$ plane in the right panel.

It is apparent that for all IFU data sets the dispersion dominated classification correlates with the intrinsic source size (smaller galaxies are more likely dispersion dominated), although they are not perfectly matched. But as we see from the first two panels, this classification also depends on the ratio of resolution to source size, such that poorly resolved galaxies are very likely classified as dispersion dominated. Given the criteria above, formally 41% of the 34 SINS/zC-SINF galaxies are classified as dispersion dominated based on seeing limited data. That fraction drops to 6–9% for the same galaxies using AO data. If we include 1σ error bars, up to 59% of the galaxies could be classified as dispersion dominated with seeing limited data and less than 35% with AO data.

In turn, the strong majority of the SINS/zC-SINF SFGs observed with AO can then be characterized by a velocity gradient along a single axis that is identical with or close to the morphological major axis. This suggests that rotation dominates the larger scale velocity field, although the observed pattern could also be matched by orbital motion in a binary minor merger in a few cases. However, we do not detect symmetric double light distributions or velocity reversals in any of the SFGs in our sample, which would be indicative of a major merger.

The empirical assessment drawn from Figure 4.5 is supported by creating simple toy models of turbulent but rotationally supported disks with intrinsic $v_{rot}/\sigma_0 \sim 1$–5. We "observe" model disks with varying sizes, masses and inclinations with seeing and AO scale resolutions and analyze them in the same way as our SINS/zC-SINF data. Their location in the empirical $\Delta v_{grad}/2\sigma_{tot} - R_{1/2}$ and $v_{rot}/\sigma_0 - R_{1/2}$ planes overlaps with the majority of the data. A fraction of the model disks indeed come to reside in the locus of 'dispersion dominated' galaxies, although they are intrinsically rotationally supported.

Finally, we carry out weighted linear fits to the data in log-log space (i.e. $\log(v_{rot}/\sigma_0)$ vs. $\log(R_{1/2})$) and calculate the formal significance of the slope differing from 0. The resulting best-fit slope and significance for data in the right panel of Figure 4.5 (and the remaining Figures) is presented in Table 4.2.

A similar dependence of kinematic classification on resolution was discussed in Jones et al. (2010) (see also: Gonçalves et al. 2010). They found that without the boost in spatial resolution provided by gravitational lensing, many of the galaxies that they identified as rotating disks would not be distinguishable from mergers or dispersion dominated sources based on their velocity profiles, even with the use of AO. However, we caution that our

Table 4.2: Significance of Correlation with Kinematic Parameters

Parameter 1	**Param. 2**	**Lin. Slope of Fit**	**Sign.**[1]	**See Fig.:**
$\log(v_{rot}/\sigma_0)$	$\log(R_{1/2})$	0.77 ± 0.12	6.4	4.5
$\log(v_{rot})$	$\log(R_{1/2})$	0.62 ± 0.094	6.6	4.6
$\log(\sigma_0)$	$\log(R_{1/2})$	-0.14 ± 0.05	2.8	4.6
$\log(M_{dyn})$	$\log(v_{rot}/\sigma_0)$	1.19 ± 0.097	12.3	4.7
$\log(M_*)$	$\log(v_{rot}/\sigma_0)$	0.54 ± 0.14	3.9	4.7
$\log(f_{gas})$	$\log(v_{rot}/\sigma_0)$	-0.028 ± 0.05	0.56	4.8
12+log(O/H)	$\log(v_{rot}/\sigma_0)$	0.1 ± 0.046	2.2	4.8
$\log(\Sigma_{SFR})$	$\log(v_{rot}/\sigma_0)$	-0.89 ± 0.18	4.9	4.9

[1] Significance of best fit linear slope as opposed to slope of 0.

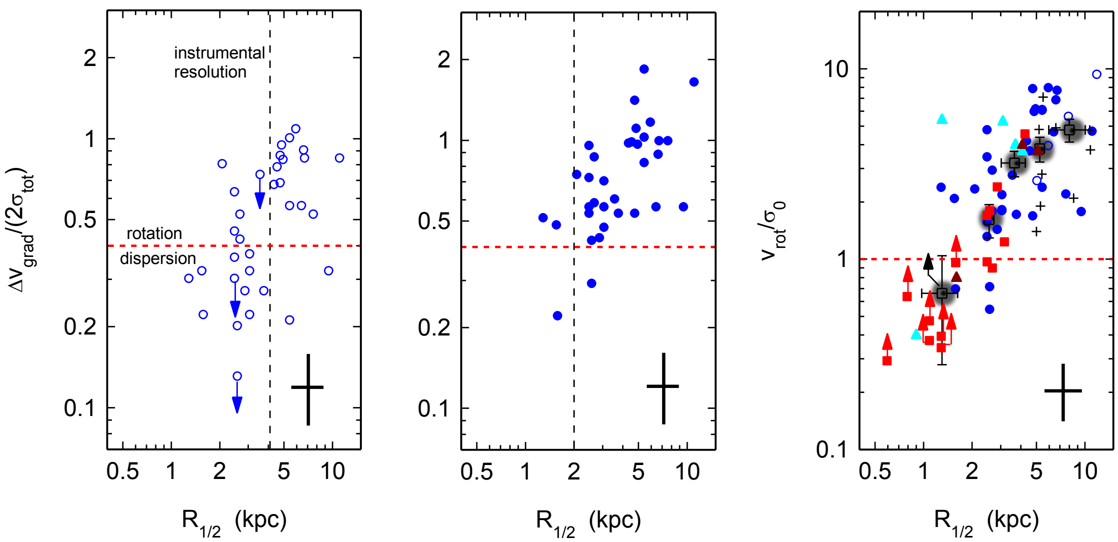

Figure 4.5: Dependence of the ratio of rotation to dispersion on the half light source radius ($R_{1/2}$) and resolution. Left panel: seeing-limited SINS/zC-SINF data (Förster Schreiber et al. 2009; Mancini et al. 2011). Middle panel: AO SINS/zC-SINF data (this paper and Förster Schreiber et al. 2013a). Right panel: Combined AO and seeing-limited data for galaxies that have sufficient angular resolution for dynamical modeling to obtain the inclination corrected v_{rot} and the beam smearing corrected σ_0 (i.e. all galaxies with AO data and seeing-limited only galaxies with $R_{1/2}$>4.5 kpc). The colored symbols are the same as for the left panel of Figure 4.1. Grey filled circles denote the median-binned values in four radius bins with horizontal error bars representing the standard deviation in the bins and vertical error bars representing the 1σ uncertainty. Many of the same galaxies are plotted in all three panels (for the SINS data). The horizontal dashed red lines mark the operational divide between dispersion and rotation dominated SFGs for the corresponding criteria for each panel. The vertical dashed black lines in the left and middle panels mark the FWHM spatial resolution of the data. Typical 1σ error bars for individual measurements are plotted at the bottom of each panel. Many of the galaxies characterized as dispersion dominated according to the seeing-limited data (left panel), would be considered rotation dominated with the higher-resolution AO data (middle panel) or with full dynamical modeling (right panel), and an important factor in the kinematic classification is the ratio of the galaxy size to the instrumental resolution.

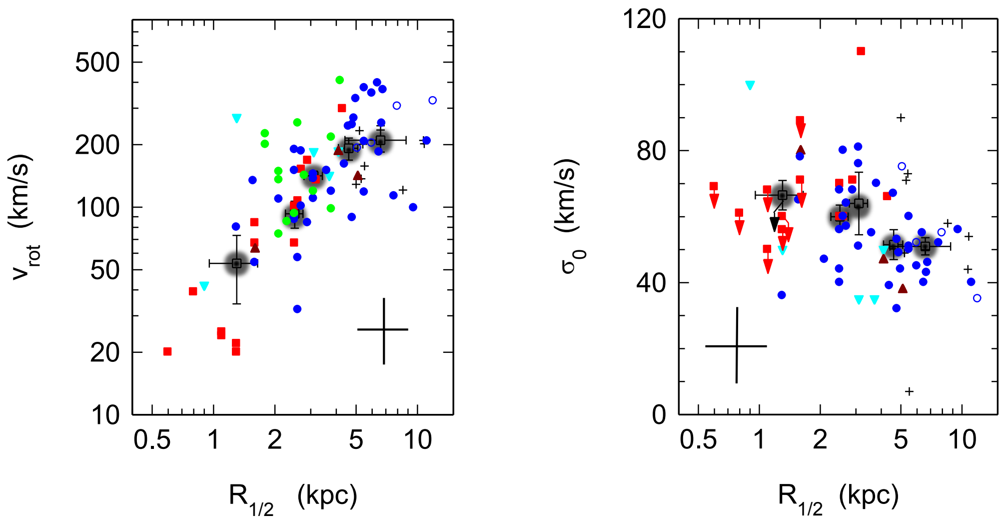

Figure 4.6: Dependence of v_{rot} (left panel) and σ_0 (right panel) on $R_{1/2}$. The data symbols are the same as in Figures 4.1 and 4.5. The strong trend in the left panel can be well fit by a linear relation: $\log(v_{rot}) = 0.62\ (\pm 0.094) \times \log(R_{1/2}) + 1.9\ (\pm 0.06)$ (see Table 4.2). In contrast, the right panel does not appear to show a significant trend, considering that many of the red data points (those from Law et al. 2009, 2012a) are strictly upper limits to σ_0. Thus the trend for smaller galaxies to be dispersion dominated is in part due to the combination of a near constant value of the velocity dispersion, and a linear increase of rotation velocity with size. We note that the characteristic error bars do not include potential additional uncertainties due to deviations from circular symmetry. However, these uncertainties really only strongly influence near face-on systems, which are very few in this data set.

sources are generally much larger than those in the Jones et al. (2010) work ($<R_{1/2}> \sim 2$ kpc), and will thus suffer less beam smearing with the use of AO even without the added spatial resolution of gravitational lensing.

4.3.3 Why Are Small Galaxies More Likely to be Dispersion Dominated?

The last section has shown that resolution effects can make an intrinsically rotation dominated system appear to be dispersion dominated if it is small, especially with seeing limited data. However, the middle and right panels of Figure 4.5 show that $\Delta v_{grad}/(2\sigma_{tot})$ and v_{rot}/σ_0 increase with radius even for well-resolved data sets, and even at AO resolution, there remain a number of dispersion dominated SFGs (mostly from the literature samples), for which the classification cannot be an instrumental effect. What causes this intrinsic dependence on size?

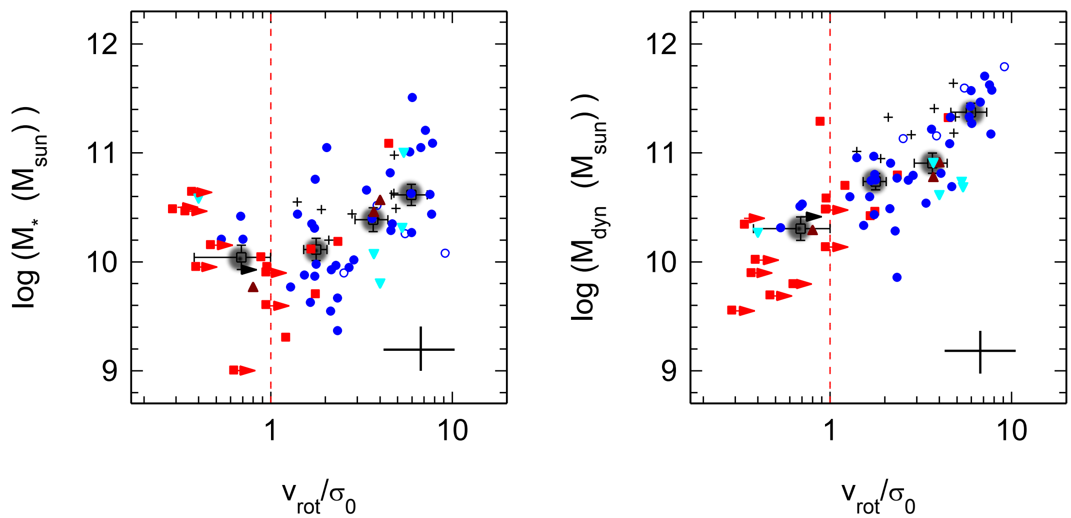

Figure 4.7: Dependence of stellar mass (left) and dynamical mass (right) on v_{rot}/σ_0. Symbols are the same as in Figures 4.1, 4.5 and 4.6.

In Figure 4.6, we plot the rotation velocity (corrected for inclination) and the intrinsic velocity dispersion (corrected for beam-smearing) as a function of $R_{1/2}$. Rotation velocity increases strongly with $R_{1/2}$ but there is no strong trend with velocity dispersion and the running median suggests that σ_0 is constant or perhaps slightly decreasing with $R_{1/2}$. The best fit weighted power law to the data in Figure 4.6 yields $v_{rot} = 59(\pm13)\times R^{0.73(\pm0.18)}$, but a linear slope is also consistent with the data within the 2σ fit error, which would be physically motivated by centrifugally supported baryonic disks of constant angular momentum parameter embedded in a virialized dark matter halo (Mo et al. 1998). Figure 4.6 thus shows that small galaxies are intrinsically more likely to be dispersion dominated because of the near-constant value of the local velocity dispersion in all high-z SFGs. Such a near constant value ($<\sigma_0>\sim 60 \pm 10$ km s^{-1}) may be caused by star formation feedback or by the dissipation of gravitational energy within and at the outer edge of the disk (Immeli et al. 2004a,b; Westmoquette et al. 2007; Bournaud et al. 2009; Agertz et al. 2009; Ceverino et al. 2010; Genzel et al. 2008, 2011; Genel et al. 2012a,b; Elmegreen & Burkert 2010; Krumholz & Burkert 2010).

4.3.4 Dependence on Stellar Mass, Gas Fraction and Age

Figure 4.7 shows that dispersion dominated galaxies tend to have smaller stellar and dynamical masses, in agreement with the earlier conclusions of Förster Schreiber et al. (2009), Law et al. (2009), Wisnioski et al. (2011), and Epinat et al. (2012). From the right panel of Figure 4.1, we see that while the dispersion dominated population (on the AO scale) is

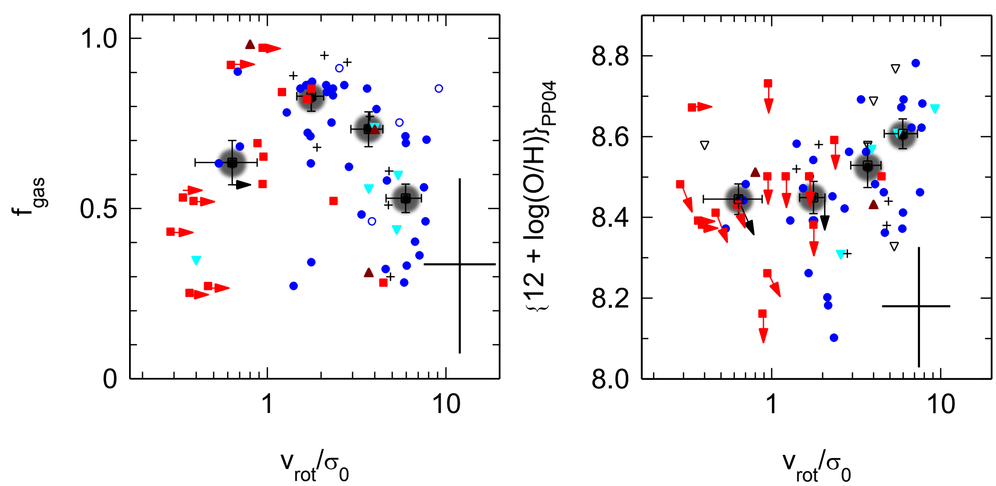

Figure 4.8: Dependence of baryonic gas fraction (f_{gas}=($M_{mol-gas}$/($M_{mol-gas}$+M_*)) (left panel) and gas phase oxygen abundance (right panel) on v_{rot}/σ_0. Symbols are the same as in Figures 4.1 and 4.5 to 4.7. For the MASSIV sample, the gas masses and Hαhalf-light radii are listed in Vergani et al. (2012) and the metallicities in Queyrel et al. (2012). Gas fraction and metallicity are correlated with kinematical type, such that dispersion dominated galaxies are more gas rich and slightly more metal poor.

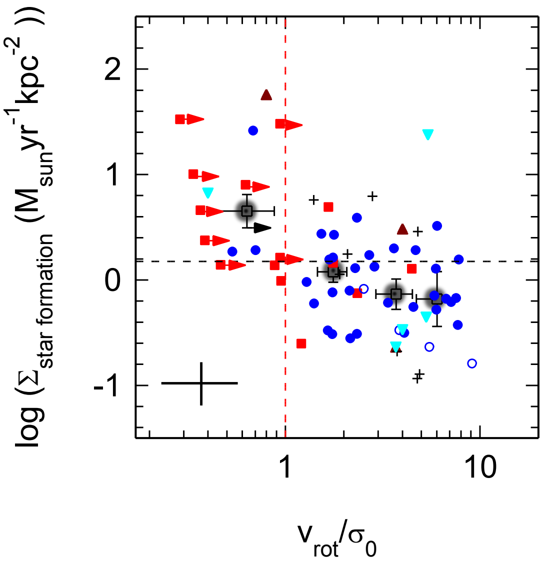

Figure 4.9: Dependence of star formation rate surface density (Σ_{SFR}= 0.5 SFR/π($R_{1/2}$)^2) on v_{rot}/σ_0. The symbols are the same as in Figures 4.1 and 4.5 to 4.8. The threshold for strong $z \sim 2$ galactic-scale outflows observed by Newman et al. (2012b) and marked by the black dashed line is at $\Sigma_{SFR} \sim$ 1.5 $M_\odot yr^{-1} kpc^{-2}$.

mostly found toward lower stellar masses, there is still substantial overlap with the location of disks. Thus, it seems that the best separation between the two kinematic populations is in terms of size and dynamical mass.

Figure 4.8 shows that the gas fraction (f_{gas}=($M_{mol-gas}$/($M_{mol-gas}$+M_*)) may be correlated with v_{rot}/σ_0 , but that this trend becomes far more uncertain for the dispersion dominated objects. While there is a large range in gas fraction for the dispersion dominated objects, some have gas fractions as large as 90%, much higher than for most of the larger rotating disks. These gas fractions are larger than those found by Tacconi et al. (2013) based on CO observations from Plateau de Bure for a sample of massive (M_*>3×10^{10} $M_\odot$) SFGs at z = 1.2 and z = 2.2. This is likely because of a combination of the lower masses and above-main sequence location of many dispersion dominated galaxies (see right panel of Figure 4.1). Tacconi et al. (2013) have shown that gas fractions increase with decreasing stellar mass and with increasing offset from the star-forming 'main sequence' in the stellar mass - SFR plane.

There is a modest difference in the strength of the [NII] line relative to the Hα line between the dispersion and rotation-dominated sub-samples, implying a metallicity trend (see Figure 4.8). We stack the spectra of the SINS/zC-SINF galaxies by kinematic type, and find that the 'dispersion dominated' sub-sample has <F[NII]6584/FHα>= 0.13 (±0.01), while the 'rotation dominated' sub-sample has <F[NII]6584/FHα>= 0.19 (±0.01), consistent with the larger stellar masses of the 'rotation dominated' sub-sample and the mass-metallicity relation

(Tremonti et al. 2004; Erb et al. 2006b; Mannucci et al. 2009). The errors here derive from the uncertainty in the fitting of the emission lines. These averages do not include the galaxies identified to contain AGN.

As found in Newman et al. (2012b), z$\sim$2 SFGs with Σ_{SFR}>1 $M_{\odot} yr^{-1} kpc^{-2}$ have evidence for strong outflows, based on the ratio of broad Hα emission to narrow Hα emission (which likely traces star-forming gas in the disk). We find that dispersion-dominated galaxies generally have higher Σ_{SFR} than the sample as a whole (Figure 4.9). When coupled with Figures 4.6 and 4.7, this suggests that outflows may be stronger (or more likely) in galaxies with smaller rotation velocities and dynamical masses (as suggested by theoretical models, e.g. Murray et al. 2005).

When comparing the mean ages of 'rotation' or 'dispersion dominated' galaxies from the SINS/zC-SINF sample we also see a relative trend. When classified using seeing-limited data, the 'dispersion dominated' sample has a mean age of 460 Myr, while the 'rotation dominated' galaxies have a mean age of 690 Myr. This contrast is even stronger when using AO data or the v_{rot}/σ_0 criteria, wherein the mean ages are 120 and 650 Myr for the dispersion and rotation dominated samples, respectively. These ages pertain to the stars providing the bulk of the rest-frame UV and optical radiation, as these dominate the photometry used in our SED analysis.

We thus find that high-z SFGs may be classified as 'dispersion dominated' for two main reasons, namely that (a) intrinsic rotation is beam-smeared by insufficient spatial resolution, and (b) the small galaxy size is accompanied by lower rotation velocity, which when coupled with the nearly constant floor of velocity dispersion leads to a low v_{rot}/σ_0 ratio. These conclusions enable us to reflect on the question posed in the Introduction about what these objects really are. We find that:

> (1) The 'dispersion dominated' objects may indeed be an earlier evolutionary stage of larger disks due to the lower stellar and dynamical masses, lower metallicities and possibly higher gas fractions. We discuss this possibility in more detail in the following section.
>
> (2) It also appears that they are (smaller) rotating disks, with rotation that is masked by beam-smearing due to insufficient resolution in addition to intrinsically lower rotation velocities (likely due to their smaller dynamical masses).
>
> (3) A fraction of the 'dispersion dominated' systems may also be the product of a recent major merger. While the parent samples from which our SFGs were drawn already only contained a few binary systems with kinematic properties consistent with major mergers (which we have intentionally excluded, see methods of e.g. Shapiro et al. 2008; Förster Schreiber et al. 2009), and the new AO observations discussed here have not uncovered new major merger candidates of somewhat smaller size, there could still be late stage major mergers in our sample masquerading as 'dispersion dominated' if they are sufficiently compact.

(4) It is less likely that the 'dispersion dominated' objects are merely large clumps in low surface brightness disks. First, if this were the case, we would not expect to see more rotation with higher spatial resolution. In addition, when we stack all of the galaxies classified as dispersion dominated based on seeing-limited data, we find Sersic indices of ~ 0.5–1 with $r_{eff} \approx <R_{1/2}>$, and without excess extended emission. Law et al. (2012c) also find that a stack of their 'Type I' galaxies is well fit by an n $\sim$ 1 Sersic profile, with $r_{eff} = 1.36$ kpc.

4.4 Implications for Galaxy Evolution

Based on this combined sample of IFU datasets, we are able to hypothesize on how the 'dispersion dominated' galaxies affect our picture of galaxy evolution. In addition to the smaller sizes and potentially higher gas fractions, we also found that dispersion dominated galaxies tend to have lower stellar masses, younger ages (based on SED fitting), and lower inferred metallicities on average than rotation dominated galaxies. One can imagine a scenario in which the smaller dispersion-dominated galaxies are "seeds" for the larger and more massive rotating disks, and these larger galaxies at z $\sim$ 2.2 have merely evolved sooner. As these "seeds" continue to rapidly accrete gas, form stars and expel winds, they also grow in size, build up their stellar masses, increase in metallicity and decrease in gas fraction. We find that these dispersion dominated galaxies are more likely to have star formation surface densities above the wind 'break-out' threshold proposed by Newman et al. (2012b) than their larger disky counterparts, implying that they drive outflows more efficiently than the latter ones do (see also: Law et al. 2012b). The higher stellar masses will eventually stabilize the disks, and the larger sizes and increased rotation velocities will decrease the Toomre scale, shrinking the size of the star-forming regions (the clumps). A similar mechanism for the growth of dispersion-dominated galaxies into rotationally-supported disks was also suggested by Law et al. (2012b). We note that our dispersion-dominated galaxies are on average not the same as the high-z compact star-forming galaxies ("blue nuggets") recently reported on by Barro et al. (2013), which they propose will soon quench and become compact quiescent galaxies. While two of the galaxies from our sample (BX502 and SA12-6339) do meet their mass/size criteria, the remainder of our smaller galaxies have much lower stellar masses (by a factor of ~2–5).

The picture we have presented, in which stellar mass builds up in the centers of galaxies through this 'compact dispersion-dominated' phase is supported by additional observational evidence. Based on 3D-HST H$\alpha$and rest-frame R-band data of z $\sim$ 1 SFGs, Nelson et al. (2012) find that Hαemission is typically more extended than continuum emission, but that this is less often the case for the smallest objects ($r_{H\alpha}$ <3 kpc) that have star formation surface densities >1 $M_{\odot} yr^{-1} kpc^{-2}$, suggesting inside-out growth. Similarly, Wuyts et al. (2012) find that z $\sim$ 1–2 SFGs from the CANDELS survey typically have large stellar bulges with high extinction and/or old stellar ages and UV-bright star-forming clumps with little or no excess in stellar mass at outer radii.

These unstable z $\sim$ 2.2 galaxies will grow until they are 'mass quenched' with increasing probability as they grow in mass beyond the Schechter mass of $\sim 10^{10.7-11}$ $M_{\odot}$(Conroy & Wechsler 2009; Peng et al. 2010), which requires a tripling of mass based on the median stellar mass of the galaxies in our sample. Given an average specific star formation rate of $\sim$ 2 Gyr^{-1}, this process would take around 1.3 Gyr. Thus the most massive of our z $\sim$ 2.2 SFG sample will be effectively quenched by z $\sim$ 1.5. Indeed, highly unstable and morphologically disturbed SFGs are more rarely seen at this later epoch (Kassin et al. 2012), also owing to the fact that galactic gas accretion has slowed by this time (Birnboim et al. 2007). The remainder may evolve into L^* galaxies, as suggested by Conroy et al. (2008).

Another possibility for the evolution of dispersion dominated objects is that they are the product of clump migration and coalescence at the centers of larger disks, and are therefore the descendants of rotation dominated galaxies. However, if the clumps are formed by gravitational instability, we would expect them to be continuously produced in the unstable, gas-rich disks, and we should see some brighter emission outside the center of the dispersion dominated galaxies. In addition, this scenario is at odds with the lower stellar masses, younger ages and lower metallicities of the dispersion dominated systems. Indeed, one would expect that the first galaxies to experience clump coalescence would be the most massive rather than the least massive ones.

4.5 Conclusions

This paper presents, for the first time, a side-by-side comparison of high quality deep AO and seeing-limited kinematic data of the same galaxies for a larger number of objects. We note that this unprecedented data leads us to similar conclusions as those made in previous work. Based on IFU data of 81 star forming galaxies at z=1–2.5, we compare the sub-samples of galaxies known as dispersion and rotation dominated. We find that the characterization of a galaxy into one of these kinematic groups is a strong function of the galaxy size. Small galaxies are much more likely to fall in the category of 'dispersion dominated' galaxies due to insufficiently resolved rotation (especially with seeing-limited observations) and also as a result of the almost constant floor of velocity dispersion across all sizes paired with the linear increase of rotation velocity with size. Many galaxies that are considered 'dispersion dominated' from more poorly resolved data actually show evidence for rotation with higher-resolution data.

Despite the finding that galaxies characterized as 'dispersion-dominated' often show evidence for rotation with higher spatial resolution data, they have different average properties than 'rotation dominated' galaxies. They tend to have lower stellar and dynamical masses, higher gas fractions, younger ages and slightly lower metallicities. We suggest that these galaxies could be precursors or 'seeds' to larger rotating galaxies, as they accrete more mass onto the outer regions of their disks. Our AO-based results provide important insights for the analysis and interpretation of seeing-limited IFU data, such as will become available for large samples with KMOS, through the quantitative assessment presented of the effects of beam-smearing on the observed kinematics of real galaxies.

Chapter 5

Nebular Excitation in $z \sim 2$ Star-forming Galaxies from the SINS and LUCI Surveys: The Influence of Shocks and AGN

Based on high-resolution, spatially resolved data of 10 $z \sim 2$ star-forming galaxies from the SINS/zC-SINF survey and LUCI data for 12 additional galaxies, we probe the excitation properties of high-z galaxies and the impact of active galactic nuclei (AGN), shocks and photoionization. We explore how these spatially-resolved line ratios can inform our interpretation of integrated emission line ratios obtained at high redshift. Many of our galaxies fall in the 'composite' region of the z $\sim$ 0 [NII]/Hα versus [OIII]/Hβ diagnostic (BPT) diagram, between star-forming galaxies and those with AGN. Based on our resolved measurements, we find that some of these galaxies likely host an AGN, while others appear to be affected by the presence of shocks possibly caused by an outflow or from enhanced ionization parameter as compared with HII regions in normal local star-forming galaxies. We find that the Mass-Excitation (MEx) diagnostic, which separates purely star-forming and AGN hosting local galaxies in the [OIII]/Hβ versus stellar mass plane, does not properly separate $z \sim 2$ galaxies classified according to the BPT diagram. However, if we shift the galaxies based on the offset between the local and $z \sim 2$ mass-metallicity relation (i.e. to the mass they would have at z $\sim$ 0 with the same metallicity), we find better agreement between the MEx and BPT diagnostics. Finally, we find that metallicity calibrations based on [NII]/Hα are more biased by shocks and AGN at high-z than the [OIII]/Hβ/[NII]/Hα calibration.

5.1 Introduction

Optical and near-infrared surveys over the last 15 years have firmly established that star-forming galaxies (SFGs) at $z \sim 2$ have very different morphological structure in their rest-frame UV/optical light than their local counterparts (e.g. Cowie et al. 1995; van den Bergh et al. 1996; Elmegreen et al. 2004b, 2009b; Elmegreen & Elmegreen 2005, 2006; Genzel et al. 2006, 2008, 2011; Law et al. 2007, 2009, 2012b; Förster Schreiber et al. 2009, 2011a; Wuyts et al. 2012; Swinbank et al. 2012b,a; Jones et al. 2010, 2012). Although a majority are characterized as rotating disks with kinematic analysis, they exhibit clumpy structure and elevated velocity dispersions, indicating much larger scale heights than local disks (Elmegreen & Elmegreen 2006; Förster Schreiber et al. 2006, 2009; Law et al. 2007, 2009; Genzel et al. 2008, 2011; Wright et al. 2007, 2009; Shapiro et al. 2008; Cresci et al. 2009; van Starkenburg et al. 2008; Epinat et al. 2009; Lemoine-Busserolle & Lamareille 2010; Jones et al. 2012; Wisnioski et al. 2012; Swinbank et al. 2012b,a; Epinat et al. 2012; Newman et al. 2013). In addition, their star formation rates (SFR), star formation rate surface densities (Σ_{SFR}) and interstellar pressures are more similar to those of local starbursting galaxies than local normal star-forming disks (Newman et al. 2012a).

Given the differing physical conditions in local and high-z SFGs, one might expect this to be reflected in their nebular excitation properties. Indeed, high-z SFGs often fall in the 'composite' region of the BPT (Baldwin et al. 1981) diagram (the plane of [OIII]/Hβ versus [NII]/Hα), between HII regions and AGN, coincident with the location of many local starburst galaxies (Tecza et al. 2004; Shapley et al. 2005; Kewley et al. 2006; Erb et al. 2006a; Liu et al. 2008; Trump et al. 2013; Juneau et al. 2011; Kriek et al. 2007; Hayashi et al. 2009; Yabe et al. 2012; Yuan et al. 2013b). In fact, Liu et al. (2008) and Brinchmann et al. (2008) have found among local SDSS galaxies a positive correlation between relative offset from the main star-forming HII branch of the BPT diagram toward the 'composite' region and ionization parameter, SFR, and electron density. They have suggested that higher values of these galaxy parameters could explain the position of high-z galaxies in the BPT diagram as well. Conversely, the offset of $z \sim 2$ galaxies from the star-forming branch of the BPT diagram could also be due to the presence of AGN or shocks from large-scale outflows. Unfortunately, weak AGN can be difficult to identify in integrated line ratios, but spatially-resolved data can help to uncover them as demonstrated by the case study of a z = 1.6 galaxy by Wright et al. (2009, 2010). More recently, Newman et al. (2012a) found that for two star-forming clumps in a $z \sim 2$ SFG, elevated [NII]/Hα and [SII]/Hα ratios were at least in part due to shocks from a galactic-scale outflow originating from the clumps, with no evidence for an underlying AGN. Determining the cause(s) of the offset of high-z galaxies in the BPT diagram is instrumental for understanding the physical properties of these objects and in particular the contribution of AGN to their evolution.

In addition to understanding the physical properties of these galaxies, quantifying the effects of shocks and AGN on emission line ratios will help us to better estimate their gas phase metallicity. These metallicities are essential for properly understanding the interplay between gas inflow, outflow and star formation at the peak epoch of the star formation rate density at z $\sim$ 2–3 (Lilly et al. 2013). Rest-optical nebular line ratios calibrated locally are the main technique used for measuring metallicity at high-z. However, different diagnostics can give very different results (see e.g. Kewley & Ellison 2008), and if the [NII]/Hα ratio is indeed elevated in many high-z galaxies by either the physical conditions in HII regions, the presence of shocks or an AGN, metallicities determined using this ratio could be systematically overestimated.

In this work, we present K-, H- and/or J-band datasets for 22 z $\sim$ 1.4–2.5 rest-UV/optically selected SFGs obtained as part of the SINS/zC-SINF and LUCI surveys (Förster Schreiber et al. 2009; Mancini et al. 2011; Kurk et al. 2013). Thus for each galaxy, we measure Hα, [NII], [OIII], and Hβ fluxes. The faintness of these lines and the requirement that all, or a significant subset of them should be observable between the bright night sky OH lines in the near-IR atmospheric windows make such studies from the ground very challenging. The SINS/zC-SINF and LUCI surveys allowed us to cull a sizeable amount of suitable targets for a first exploration of spatially-resolved metallicities and excitation in massive $z \sim 2$ SFGs. We adopt a ΛCDM cosmology with Ω_m=0.27, Ω_b=0.046 and H_0=70 km/s/Mpc (Komatsu et al. 2011), as well as a Chabrier (2003) initial stellar mass function (IMF).

5.2 Observations and Analysis

5.2.1 Source selection, observations and data reduction of SINS/zC-SINF galaxies

Half of our sample (10 SFGs) was drawn from the SINS and zC-SINF surveys of IFU spectroscopic data of z $\sim$ 1.5–2.5 SFGs, obtained using SINFONI on the Very Large Telescope (VLT) of the European Southern Observatory (ESO). For all of these objects, we obtained either K- and H-band (for z = 2–2.5) or H- and J-band (for z = 1.4) data in the seeing-limited mode of SINFONI. For a subset of these objects (six), we also obtained K-band data in the AO mode with the aid of either a natural or laser guide star. The seeing-limited data have a pixel scale of 0.125" $\times$ 0.25", whereas the AO data have a pixel scale of 0.05" $\times$ 0.1", with a spectral resolution of R = 1900, 2900 and 4500 (5000) for J, H and K-band (AO), respectively.

The full SINS and zC-SINF samples were selected as described in Förster Schreiber et al. (2009) and Mancini et al. (2011). Of the final 10 galaxies used in this analysis, two were selected based on their K-band magnitudes (Daddi et al. 2004b; Mignoli et al. 2005), three based on their K-band magnitudes and BzK colors (Kong et al. 2006; Lilly et al. 2007), and five from their U_nGR colors (Erb et al. 2003; Adelberger et al. 2004; Steidel et al. 2004; Erb et al. 2006b; Law et al. 2009).

We further selected galaxies to be observed in H- or J-band based on the requirement that they fall at a redshift such that all four emission lines of interest ([NII], Hα, [OIII], Hβ) are unaffected or weakly affected by OH sky lines. In addition, these targets are among the brighter objects in the SINS sample, enabling us to observe the relatively weak Hβ and [OIII] lines in comparatively short exposure times. For the present study, we included only galaxies that had a secure detection in all 4 emission lines with minimal interference from an OH sky line or had a secure detection in 3 lines and an upper limit for one of the lines, with the requirement that there was not an OH sky line near the upper limit, in order to ensure a meaningful value. Out of 15 galaxies for which we attempted to measure all four lines, only 10 were deemed acceptable based on the aforementioned criteria, and all have secure detections in all of the lines.

The resulting 10 targets present an exemplary sample of the galaxies in the SINS survey. They span the range in stellar mass from 0.77–31.6 $\times 10^{10}$ $M_{\odot}$, and star formation rate from 25 to 340 $M_{\odot}$/yr. They include various kinematic types: rotation and dispersion dominated objects as well as merging systems. For all the targets, the Hα and [NII] data had already been taken during previous SINFONI observing runs. We note that two of the SINS targets from our sample (Deep3a-15504 and K20-ID5) have evidence for an AGN from X-ray, UV, and/or mid-IR data (Förster Schreiber et al. 2009, 2013a).

Table 5.1 lists all observing runs during which the data of the 10 sources with secure Hα, [NII], [OIII], and Hβ detections were obtained (observing details for other sources with only Hα+[NII] data can be found in Förster Schreiber et al. (2009)). The table also gives the band/grating, pixel scale, observing mode, and the total on-source integration time. For simplicity '125' refers to the largest scale with nominal pixels of 0.125"$\times$0.250"and field of view of 8"x8", and '50' refers to the intermediate scale with nominal pixels of 0.05"$\times$0.125" and a field of view of 3.2"x3.2".

For the data reduction, we used the software package SPRED and custom routines for optimizing the background/OH airglow subtraction. The point spread function (PSF) full-width at half maximum (FWHM) was measured by fitting a 2D Gaussian profile to the combined images of the PSF calibration star taken throughout the observations of a galaxy. More information on the specifics of the data reduction can be found in Förster Schreiber et al. (2009), Mancini et al. (2011), and Förster Schreiber et al. (2013b).

5.2.2 Source selection, observations and data reduction of LUCI galaxies

We also include 12 galaxies observed with the LUCI1 NIR camera and spectrograph on the Large Binocular Telescope (LBT) (Ageorges et al. 2010; Seifert et al. 2010). LUCI1 allows multi-object spectroscopy with up to 23 laser-cut masks allowing arbitrarily placed and oriented slits having widths down to 0.1" within a 2.5' $\times$ 4' field (Buschkamp et al. 2010). These galaxies were observed in the H and K-bands for a median integration time of 4 hours each, employing 1"-wide slits. With this slit width and medium resolution gratings, the spectral resolution is 2850 in H band and 2900 or 1900 in K band. The observations were taken between December 2009 and May 2012, with seeing conditions ranging between 0.6" and 1.1". For further description of the LUCI1 instrument and the observations, see Buschkamp et al. (2010) and Kurk et al. (2013).

The majority of LUCI star-forming targets were selected from the GOODS-N field based on the PEP multiwavelength catalog (Berta et al. 2011) with spectroscopic redshifts from Barger et al. (2008). In addition, galaxies were selected from the Q2343 field (Steidel et al. 2004) based on the rest-UV selected sample presented in Erb et al. (2006b). Objects from both fields were selected based on their optical redshifts such that there was minimal overlap

Table 5.1: Observation Details for SINS/zC-SINF Targets

Object	**Band**	**Scale** [mas]	**Mode**	$\mathbf{t}_{int}$ [s]	**Observing Date(s)** [MonthYY]
Q1307-BM1163	J	125	seeing-limited	7200	Mar05
	H	125	seeing-limited	14400	Mar05
Q2343-BX389	H	125	seeing-limited	15900	Jun06, Aug06
	K	125	seeing-limited	14400	Oct05
	K	50	LGS-AO	18000	Sep12, Oct12
Q2343-BX610[a]	H	125	seeing-limited	30000	Oct05, Nov07
	K	125	seeing-limited	10800	Jun05, Aug05
	K	50	LGS-AO	30000	Sep11, Oct11, Aug12
Deep3a-6004[a]	H	125	seeing-limited	13200	Feb10, Mar10
	K	125	seeing-limited	36000	Mar06, Mar07
	K	50	LGS-AO	19200	Jan10, Mar10, Jan11, Mar11, Mar12, Apr13
Deep3a-15504[b]	H	125	seeing-limited	14400	Apr06
	K	125	seeing-limited	21600	Mar06
	K	50	LGS-AO	82800	Mar06–Apr11
ZC-407302	H	125	seeing-limited	20400	Dec09, Jan10
	K	125	seeing-limited	7200	Mar07
	K	50	LGS-AO	68400	Apr07, Apr09, Mar12
K20-ID5[b]	H	125	seeing-limited	7200	Mar05
	K	125	seeing-limited	9600	Mar05
K20-ID7	H	125	seeing-limited	24000	Jan10, Feb10
	K	125	seeing-limited	31200	Oct05, Nov06
SSA22a-MD41	H	125	seeing-limited	3600	Aug06
	K	125	seeing-limited	25200	Nov04, Jun05
Q1623-BX599	H	125	seeing-limited	12000	Apr11, Jul11
	K	125	seeing-limited	5400	Jul04
	K	50	AO	7200	Apr10

[a] Has evidence for an AGN based only on spatially resolved line ratios.
[b] Has evidence for an AGN from X-ray, UV, and/or mid-IR data.

of the Hα, [NII], [OIII], and Hβ emission lines with OH sky features.

The data were reduced using a custom pipeline developed at MPE (Kurk et al. 2013). The pipeline includes cosmic ray removal, correction for distortion and the same routine to remove OH sky features as used for the SINFONI reduction (Davies 2007). The background is subtracted from frames in pairs obtained from on-slit dithering. Wavelength calibration was conducted using OH sky lines, and flux calibration using a Telluric standard star. The noise spectrum was determined using the same method as for the SINFONI data (Förster Schreiber et al. 2009).

5.2.3 Galaxy Properties for the Total sample

Our total sample of 22 galaxies contains 10 SFGs from the SINS/zC-SINF survey with all four emission lines detected, 6 galaxies from the LUCI survey with all four lines detected and 6 galaxies from the LUCI survey with an upper limit for either the [NII] or [OIII] emission line and secure detections for the remaining three lines. These galaxies sample the z $\sim$ 1.5–2.5 'main sequence' of SFGs in the stellar mass/star-formation rate plane between stellar masses of 1×10^9 and 3×10^{11} $M_\odot$ and SFRs between 6 and 340 $M_\odot$/yr (Figure 5.1).

For the SINS/zC-SINF galaxies, stellar masses and star-formation rates were determined from stellar population synthesis modeling of broad-band photometry in Förster Schreiber et al. (2009), Mancini et al. (2011), and Förster Schreiber et al. (2011a), and assume either a constant star-formation history or an exponentially declining model with Bruzual & Charlot (2003) stellar evolution tracks, a Chabrier (2003) IMF and a Calzetti et al. (2000) dust law. For Q1307-BM1163, photometry is only available in three optical bands, preventing reliable SED modeling to derive the stellar properties. Galaxy properties for the LUCI sample were derived by Wuyts et al. (2011a) based on broad-band SEDs. Stellar masses and star-formation rates are computed with the FAST routine (Kriek et al. 2009) using Bruzual & Charlot (2003) stellar evolution models with exponentially declining star-formation histories. These galaxy properties are listed in Table 5.2.

5.2.4 Extraction of Emission Line Fluxes and Maps

We extracted source- and region-integrated emission line fluxes as well as emission line maps from the final SINFONI science data cubes using line profile fitting. Prior to fitting, we apply a 3 pixel wide median filter to the data cubes to increase the signal-to-noise ratio (SNR). We then use the Gaussian fitting routine LINEFIT (Davies et al. 2011) to produce Hα emission line flux, velocity and velocity dispersion maps. Using these Hα kinematic maps, we velocity-shifted all of the data cubes for each object such that the Hα line falls at the same wavelength for each pixel in order to remove the line-broadening effect of large scale velocity gradients. We then summed the spectra of individual pixels from the velocity-shifted cubes to obtain co-added spectra. For those galaxies that have high enough SNR data to create kinematic maps for [OIII] in addition to Hα, we find that the kinematics of these lines are roughly consistent, such that we are justified in using the kinematic maps of Hα to correct

Table 5.2: Galaxy properties for the total sample

Object	**SFR** $M_\odot$ yr^{-1}	**sSFR** Gyr^{-1}	$\mathbf{M_*}$ 10^{11} $M_\odot$
Q1307-BM1163[a]	57	—	—
Q2343-BX389	25	0.61	0.41
Q2343-BX610[b]	60	0.60	1.01
Deep3a-6004[b]	214	0.68	3.26
Deep3a-15504[c]	150	1.38	1.08
ZC-407302	340	13.93	0.241
K20-ID5[c]	310	10.11	1.40
K20-ID7	112	2.84	0.40
SSA22a-MD41	185	24.03	0.077
Q1623-BX599	34	0.60	0.571
GN-7573	8	0.22	0.339
GN-21496	9	0.22	0.417
GN-16564	7	5.08	0.013
GN-31720	35	0.74	0.479
GN-4126	23	0.60	0.380
Q2343-BX442	42	0.34	1.230
GN-2602	63	1.48	0.427
GN-3493	51	0.76	0.676
GN-4104	8	1.45	0.056
GN-28625	17	1.20	0.138
GN-12976	6	2.57	0.023
Q2343-BX436	54	11.75	0.046

[a] This galaxy does not have reliable photometry, and the SFR is thus derived from $H\alpha$.
[b] Has evidence for an AGN based only on spatially resolved line ratios.
[c] Has evidence for an AGN from X-ray, UV, and/or mid-IR data.

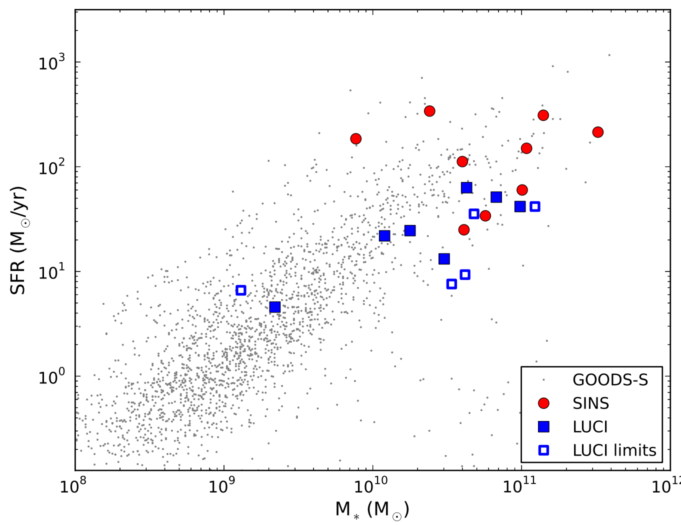

Figure 5.1: The location of our sample on the SFR-M_* plane. GOODS-S galaxies from z=1.4–3 are shown as gray points (see: Wuyts et al. 2012), red circles are SINS galaxies and blue squares are LUCI galaxies. For the LUCI galaxies, we show objects that have secure detections in all four emission lines with closed symbols and those that have an upper limit in one as open symbols.

for all of the data cubes. We note that the emission line ratios do not vary significantly without this velocity shifting, but this technique allows us to recover additional flux, which is especially important for some of the fainter lines.

We obtain fluxes for each emission line by simultaneously fitting a constant continuum offset and the Hα, [NII]λ6548,6584, and [SII]λ6717,6731 lines of the co-added spectra assuming identical kinematics (velocity and line width). We then fit the [OIII]λ4959,5007 and Hβ lines assuming the same kinematics as for Hα. For all lines, we assume a Gaussian shape. The errors for the line fluxes are generated from the fit uncertainties, using the noise cube produced from the reduction as input. These errors are on average greater than those obtained from 1000 Monte Carlo simulations.

In order to compare region-integrated spectra or emission line maps (for pixel-to-pixel analysis) that were derived from different bands, we used the 250mas data cube for both even when a 100mas cube was available, for resolution consistency. However, we note that for the integrated spectra, we used the higher quality (from longer t_{int}) 100mas cubes when available. For comparing emission lines from different data cubes, we register the position of the galaxy in each cube using the centroid of the continuum emission, if possible. If there is not a clear continuum signature free from residuals, we use the centroid of the Hα and [OIII] emission line fluxes, checking that the morphology and peak of emission is similar for these lines. We also find that the point spread functions (PSFs) for different bands are consistent within 30%, which is the combined uncertainty of the resolution of the data sets. For the pixel-to-pixel analysis, we only consider pixels with a SNR of the line flux >3 for all four emission lines.

For the LUCI targets, we collapsed the 2D data onto a 1D spectrum with an aperture chosen to optimize the SNR. We have attempted a similar velocity-shifting technique as for the SINFONI data, but for the few objects for which this was possible, the procedure only increased contamination from OH features. Thus we have not used any velocity-shifted LUCI spectra, but note that as mentioned before, this should not have a large affect on the emission line ratios.

The emission line fluxes for the LUCI spectra were fit using the LINEFIT routine, with errors derived from 100 Monte Carlo simulations. For lines that were undetected, a 3σ upper limit was derived based on the noise spectrum for the wavelengths corresponding to the line of interest based on the Hα-derived redshift, assuming the same line width as Hα. For two of the galaxies from the LUCI sample (GN2602, GN3493), the [OIII]λ5007 line was out of the range of the filter and thus the [OIII] upper limit was determined from the [OIII]λ4959 emission line and adopting the approximate scaling [OIII]$\lambda5007 = 3 \times$ [OIII]λ4959. In another one of our objects (GN4126) the [OIII] and Hβ fluxes are derived from an HST/WFC3 Grism spectrum (B. Weiner, private communication), because neither of these lines were detected in our LUCI data. These fluxes are determined using the same method as for the SINFONI spectra, except the line positions and widths were allowed to differ from those of Hα since the GRISM line width is more sensitive to the object size than kinematics (because the GRISM spectra are slit-less and very low resolution). Table 5.3 lists the [NII]λ6584/Hα and [OIII]λ5007/Hβ line ratios and the inferred abundances based on the N2 and O3N2 calibrations from Pettini & Pagel (2004) for our sources.

Galaxy-averaged spectra are shown for the SINS galaxies in Figures 5.2 and 5.3 and for the LUCI galaxies in Figures 5.4 and 5.5 (the latter of which contains galaxies with an upper limit for one of the lines).

5.3 Results

5.3.1 Excitation Properties of $z \sim 2$ Galaxies

Galaxy-integrated measurements

We show the galaxy-integrated line ratios in the BPT diagram in Figure 5.6. Many of the objects in our sample are located in the 'composite' region of the BPT diagram, between the star-forming and AGN branches traced out by the local SDSS galaxies, and demarcated by the Kauffmann et al. (2003) and Kewley et al. (2001b) empirical and theoretical divisions between star-forming and AGN galaxies. This is consistent with most findings of other recent work for samples of galaxies selected by similar criteria (Erb et al. 2006a; Shapley et al. 2005; Liu et al. 2008; Kriek et al. 2007; Hayashi et al. 2009; Yabe et al. 2012; Trump et al. 2013, see Figure 5.7). The observed offset of high-z galaxies from the local star-forming branch suggests that different physical conditions and/or chemical abundances prevail in the high-z

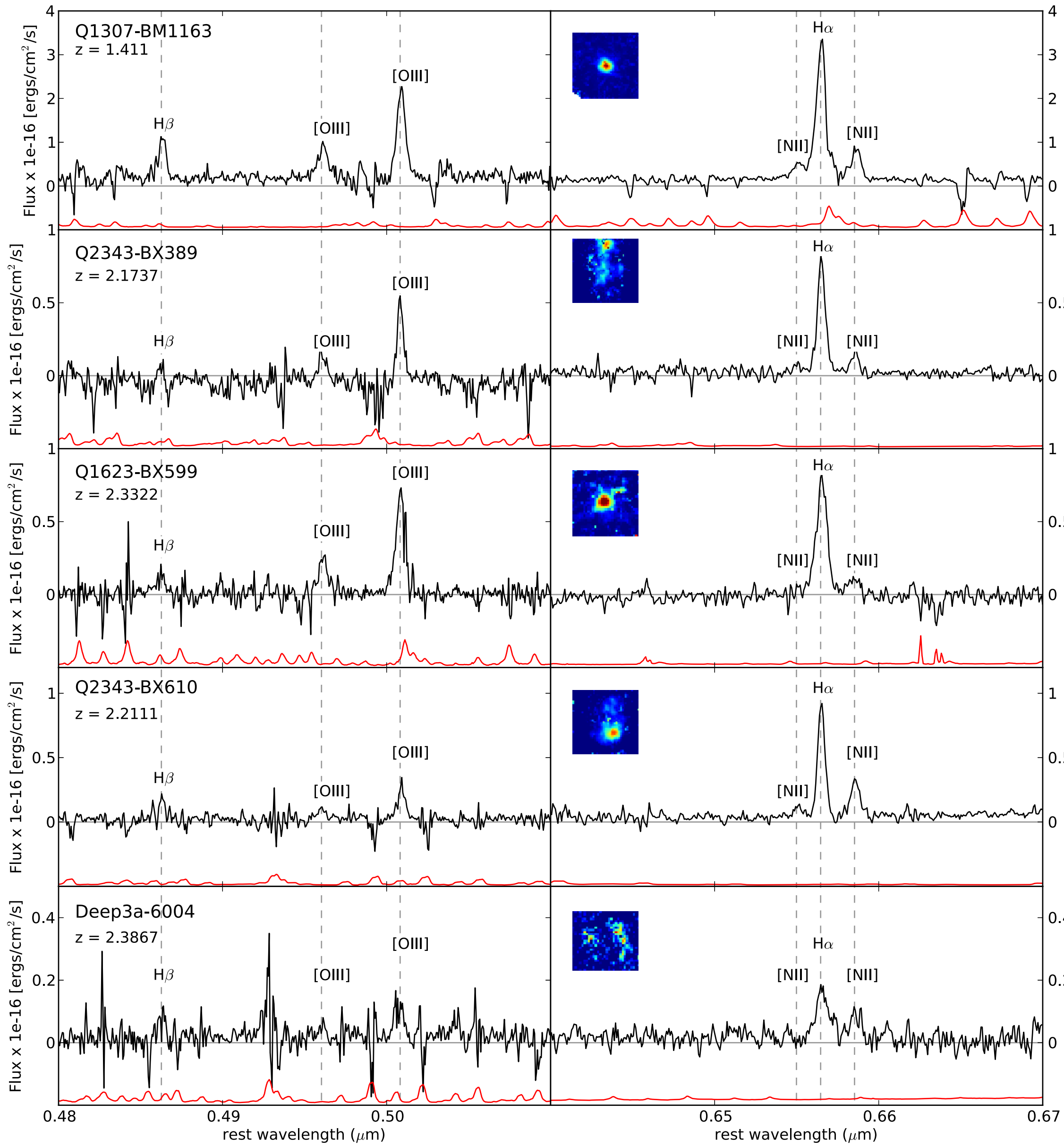

Figure 5.2: Galaxy spectra for five of the SINS/zC-SINF objects. The black lines show the data and the red lines show the error derived from the noise cubes. The inset in the right panels shows an AO-scale (if available) Hα image of the galaxy.

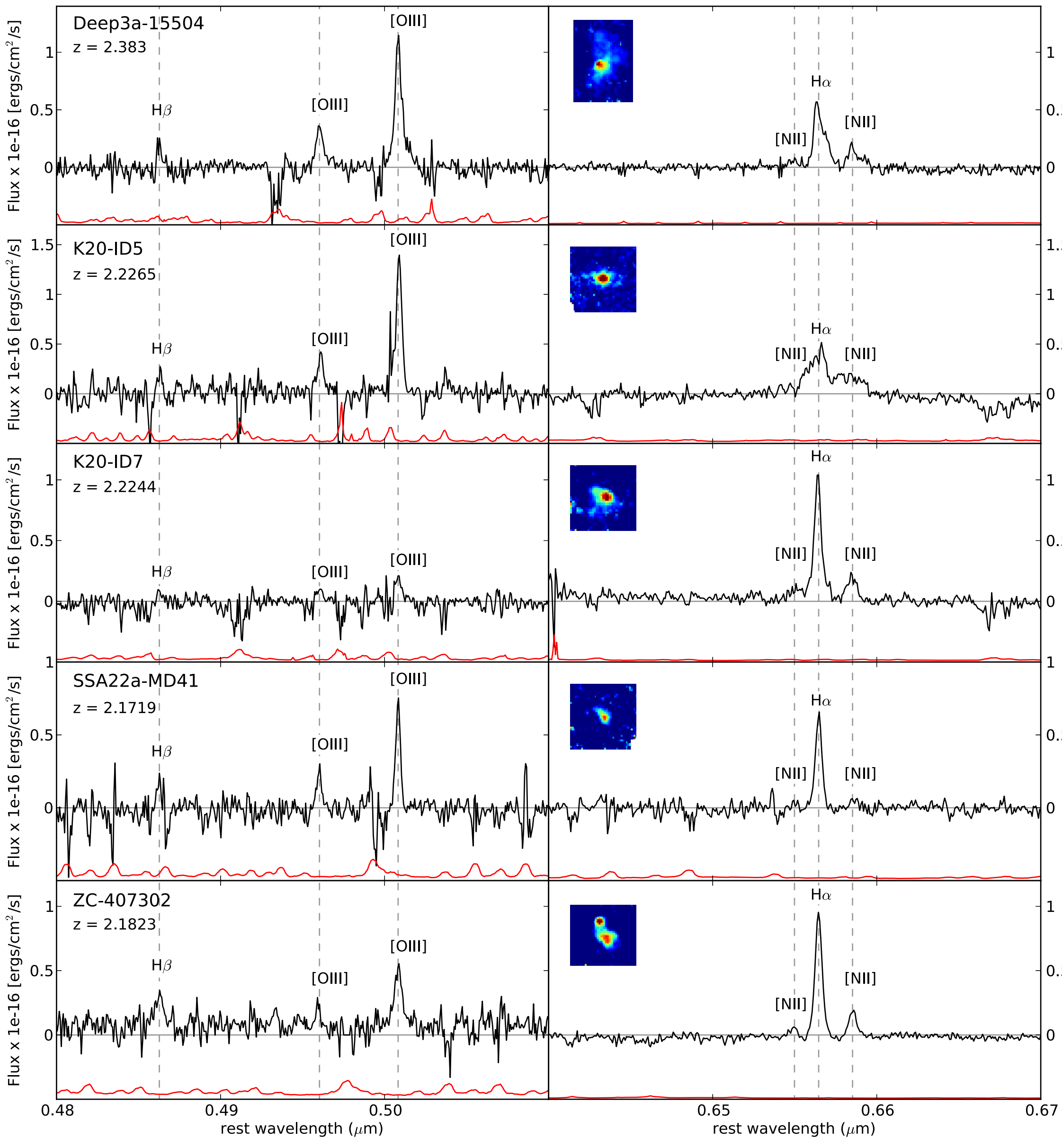

Figure 5.3: Same as for Figure 5.2

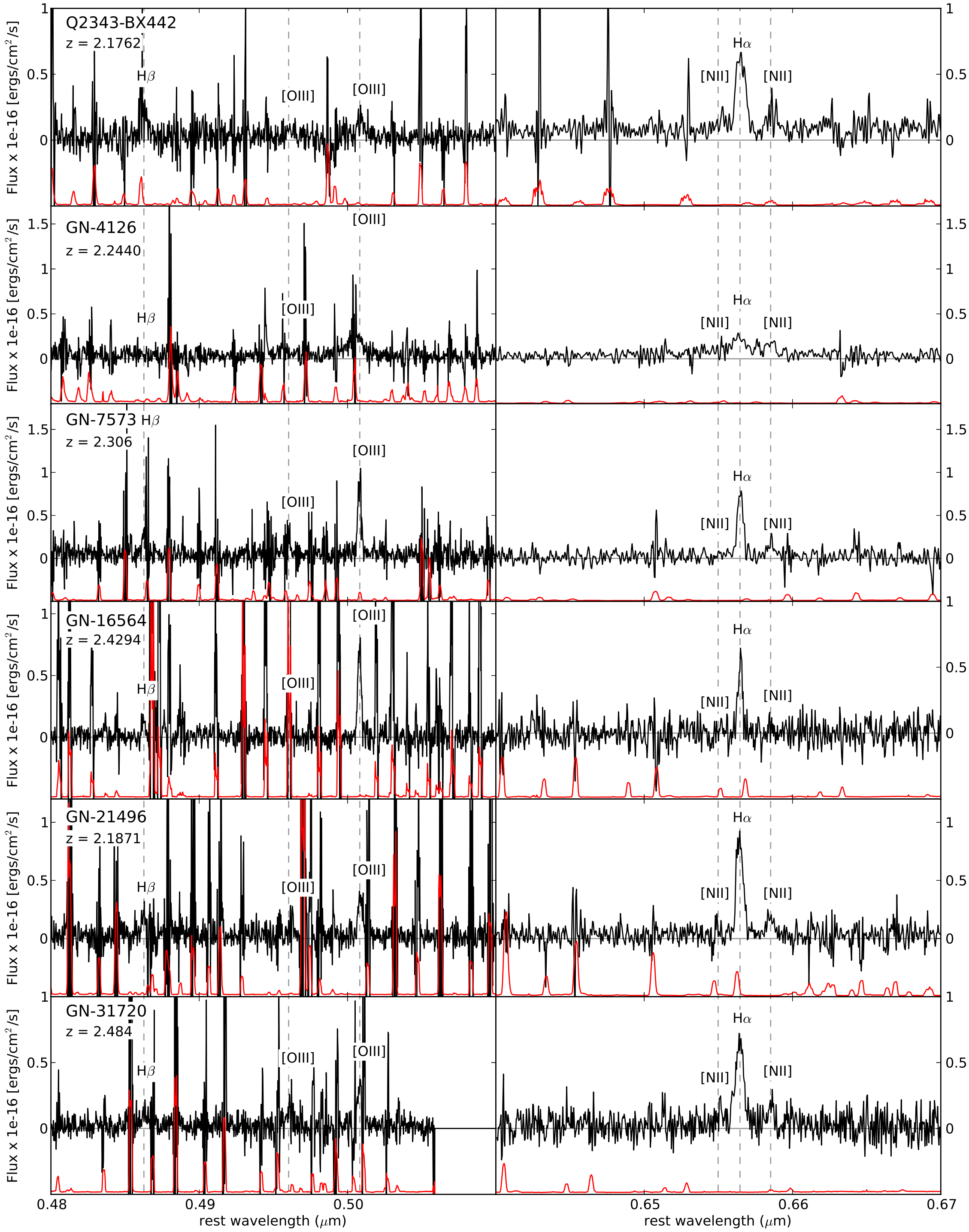

Figure 5.4: Galaxy spectra of LUCI galaxies with detections in all four lines. The error spectrum (red line) is shown as a factor of 5 lower than its actual value.

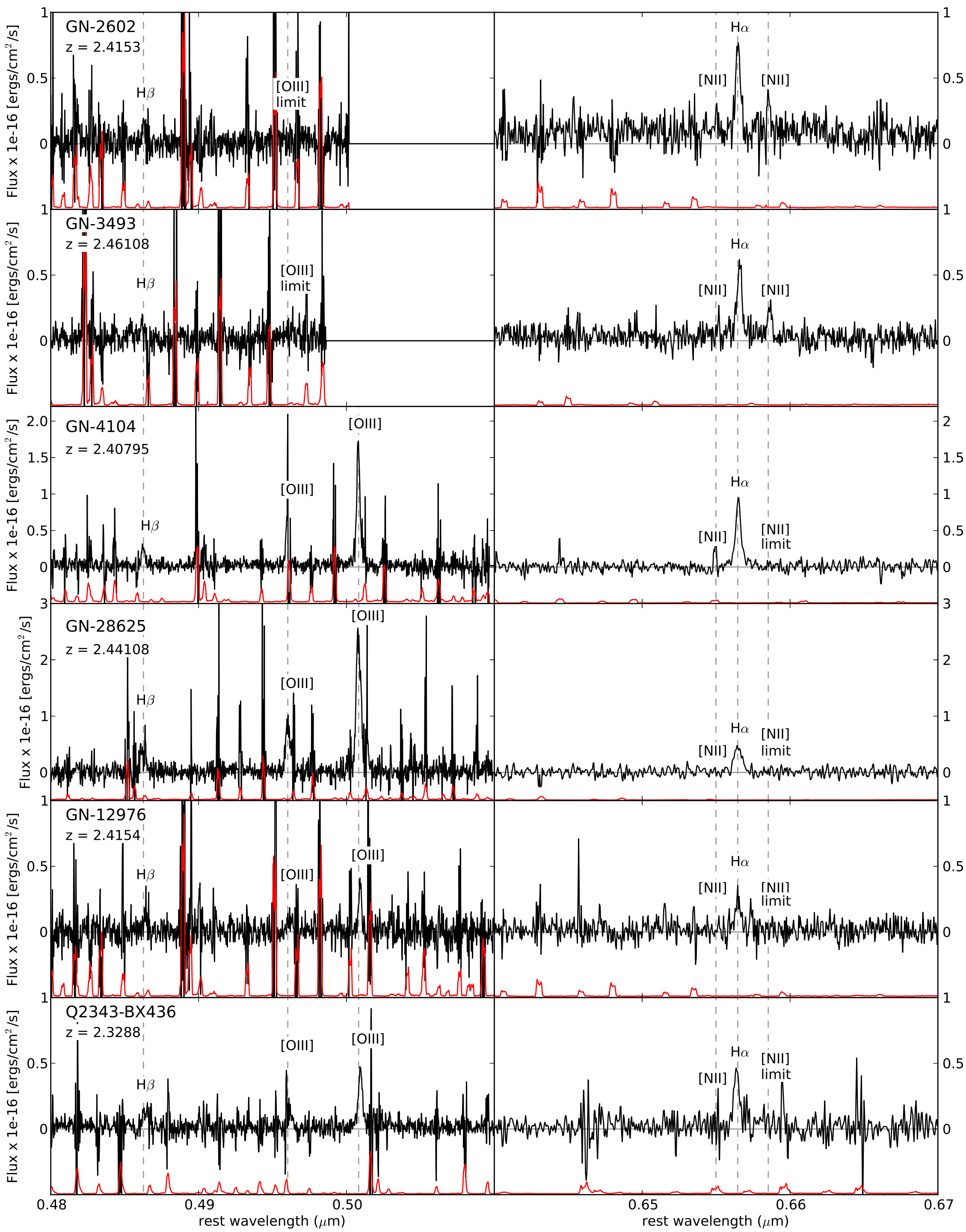

Figure 5.5: Galaxy spectra of LUCI galaxies with detections in three lines and an upper limit in the remaining line. For GN-2602 and GN-3493, the [OIII]λ5007 line flux was derived from 3 × the [OIII]λ4959 line flux. The error spectrum (red line) is shown as a factor of 5 lower than its actual value.

Table 5.3: Emission Line Ratios

Object	**[NII]/Hα**	**[OIII]λ5007/Hβ**	**Z/Z$_\odot$ (N2)[a]**	**Z/Z$_\odot$ (O3N2)[a]**
Q1307-BM1163	0.256 ± 0.024	2.29 ± 0.16	0.75	0.45
Q2343-BX389	0.180 ± 0.027	7.04 ± 1.91	0.61	0.34
Q2343-BX610[b]	0.339 ± 0.029	1.69 ± 0.22	0.88	0.66
Deep3a-6004[b]	0.419 ± 0.227	1.62 ± 0.30	0.99	0.71
Deep3a-15504[c]	0.350 ± 0.089	8.13 ± 2.00	0.89	0.40
ZC-407302	0.223 ± 0.015	1.80 ± 0.18	0.69	0.56
K20-ID5[c]	0.560 ± 0.102	7.00 ± 0.78	1.17	0.49
K20-ID7	0.236 ± 0.042	2.76 ± 0.58	0.71	0.50
SSA22a-MD41	0.100 ± 0.038	4.09 ± 0.71	0.44	0.33
Q1623-BX599	0.167 ± 0.030	6.48 ± 1.33	0.58	0.34
GN-7573	0.247 ± 0.040	4.17 ± 0.69	0.73	0.44
GN-21496	0.204 ± 0.034	2.53 ± 0.70	0.66	0.49
GN-16564	0.067 ± 0.055	7.13 ± 2.184	0.35	0.25
GN-31720	0.162 ± 0.060	2.97 ± 0.86	0.58	0.43
GN-4126	0.626 ± 0.047	7.10 ± 2.28	1.24	0.50
Q2343-BX442	0.232 ± 0.076	0.56 ± 0.10	0.71	0.83
GN-2602	0.402 ± 0.066	>1.573 ± 0.72	0.96	0.71
GN-3493	0.143 ± 0.043	>1.028 ± 0.79	0.54	0.58
GN-4104	<0.109 ± 0.109	6.92 ± 0.65	0.46	0.29
GN-28625	<0.119 ± 0.119	6.30 ± 1.04	0.48	0.31
GN-12976	<0.306 ± 0.208	5.76 ± 3.50	0.83	0.43
Q2343-BX436	<0.151 ± 0.151	4.73 ± 0.65	0.55	0.36

[a] Assuming Z$_\odot$ = 8.69 (Asplund et al. 2009) and using the calibration of Pettini & Pagel (2004).
[b] Has evidence for an AGN based only on spatially resolved line ratios.
[c] Has evidence for an AGN from X-ray, UV, and/or mid-IR data.

non-AGN actively star-forming systems compared to the bulk of local star-forming galaxies (see, e.g., the detailed discussion by Liu et al. 2008). We note that all of the galaxies that are identified as AGN either from X-ray, UV or mid-IR data or based on spatially-resolved rest-frame optical data (see next section and Förster Schreiber et al. 2013a), have [NII]/H$\alpha \gtrsim 0.3$ independent of whether they are located in the composite or AGN region of the diagram. However, all galaxies in the composite region are not necessarily AGN. We also compare our observations with the new theoretical model of Kewley et al. (2013), wherein a redshift-dependent dividing line between star-forming and AGN galaxies is introduced. At $z \sim 2.2$ where most of our galaxies live, the dividing line is very similar to the Kewley et al. (2001b) division, and thus Q2343-BX610 and Deep3a-6004, which we later show to have evidence for AGN from spatially-resolved data, would not be characterized as AGN galaxies. We further examine the galaxies that fall near the composite region and how to identify galaxies with obscured AGN using spatially resolved data in the next section.

To explore some of the trends described in Liu et al. (2008) and Brinchmann et al. (2008), we color-code galaxies in the BPT diagram by SFR, stellar mass and sSFR (Figure 5.8). We include all of our SINS and LUCI galaxies as well as galaxies from the literature, presented in Figure 5.7, with secure detections in all four emission lines. Thus this analysis includes galaxies from z=1 to 2.5. As expected from the mass-metallicity relation, there is a trend of increasing stellar mass with higher [NII]/Hα ratios. We also find a trend of increasing offset (mostly in the [NII]/Hα direction) from the HII branch with increasing SFR, which may be correlated with an increase in ionization parameter, but may also be due to the aforementioned stellar mass trend since stellar mass and star formation rate are tightly correlated for SFGs (Daddi et al. 2007; Rodighiero et al. 2011). Finally, there may be a (marginal) trend of increasing [OIII]/Hβ ratio with increasing sSFR, suggesting that galaxies in the 'composite' region of the BPT diagram may be in a burstier phase of star-formation than those that lie on the HII branch. This is consistent with the finding that many of the local galaxies in the 'composite' region are starbursts (Liu et al. 2008; Brinchmann et al. 2008). Alternatively, the elevated sSFR for these galaxies could be related to AGN activity affecting the line ratio, if there is a correlation between sSFR and AGN activity. However, Rangel et al. (2013) suggest that there is no such correlation.

The measured Hβ fluxes might also be biased by underlying stellar Hβ absorption (Dufour et al. 1980). We therefore correct for this absorption using the best fit SED-derived star-formation histories and ages. Once we account for this correction factor, we see a noticeable down-shift in [OIII]/Hβ of ~ 0.02 to 0.21 dex (mean 0.08 dex). Nevertheless, accounting for Hβ absorption does not reconcile our data with the distribution of local galaxies from the SDSS (Figure 5.9) and therefore does not affect our qualitative conclusions. Our estimated corrections for Hβ absorption are fairly similar to those of Shapley et al. (2005) who reported a maximum down-shift of 0.1 dex and also found that unaccounted-for Hβ absorption is likely not causing the observed offset in [OIII]/Hβ for their DEEP2 sample. For the remainder of this paper, we use emission line ratios that are not corrected for stellar Hβ absorption for consistency with previous work.

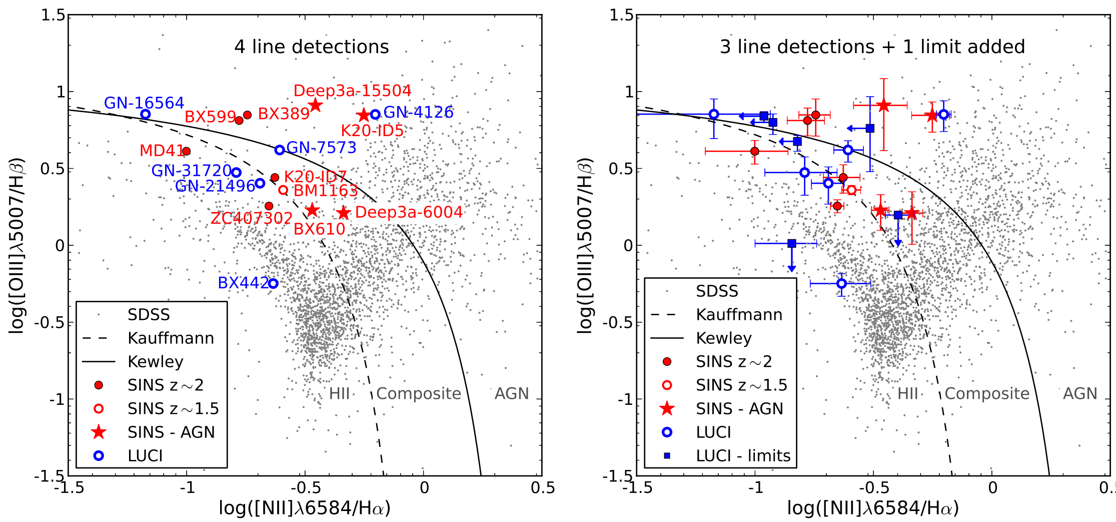

Figure 5.6: The [NII]/Hα vs. [OIII]/Hβ plane (BPT diagram). SINS galaxies are shown as either red circles (star-forming) or red stars (those identified as AGN), and LUCI galaxies are shown as blue circles, with galaxies that have only three line detections and one upper limit shown in the right panel as blue filled squares.

Spatially-resolved measurements

In this section, we exploit the high-quality IFU data taken of the SINS/zC-SINF galaxies in our sample. Overall, the emission line and kinematic maps of our targets for the different emission lines are in good agreement. For most sources, the main emission peak in all of the individual line maps is found at the same location inside the source boundaries. Some notable exceptions exist for a couple of sources (K20-ID5 and ZC407302, see discussion later in this section), where, in particular, the peak [OIII] emission was somewhat offset from the Hα peak emission. For four of the galaxies in our SINS/zC-SINF sample, the SNR is sufficiently high in all four lines ([NII], Hα, [OIII], Hβ) that we are able to plot individual pixels in the BPT diagram for a large region of these galaxies. For the remaining galaxies (except Deep3a-6004), we are still able to obtain high quality spectra of the inner (R <0.4") and outer regions (see Figure 5.10), where the center is determined as in Section 5.2.

We find that many galaxies have inner regions that are offset to higher excitation relative to their outer regions, indicating that perhaps the inner region is influenced by an (possibly obscured) AGN and the outer region is dominated by star-formation (see Figure 5.10). Alternatively, the inner region could have a larger contribution from shock excitation or elevated ionization parameter, perhaps due to an outflow, as seen in the star-forming clumps of a $z \sim 2$ SFG presented in Newman et al. (2012a). This inner/outer region offset is seen for two galaxies with strong evidence for an AGN, Deep3a-15504 and K20-ID5, as well as Q2343-BX389, which has no other evidence for an AGN (see discussion below). However,

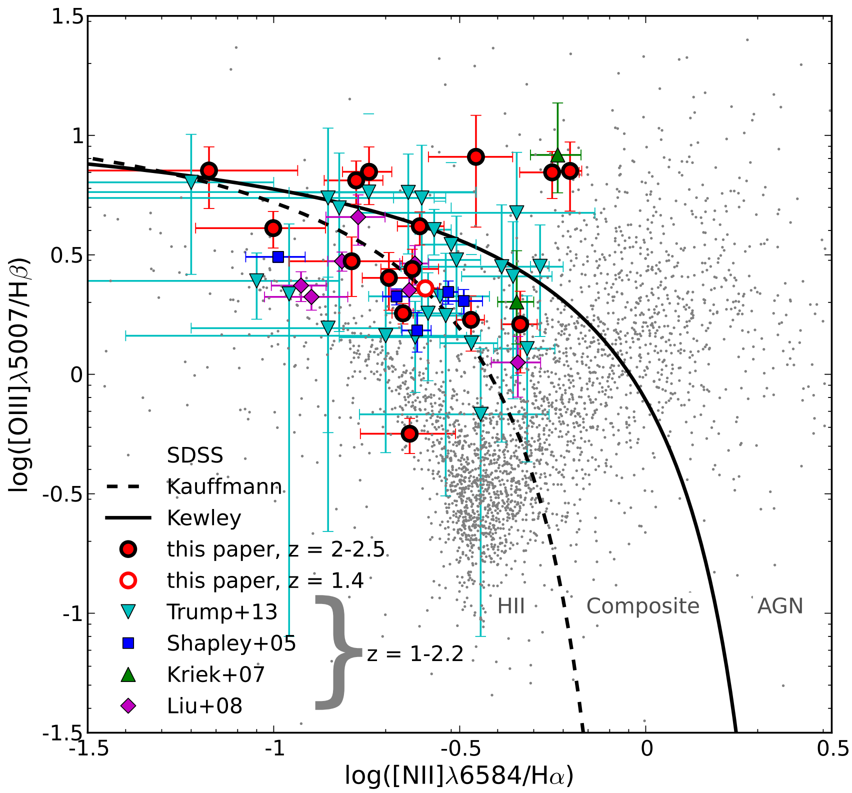

Figure 5.7: The [NII]/Hα vs. [OIII]/Hβ plane (BPT diagram). SINS and LUCI galaxies are shown as red circles, and data from Shapley et al. (2005), Kriek et al. (2007), Liu et al. (2008) and Trump et al. (2013) are blue squares, green upright triangles, magenta diamonds and cyan inverted triangles, respectively. Only secure detections in all four lines (not upper limits) are shown.

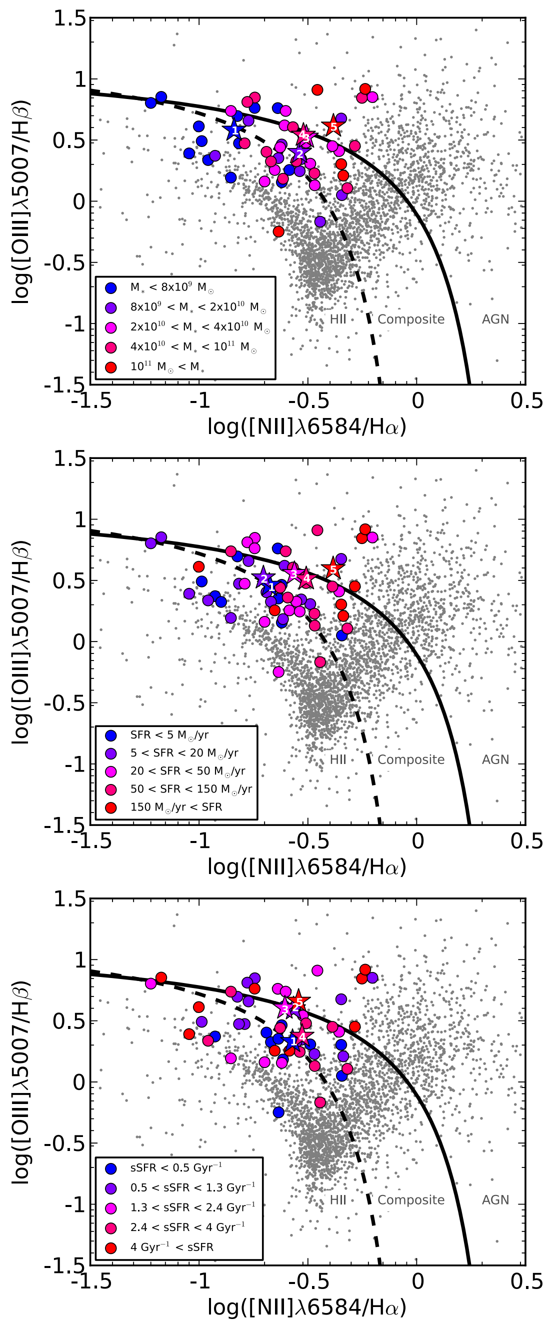

Figure 5.8: BPT diagram with SINS, LUCI and literature data color-coded by M_*(top panel), SFR (middle panel) and sSFR (lower panel). Individual galaxies are shown as circles and the average of each bin is shown as a star with a number representing the order of the bin. Both M_* and SFR appear to increase with increasing [NII]/Hα, while there is perhaps a marginal trend of increasing sSFR with increasing [OIII]/Hβ.

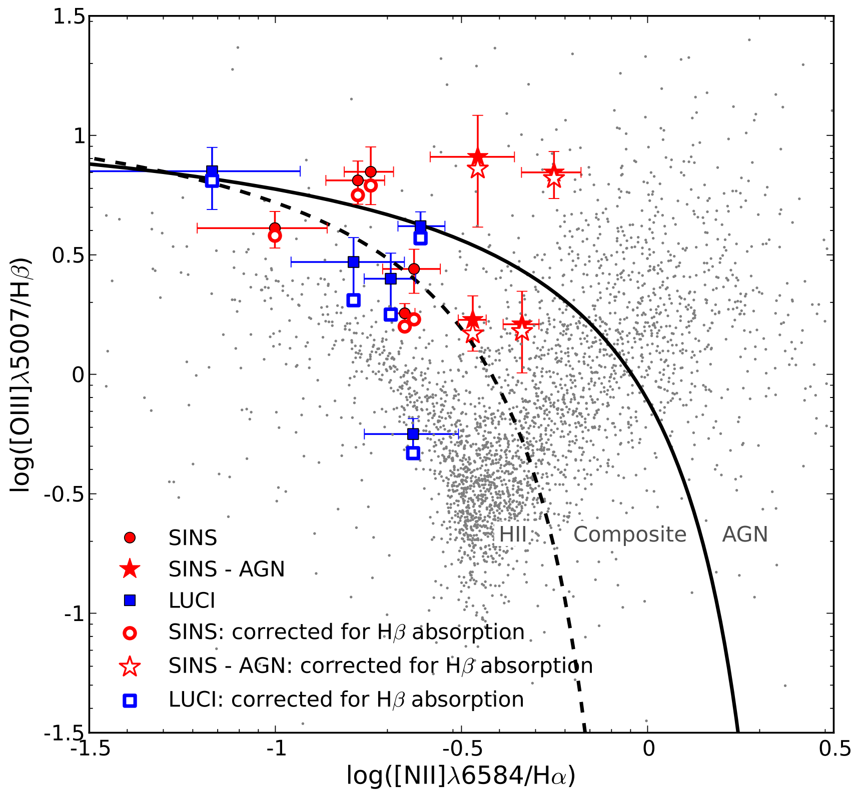

Figure 5.9: BPT diagram with SINS and LUCI data before (closed symbols) and after (open symbols) correction for stellar $H\beta$ absorption. The correction is marginal, with a mean offset of 0.08dex, and cannot fully account for the elevated line ratios of $z \sim 2$ SFGs as compared with local SFGs.

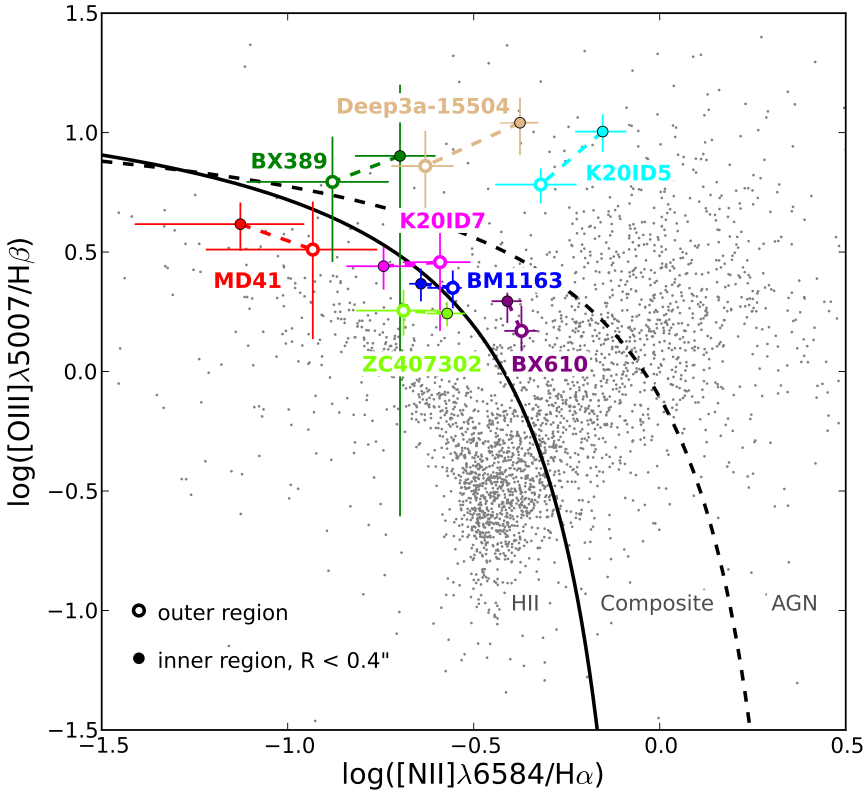

Figure 5.10: BPT diagram showing inner and outer regions for each galaxy. The inner regions (with R < 0.4") are shown as closed symbols and the outer regions as open symbols. Several objects, particularly those in the AGN regime of the diagram, show elevated line ratios in their inner regions with respect to their outer regions.

we note that the Hβ line for Q2343-BX389 becomes somewhat contaminated by an OH sky line on it's redshifted side, and thus its outer spectrum may be unreliable, as reflected in the error bars. For the remaining galaxies, the offsets between the inner and outer regions in the BPT diagram are consistent with the 1σ errors.

Figures 5.11, 5.12, 5.13 and 5.14 show pixel-by-pixel BPT diagrams for Deep3a-15504, ZC407302, Q1623-BX599 and Q2343-BX610 along with [NII]/Hα and [OIII]/Hβ maps with a SNR cut-off of 3. There are some small discrepancies between Figure 5.10 and Figures 5.11 through 5.14, and these stem from the different techniques used to extract the line ratios in the pixel-by-pixel and inner/outer region analysis and the resulting flux weightings (i.e. fitting the lines to individual pixel spectra versus to integrated spectra).

Deep3a-15504

Deep3a-15504 is a large, rotating massive disk which has previously been identified as an AGN based on broad and/or high excitation lines in the optical (rest-UV) spectrum (Kong et al. 2006; Genzel et al. 2006, E. Daddi, private communication). In addition to elevated [NII]/Hα values, its nuclear region also demonstrates extremely broad Hα emission line wings, with velocities of up to 1500 km s^{-1}(Genzel et al. 2006; Förster Schreiber et al. 2013a). The deep, AO-assisted Hα map obtained for this galaxy shows that the star formation activity in the large disk takes place in several moderately bright clumps superimposed on diffuse emission. With pixel-by-pixel analysis (see Fig. 5.11), the central AGN-dominated (red and green symbols) and outer star-forming disk regions (blue pixels) separate clearly. While the outer region pixels still lie between the AGN region and the composite region of the BPT diagram, it is clear that the high excitation due to the AGN at the center drives the integrated ratios to values even closer to those of the AGN regime.

ZC407302

ZC407302 has no evidence for an AGN either from resolved Hα observations or ancillary data. This is corroborated by the pixel-by-pixel BPT diagram (Figure 5.12), where all pixels are consistent with excitation as observed in purely star-forming objects, and are very similar to the integrated line ratio. This is also reflected in the fairly uniform line ratio maps from the seeing-limited SINFONI data. As mentioned earlier in this section, there is a slight discrepancy between the peaks of Hα and [OIII] emission. This could be due to the asymmetric light distribution in Hα and [NII] seen in the high resolution AO map (see Figure 5.3, Genzel et al. 2008, 2011). The asymmetry is mainly caused by a compact source north-east of the main body of the galaxy, which is not resolved in the seeing-limited maps of Figure 5.12 but is present in the adaptive optics data set as well as in ACS i-band and HST WFC3 J- and H-band imaging available for this galaxy (S. Tacchella *et al.* in preparation). This source could be a bright disk clump at the edge of the system or a second, lower mass galaxy interacting with the main galaxy. The overall velocity field is consistent with a large disk galaxy, while on kpc-scales, deviations from pure rotation are visible and the north-eastern part appears more disturbed (Genzel et al. 2011).

Q1623-BX599

Q1623-BX599 is a compact, rotating disk (Newman et al. 2013). Like ZC407302, it has no evidence for an AGN and all three regions appear to lie in or close to the star-forming region of the BPT diagram (Figure 5.13). However, this galaxy does barely lie in the AGN regime of the BPT diagram based on integrated line ratios (Figure 5.6). This may be due to the fact that much of the east half of the galaxy has very low SNR in Hβ (see [OIII]/Hβmap in Figure 5.13) and the inclusion of this region in the integrated spectrum is driving up the [OIII]/Hβ ratio. Based on the low [NII]/Hα ratio for this galaxy (0.17 $\pm$ 0.03), and the results of the pixel-by-pixel analysis, it is unlikely that this galaxy harbors an AGN.

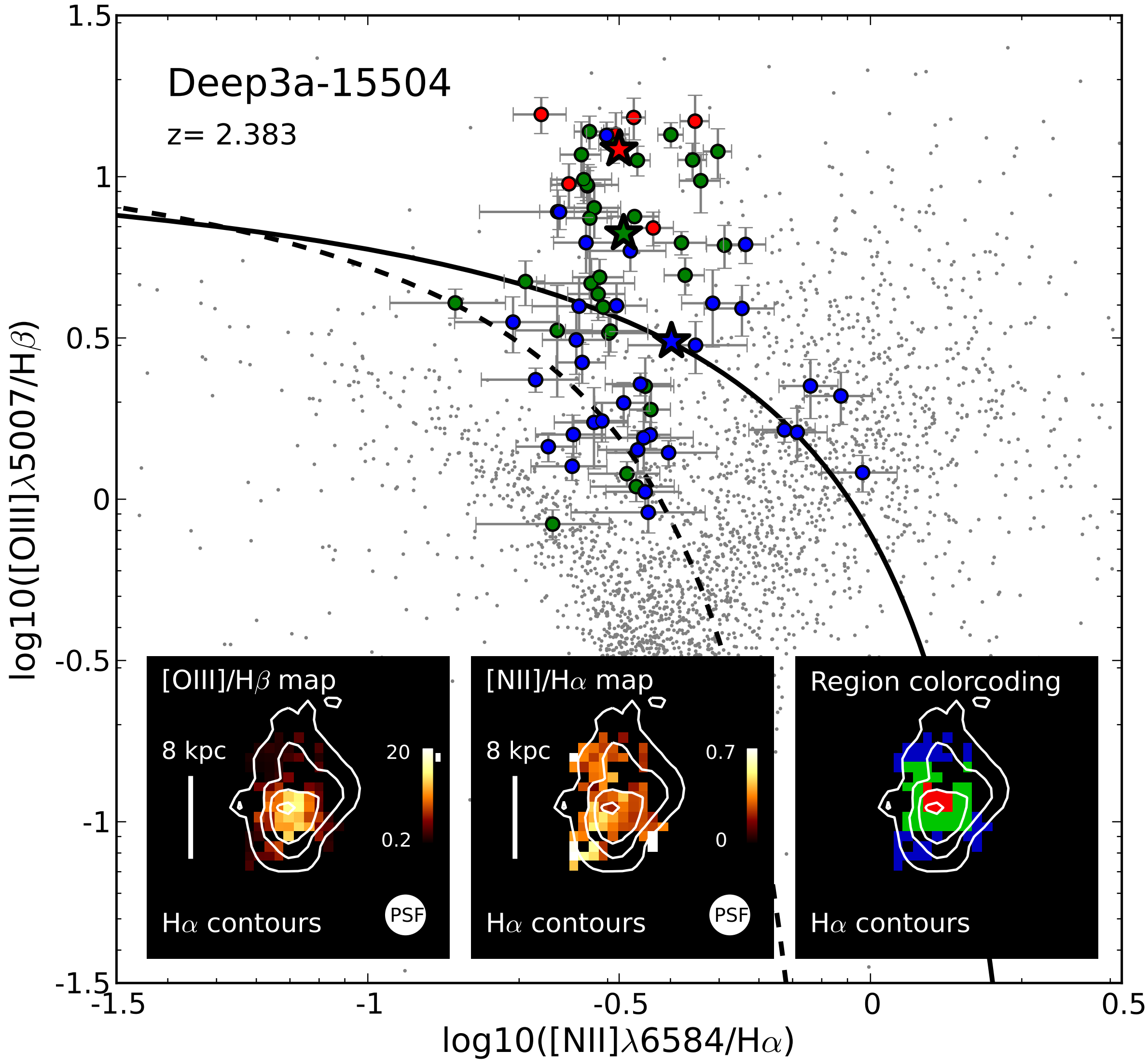

Figure 5.11: Pixel-by-pixel BPT diagram for Deep3a-15504. Red points are from the innermost region, green points from further out and blue points from the furthest edges of the galaxy. The region-averaged data are shown as star symbols. The rightmost inset shows the color-coding for the regions, the middle inset shows a map of [NII]/Hα, and the left inset shows [OIII]/Hβ. Hα contours appear on all three maps, and only pixels are shown with SNR > 3 in all four lines. The emission line maps show higher ratios in the nuclear regions, particularly for [OIII]/Hβ and this is reflected in the BPT diagram. Thus the outer region is influenced by star-formation in the disk, while the nuclear region is mostly a reflection of the AGN.

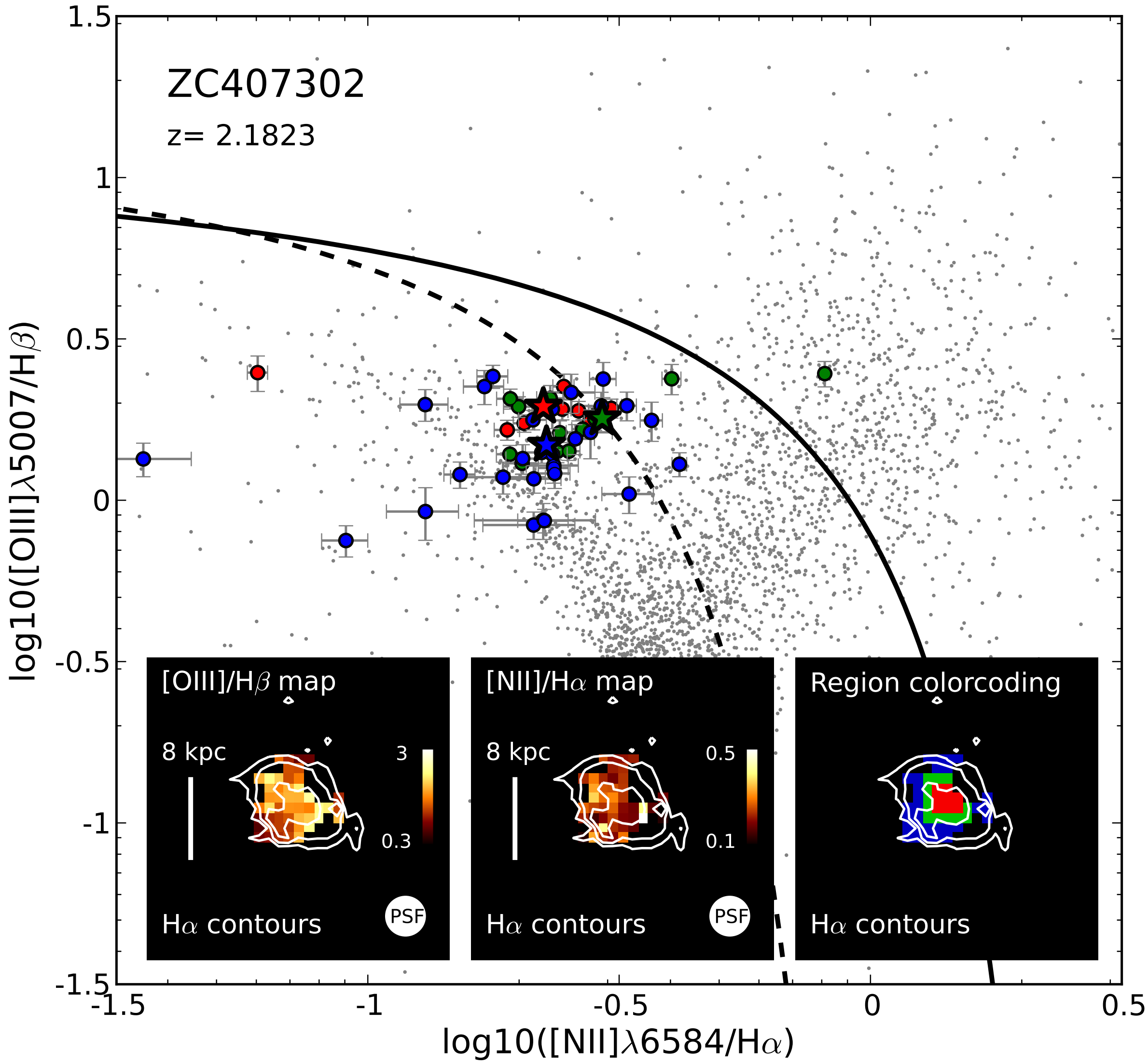

Figure 5.12: Pixel-by-pixel BPT diagram for ZC407302. Symbols and insets are the same as for Figure 5.11. The emission line ratio maps are mostly uniform and all regions of the galaxy are consistent with excitation from HII regions.

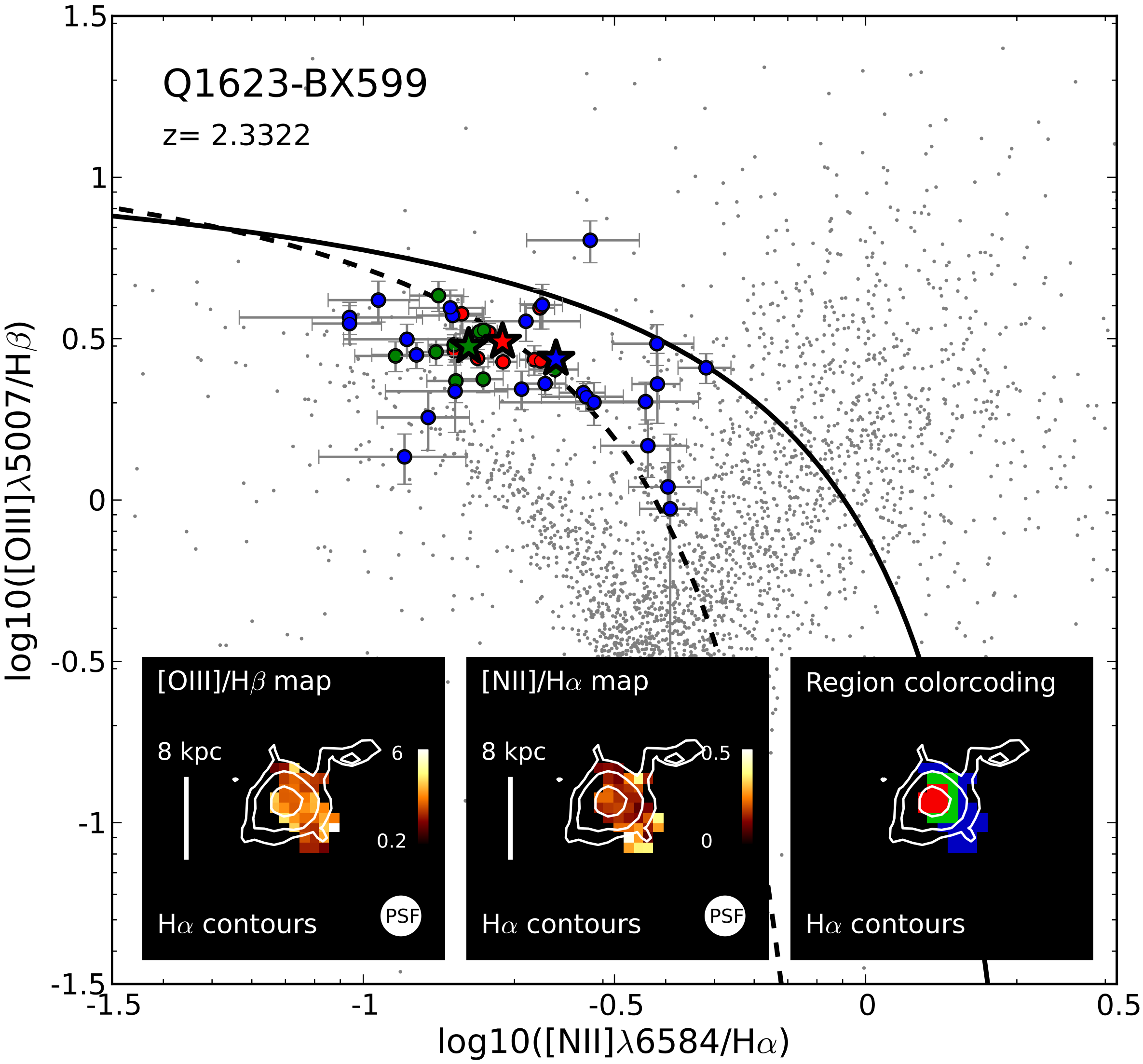

Figure 5.13: Pixel-by-pixel BPT diagram for Q1623-BX599. Symbols and insets are the same as for Figures 5.11 and 5.12. The emission line ratios for all regions are consistent with pure star-formation.

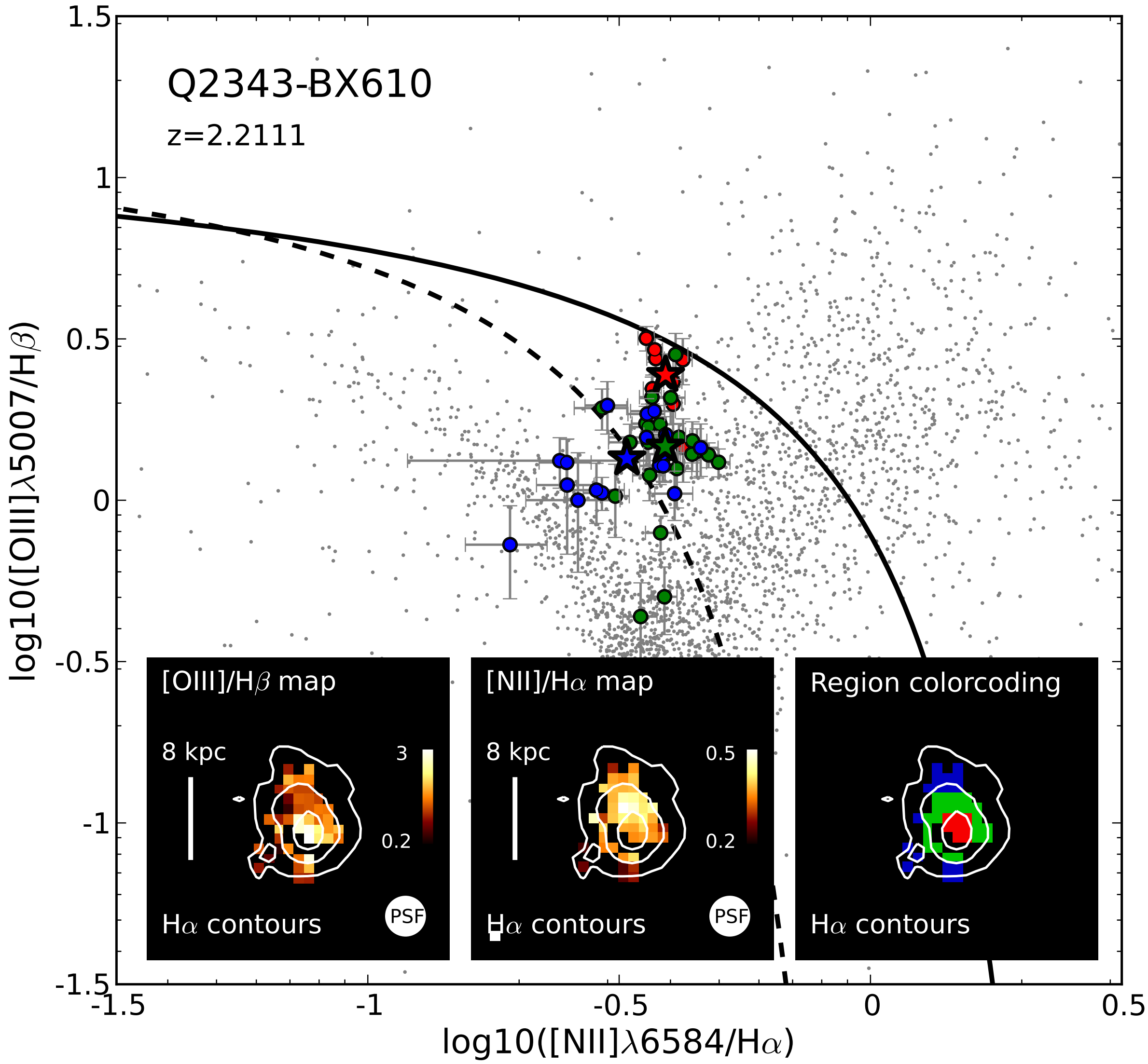

Figure 5.14: Pixel-by-pixel BPT diagram for Q2343-BX610. Symbols and insets are the same as for Figures 5.11, 5.12 and 5.13. The innermost region has elevated [NII]/Hα and [OIII]/Hβ ratios, suggestive of an AGN.

Q2343-BX610

Hα kinematics clearly show that this system is a large rotating disk with several bright clumps visible in the AO SINFONI data as well as in high resolution NIC2 H-band and WFC3 maps (Förster Schreiber et al. 2011a,b, S. Tacchella *et al.* in preparation). While there is no other evidence for an AGN from the available rest-UV spectrum (Erb et al. 2006b), there is an indication of a possible AGN from the observed mid-IR IRAC colors (Hainline et al. 2012; Förster Schreiber et al. 2011a, 2013a) and resolved analysis of the nuclear region shows elevated emission line ratios (Figure 5.14, particularly in [OIII]/Hβ) and very broad emission line wings (up to 1500 km/s, see: Förster Schreiber et al. 2013a), further supporting the presence of an obscured AGN. Interestingly, while the [OIII]/Hβ ratio peaks in the same location as the Hα peak, [NII]/Hα peaks slightly north of the center, at the continuum- and kinematic-derived center (0.4" or 3.5 kpc away).

There are two additional galaxies from our sample (Deep3a-6004 and K20-ID5) that show evidence for an AGN, but do not have a sufficiently high SNR in all four lines for the pixel-by-pixel analysis. Deep3a-6004, with a ring-like Hα morphology and kinematics suggestive of rotation (Förster Schreiber et al. 2009; Newman et al. 2013), is located in the 'composite' region of the BPT diagram. While it's VIMOS rest-UV spectrum shows no evidence for an AGN (E. Daddi, private communication), the nuclear region has an elevated [NII]/Hα ratio and very broad emission (up to 1500 km s^{-1}, see: Förster Schreiber et al. 2013a), both suggestive of an AGN. Unfortunately, the [OIII] and Hβ lines have too low SNR in the nuclear region to be analyzed. K20-ID5, while located in the AGN regime of the BPT diagram, has previously been characterized as a non-AGN galaxy with elevated emission line ratios due only to photoionization and shocks by van Dokkum et al. (2005). This analysis was based on the optical spectrum, which includes [HeII]λ1640 and [CII]λ1909 emission, but no higher ionization lines such as [CIV]λ1549 that would allow unambiguous identification of an AGN (Daddi et al. 2004b). However, in recent deep 4Ms *Chandra* observations, K20-ID5 has been detected in both hard and soft X-rays (Xue et al. 2011), and it's 1.4 GHz flux density is also consistent with the presence of an AGN. Moreover, it's *Spitzer*/IRAC colors (from the catalog of Wuyts et al. 2008) also satisfy the criteria for an AGN (Stern et al. 2005; Lacy et al. 2007; Donley et al. 2012). These new data support the notion that K20-ID5 does in fact harbor an AGN, though shocks in the nucleus and the disk are not excluded.

One other galaxy from our sample (Q2343-BX389) lies in the AGN regime of the BPT diagram, although it is not clear if it in fact contains an AGN. First, the Hβ absorption correction brings it closer to the 'composite' region of the BPT diagram (see Figure 5.9). Second, the [NII]/Hα ratio (0.18 ± 0.03) is quite low for a galaxy with an AGN. Finally, the Hβ line is affected by an OH sky line for a region of the galaxy and this could be affecting its positions in the BPT diagram. On the other hand, Q2343-BX389 is fairly massive ($M_* \sim 4\times10^{10}$ $M_\odot$), and close to the stellar mass for which most $z \sim 2$ SFGs host an AGN (10^{11} $M_\odot$), as seen by Förster Schreiber et al. (2013a), and the inner region of the galaxy is offset towards higher excitation than the outer region (Figure 5.10). Unfortunately, our current data are insufficient for determining whether or not this galaxy contains an AGN.

Our results from the analysis of spatially-integrated line ratios combined with other source properties suggest that there is no single dominant mechanism common to all galaxies, which is causing the observed offset in the BPT diagram, compared to the location of local SDSS galaxies. Known AGNs (Deep3a-15504 and K20-ID5) are located in the AGN region and other sources show a similar offset as found in other high-z studies (see e.g.: Erb et al. 2006a; Shapley et al. 2005; Liu et al. 2008; Kriek et al. 2007; Hayashi et al. 2009; Yabe et al. 2012; Trump et al. 2013), being located towards higher values in [NII]/Hα and [OIII]/Hβ and in between the AGN and star-forming branch. For these objects, contributions from (possibly low-luminosity) AGN (for Q2343-BX610 and Deep3a-6004) as well as (possibly outflow-related) shocks or an ISM with higher electron density and ionization parameter (for Q1307-BM1163, K20-ID7, Q2343-BX389 and Q1623-BX599) may be possible (e.g., Shapley et al. 2005; Liu et al. 2008; Erb et al. 2006a; Wright et al. 2009, 2010; Newman et al. 2012a). We probe the latter two scenarios using photoionization and shock models in section 5.3.2.

We note that the effect of spatial resolution on the determination of line ratios and excitation mechanism has previously been explored by previous authors. Yuan et al. (2013a) found that coarser resolution can lead to flatter line ratio gradients and Trump et al. (2011) showed with spatially resolved WFC3 GRISM data that many low mass $z \sim 2$ SFGs could host weak AGN, both in line with our findings.

The key result from this section is that we are able to *identify potential low-luminosity or obscured AGN through the use of resolved line ratio measurements* (e.g. Q2343-BX610), which would not be identified as such using integrated data. Using this technique, we also find that not all high-z galaxies in or near the composite region appear to contain AGN.

MEx diagnostic at high-z

Recently, Juneau et al. (2011) introduced a new excitation diagnostic that could be used in the absence of an [NII] and Hα measurement, the Mass-Excitation diagnostic (MEx). This diagnostic uses the well-known correlation between galaxy stellar mass and gas phase metallicity to create an alternate BPT-like diagram with [OIII]/Hβ vs. stellar mass. While both Juneau et al. (2013) and Trump et al. (2013) have shown that this relation, which was calibrated locally, holds up to z $\lesssim$ 1.6, separating AGN and star-forming galaxies, we hope to test whether this relation could also be used for our $z \sim 2$ objects.

As seen in the left panel of Figure 5.15, we find that this diagnostic does not work for our $z \sim 2$ galaxies. All of our galaxies with all four emission lines ([NII], Hα, [OIII], Hβ) fall in the AGN regime of the MEx diagram regardless of their position in the original BPT diagram. This is not surprising given the strong offset of $z \sim 2$ galaxies in the stellar mass-metallicity relation. In order to quantify the effect of the evolution of the mass-metallicity relation on this discrepancy, we derive a simple correction for the stellar mass (i.e. what would the stellar mass of our $z \sim 2$ galaxies be at z $\sim$ 0 for the same value of [NII]/Hα). First, we calculate the shift in stellar mass as a function of metallicity between the Erb et al. (2006a) $z \sim 2$ relation and the Tremonti et al. (2004) SDSS local relation (using the N2 indicator). Then we use the Erb et al. (2006b) mass-metallicity relation to get the mass shift

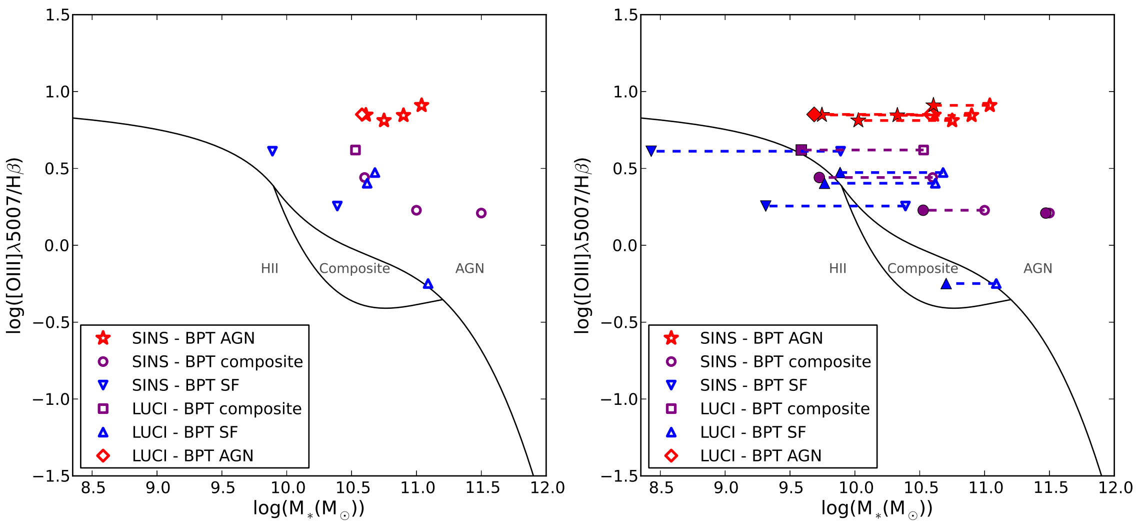

Figure 5.15: MEx diagnostic from Juneau et al. (2011) with SINS/zC-SINF and LUCI galaxies. The left panel shows the traditional MEx diagnostic with the galaxies color and symbol coded by their position in the BPT diagram. Red stars and diamonds are SINS and LUCI AGN, purple circles and squares are SINS and LUCI composite galaxies, and blue inverted and upright triangles are SINS and LUCI star-forming galaxies, according to the BPT diagram. In the right panel, we shift the data points according to the shift in the mass-metallicity relation between z $\sim$ 0 and 2 (using the Erb et al. (2006a) and Tremonti et al. (2004) relations). The original points are shown as open symbols and the shifted points are shown as closed symbols. While the MEx diagnostic does not accurately predict the location of $z \sim 2$ galaxies in the BPT diagram, applying a simple shift according to the mass-metallicity relation brings the two diagnostics into better agreement.

as a function of stellar mass and apply this shift to our $z \sim 2$ galaxies in Figure 5.15 (right panel). We note that this correction can not account for the presence of shocks and elevated ionization parameter, which could also affect the MEx diagnostic at $z \sim 2$.

We find that this corrected MEx diagnostic does a reasonably good job of predicting the location of the galaxies in the BPT diagram: The BPT star-forming galaxies (left of the Kauffmann et al. (2003) relation) all fall in the MEx star-forming regime or close to it; all but one of the BPT composite galaxies are shifted towards the border between the AGN and star-forming regimes; and the BPT AGN galaxies are still in the MEx AGN regime. In fact, we find that the two BPT composite galaxies that still lie in the AGN regime of the 'corrected' MEx diagram (Deep3a-6004 and Q2343-BX610) are also classified as AGN when using spatially resolved analysis.

5.3.2 Comparison to Photoionization and Shock models

We generate both photoionization and shock models to explore the effect of these processes on the location of high-z galaxies in the BPT diagram. The photoionization models are created using SEDs generated with Starburst99 (Leitherer et al. 1999; Vázquez & Leitherer 2005), along with the photoionization code Cloudy (Ferland et al. 2013). We assume a spherical geometry, a uniform electron density of 100 cm^{-3}, and an ISM dust model. In generating the SEDs we assume a 10 Myr old cloud with a constant SFR of 100 $M_\odot$ yr^{-1}(the median for the SINS galaxies), a Kroupa (2001) IMF, high mass-loss stellar evolution tracks from the Geneva group (Meynet et al. 1994) and a Pauldrach/Hillier atmosphere (Pauldrach et al. 2001; Hillier & Miller 1998). Models are generated for a range of metallicities (for $0.2Z_\odot$, $0.4Z_\odot$ and $Z_\odot$) and ionization parameters (logU = -3.5 to -1.8). Using an open geometry has little effect on the resulting line ratios, as does altering the filling factor (we consider a filling factor of 1 here), changing the density (between 1 and 500 cm^{-3}), adding molecules, removing the grain model, or changing the SFR by an order of magnitude.

The shock models are generated according to the method outlined in Gnat & Sternberg (2009) for the same metallicities as above (0.2–1 $Z_\odot$) and for shock velocities of 200, 500 and 1000 km s^{-1}(comparable to the velocities of the warm ionized component and hot wind fluid in galactic outflows, see Veilleux et al. 2005). In these shock models, we have calculated the non-equilibrium ionization and cooling, followed the radiative transfer of the shock self-radiation through the postshock cooling layers, taken into account the resulting photoionization and heating, and followed the dynamics of the cooling gas. We have also followed the emission-line intensities of several lines produced in the postshock cooling layers.

To obtain models with both photoionization and shocks, we normalize the lines fluxes in each of the photoionization and shock models by the Hα flux, and combine them with varying contributions, as shown in Figure 16. The SINS and LUCI data (particularly in the 'composite' region of the BPT diagram) are best fit by the models with a 25% flux contribution to the Hα emission from shocks, and are fit equally well with either the 500 or 1000 km s^{-1} shock velocity models, or the 200 km s^{-1} model with a 50–75% flux contribution from shocks. Incidentally, this is consistent with what was found by Newman et al. (2012a) for the fraction of Hα emission deriving from shocks (15–30%) in winds from individual star-forming clumps in a $z \sim 2$ SFG, assuming the higher velocity models. However, we note that if the Hβ absorption correction shown in Figure 9 is applied, the data points may be more consistent with the 100% photoionization model. Both the 100% and the 75% photoionization models imply ionization parameters of logU = -3 to -1.8 for our galaxies.

If we compare the metallicities from the models with those assumed using the Pettini & Pagel (2004) [NII]/Hα calibration (indicated by the grey lines in Figure 5.16), we find that galaxies determined to have close to solar metallicity based solely on their [NII]/Hα ratios, could indeed have metallicities as low as $0.2Z_\odot$ when accounting for photoionization effects and shocks (for both galaxies with and without evidence for AGN). The discrepancy is lower when the metallicities are calibrated using the O3N2 diagnostic (see next section, and Table 5.3), but there is still a significant offset between that calibration and the metallicities determined from the models. When considering the non-AGN galaxies that fall within the best fit model grid (Q1307-BM1163, K20-ID7, GN-21496), the metallicities ($Z/Z_{\odot}$) calculated with the N2 diagnostic are overestimated (as compared with the models) by a factor of $\sim$3, and those calculated with the O3N2 diagnostic are overestimated by a factor of $\sim$2.

Our models are roughly consistent with those of previous work on photoionization and shock models (see e.g. Dopita & Sutherland 1995; Dopita et al. 2000, 2006; Allen et al. 2008; Levesque et al. 2010; Rich et al. 2011). The 100% photoionization models occupy a similar region of parameter space (mostly in the HII region and part of the composite region), as those from Dopita et al. (2000), Dopita et al. (2006) and Levesque et al. (2010), and the shock model produces similar line intensities as for other fast shock codes (e.g. Allen et al. 2008). We compare our combined shock and photoionization models to those of Rich et al. (2011), and find good overall agreement, with [NII]/Hα increasing with shock fraction, although we find an overall decrease in [OIII]/Hβ with shock fraction while they find an increase.

From our models, we find that most or all of the galaxies located in the 'composite' region of the BPT diagram need not contain an AGN and may only lie there because of shocks and photoionization (particularly if we correct Hβ for stellar absorption). Rich et al. (2010, 2011) showed a similar effect of shocks on local galaxies in the BPT diagram. Furthermore, metallicities based solely on the [NII]/Hα local calibration could be severely overestimated, and these models allow us to determine the expected metallicities when shocks are present.

5.3.3 Comparison of metallicity indicators

A discussion of the mass-metallicity relation for the full SINS/zC-SINF and LUCI samples as well as resolved metallicity gradients will be discussed by Kurk et al. (2013). Here, we compare the gas phase metallicities derived using different nebular line ratios, all calibrated locally. Kewley & Ellison (2008), among others, have shown that the choice of metallicity calibration can have a large effect on the resulting metallicity, even for local SDSS galaxies. However, here we explore additional systematic discrepancies that can arise from differing ISM conditions in high-z galaxies.

In Figure 5.17, we have plotted the O3N2 versus N2-based metallicities of our galaxies using the Pettini & Pagel (2004) calibrations. The deviation from the 1:1 relation is reminiscent of the offset above the SDSS star-forming sequence in the BPT diagram (Figure 5.6), and could reflect different physical conditions locally and at $z \sim 2$ or an obscured AGN contribution, driving the line excitation. Indeed, for AGN galaxies we find a mean offset between the gas-phase metallicities derived with the two different methods of 0.28dex (stddev = 0.12dex), while for the non-AGN galaxies, we find a mean offset of 0.16dex (stddev = 0.06dex). If we account for stellar Hβ absorption, as previously shown in figure 5.9 for the BPT diagram, the deviation from the 1:1 relation decreases but the average offset is still 0.13dex (stddev = 0.06dex) for the non-AGN and 0.24 (stddev = 0.12dex) for the AGN galaxies, towards lower log(O/H) with the O3N2 calibration.

Thus, as shown by Liu et al. (2008), some metallicity calibrations (e.g. N2) are more affected than others by the presence of shocks, AGN or higher interstellar pressure, and

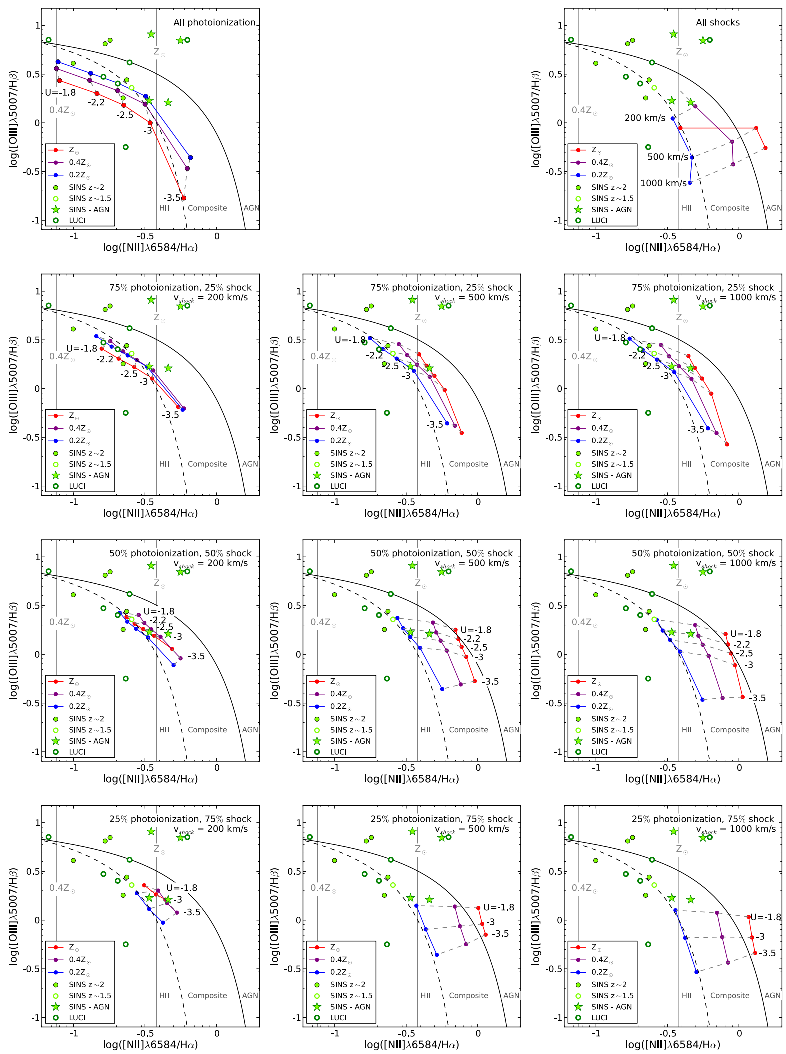

Figure 5.16: The BPT diagram with SINS and LUCI data as well as photoionization and shock models. The different panels represent different contribution fractions from photoionization and shocks, and different shock velocities. The colored lines represent different metallicities with red, purple and blue being $Z_{\odot}$, $0.4Z_{\odot}$, and $0.2Z_{\odot}$, respectively. The data points connected by grey dashed lines represent different ionization parameters in all but the upper right panel (where they represent different velocities), ranging from logU = -3.5 to -1.8. The vertical grey lines show the corresponding [NII]/Hα values for $Z_{\odot}$ and $0.4Z_{\odot}$ using the Pettini & Pagel (2004) calibration. The combined photoionization and shock models occupy much of the ‘composite’ region of the BPT diagram and thus these processes alone may be responsible for the positions of many $z \sim 2$ SFGs in the diagram, without the need to invoke an AGN.

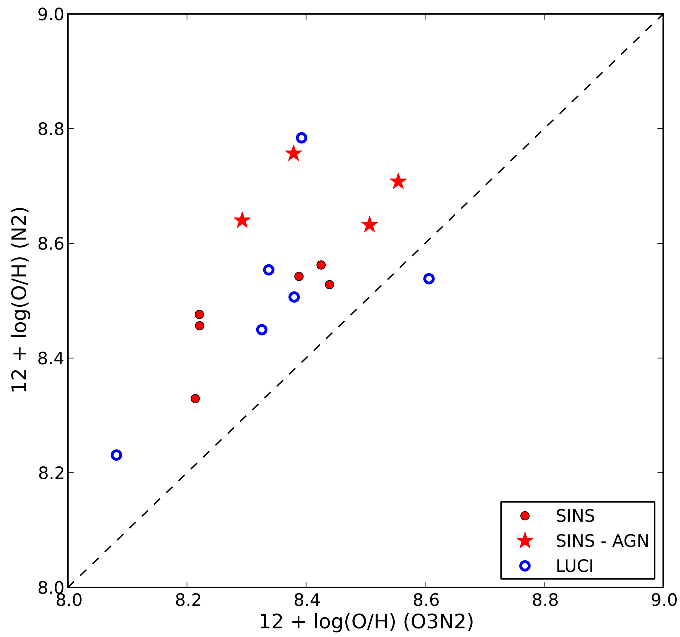

Figure 5.17: Comparison of gas phase metallicities calibrated using either the [NII]/Hα calibration or the [OIII]/Hβ/[NII]/Hα calibration (both from Pettini & Pagel 2004). The 1:1 relation is shown by the dashed line, SINS galaxies are shown as red symbols (filled circles for star-forming, and stars for AGN), and LUCI galaxies are shown as blue open circles. The N2 diagnostic is biased at $z \sim 2$, systematically producing higher metallicities than the O3N2 diagnostic, even with the exclusion of AGN galaxies.

even while excluding the AGN galaxies, there is still an offset between the two calibrations. As mentioned in the previous section, using the O3N2 calibration brings the metallicity determinations into closer agreement with the photoionization and shock models presented here (as compared with the N2 calibration), but there is still some inconsistency. Despite the observed offsets, relative measurements among galaxies remain unaltered and the use of one or the other indicator would lead to similar conclusions.

Based on our findings here and in Section 5.3.2, it is possible that the mass-metallicity relation at $z \sim 2$ based on the [NII]/Hα diagnostic could be overestimated by a factor of 2–3 in Z. This discrepancy may be even worse considering that we have excluded from this calculation AGN that have been identified solely based on spatially resolved observations.

5.4 Conclusions

Based on 22 z∼1.4–2.5 SFGs from the SINS/zC-SINF and LUCI surveys (10 with spatially resolved data), we explore the effects of AGN, shocks and photoionization on line ratio diagnostics at $z \sim 2$. In particular, our spatially-resolved data allow us to investigate how integrated line ratio measurements may be impacted by different excitation mechanisms. Our findings are as follows:

- With the use of spatially resolved line ratios, we are able to identify low-luminosity or obscured AGN that would otherwise not be detectable from integrated measurements, wherein the line ratios are the product of both a star-formation dominated disk and a highly excited nuclear region.

- Shocks and photoionization may be responsible for the location of many $z \sim 2$ galaxies in the 'composite' region of the BPT diagram. Shocks could contribute up to ∼25% of the Hα flux for our sample.

- In the composite region of the BPT diagram, there is a mix of galaxies with and without evidence for AGN and the prevalence of an AGN in this region appears to be correlated with [NII]/Hα(or similarly M_*).

- The MEx diagnostic (Juneau et al. 2011) does not accurately separate $z \sim 2$ star-forming and AGN galaxies according to the BPT diagram. However, applying a shift to M_* values based on the offset between the local and $z \sim 2$ mass-metallicity relations improves consistency of galaxy classification between the BPT and MEx diagrams.

- Gas-phase metallicities that are determined from local calibrations appear biased to higher metallicities at high-z when the presence of photoionization and shocks are considered, by up to a factor of 3 (when using the N2 calibration) or 2 (when using the O3N2 calibration).

The key take-away messages from this paper are that one must be careful when using integrated line ratios, as there may be a large range in excitation that is hidden in the average spectrum and that the effects of shocks, photoionization and the presence of an AGN may all be responsible for elevated line ratios in $z \sim 2$ SFGs.

Chapter 6

Conclusions

In this dissertation, I have used high-quality integral-field unit spectroscopic data to probe the properties and influence of galactic scale outflows from $z \sim 2$ star-forming galaxies (SFGs). These outflows have a significant impact on galaxy evolution, as they enrich the intergalactic medium (IGM) with metals and hot gas, regulate star-formation and potentially quench it in massive galaxies. As mentioned in Chapter 1, there are still several key issues concerning galactic winds that are not well understood, such as how they are launched from SFGs, the total mass and energy that they carry, and their influence on galaxy evolution. Throughout this dissertation, I have attempted to answer three main questions, which could shed light on these issues:

- What drives galactic-scale winds at $z \sim 2$?
- How do winds affect their host galaxies?
- What is the nature of the dispersion dominated SFGs at $z \sim 2$?

6.1 What drives galactic winds at $z \sim 2$?

Various models have been proposed to explain the origin of galactic winds both locally and at high-z. These include energy and momentum feedback from supernovae, stellar winds, HII regions, cosmic rays and radiation pressure (Heckman et al. 1990; Veilleux et al. 2005; Murray et al. 2005, 2010; Ostriker & Shetty 2011). While all of these components likely play some role in the launching of outflows, the relative importance of different mechanisms is not well understood. Furthermore, it is not clear if the mechanisms responsible for launching winds in local ULIRGs and starburst is the same as for $z \sim 2$ 'normal' SFGs.

From Chapter 2, the study of the galactic winds from star-forming clumps in one exemplary $z \sim 2$ SFG, we were able to probe the energetics and structure of the wind in detail. We found that the energy and mass contained in the warm ionized component of the outflow from individual clumps rivaled and perhaps exceeded that from entire local ULIRGs and dwarf starburst galaxies. However, the ISM conditions in these clumps were more similar to those of local starbursts than local normal disk galaxies, suggesting that the wind launching mechanisms could also be similar. Finally, we found that the energy and momentum rates in the clump outflows were consistent with both energy and momentum-driven winds. On the other hand, in Chapter 3, I showed that the strength of outflows was positively correlated with the star formation rate surface density, which could lend support to the momentum-driven wind model.

It is also not well understood what are the respective contributions to galactic-scale outflows from star-formation versus AGN feedback. From our sample of $z \sim 2$ SFGs, we found that strong outflows with mass-loading factors (the ratio of the mass outflow rate to the star formation rate) of ∼1 are driven purely from star formation without any contribution from an AGN. This was shown in Chapter 3 by the large spatial extent of broad emission (due to outflows) in our galaxies, well beyond the central regions where an AGN would lie. In addition, the broad emission studied in Chapter 2 was located on and around the star-forming clumps, also quite spatially extended and away from the center of the galaxy. Finally, we demonstrated (both in Chapters 2 and 5) that shocks may be present in the outflows and that this can affect the location of galaxies in the BPT diagram. Thus, due to these shocks and extreme ISM conditions, some $z \sim 2$ SFGs could be pushed towards the AGN branch of the BPT diagram, while they in fact, do not have any contribution (to their emission or outflows) from AGN.

6.2 The effect of winds on their host galaxies

In this dissertation, I presented evidence for outflowing gas in the form of broad (mostly blueshifted) emission lines, indicative of warm ionized gas in the ISM or halo of the galaxy moving at several 100 km s^{-1}. But can this gas escape the galactic gravitational potential? In Chapter 2, I showed that much of the outflowing gas from the star-forming clumps could escape the potential of not only the clumps, but also the galaxy, based on pressure balance arguments and the velocity of the gas. In general, the average velocity of the warm ionized component is comparable to the escape velocity of SFGs from our sample, suggesting that some gas (and thus the metals in that gas) could escape. I also addressed the question of whether or not star-formation feedback could be responsible for the elevated velocity dispersions observed in $z \sim 2$ SFGs, and found that they could only contribute a small fraction to the overall turbulence. Additionally, in Chapter 3, I showed that the majority of outflowing gas came from the highest stellar mass galaxies, near the Schechter mass, suggesting that they could in fact be responsible for the quenching of SFGs at z ∼ 2, removing the reservoir of gas required for star-formation.

6.3 The nature of dispersion-dominated galaxies

In Chapter 4, I discussed the class of $z \sim 2$ galaxies for which velocity dispersion dominates the kinematic signature. Apparently, the classification of galaxies as 'rotation' or 'dispersion dominated' is a strong function of both the galaxy size and the spatial resolution of the data. In fact, with higher spatial resolution data, many of these objects exhibit large scale velocity gradients, indicative of orbital motion. The most likely interpretation is that this orbital motion is from rotation, although in some objects it may be the orbital motion of two interacting galaxies. Furthermore, these galaxies have lower stellar masses, higher gas fractions, younger ages and lower gas-phase metallicities than larger rotating disk galaxies, suggesting that they could be an earlier evolutionary stage, and eventually turn into 'rotation-dominated' galaxies as they build up their stellar masses and mature. Tying this into the issue of galactic-scale outflows, we find that 'dispersion-dominated' galaxies are more often over the star-formation rate surface density threshold for strong outflows described in Chapter 3, which could mean that $z \sim 2$ SFGs in an early stage are more likely to dispel gas through galactic winds, and this naturally leads to the lower gas fractions observed in 'rotation-dominated' galaxies.

6.4 Final Remarks

Taken together, this dissertation describes the structure, mass, energetics and potential origin of galactic winds in $z \sim 2$ SFGs. It shows how these winds affect their host galaxies, regulating and potentially shutting off star-formation in the most massive objects. However, many questions still remain unanswered. While we are able to compare different mechanisms for launching outflows based on the energetics and trends we observe in $z \sim 2$ outflows, there is still no solid evidence distinguishing between the different models. In addition, one of the major issues that still clouds our knowledge of the structure and impact of galactic scale outflows is the lack of multi-phase data from the same object both locally and at high-z. While it is useful to individually constrain the amount of mass and energy in the warm ionized, hot ionized, neutral or molecular components, without a total accounting of all of the gas, we do not truly understand the impact of these winds.

Bibliography

Abraham, R. G., et al. 2004, AJ, 127, 2455
Adelberger, K. L., Shapley, A. E., Steidel, C. C., et al. 2005, ApJ, 629, 636
Adelberger, K. L., Steidel, C. C., Shapley, A. E., et al. 2004, ApJ, 607, 226
Adelberger, K. L., Steidel, C. C., Shapley, A. E., & Pettini, M. 2003, ApJ, 584, 45
Adelman-McCarthy, J. K., & et al. 2009, VizieR Online Data Catalog, 2294, 0
Ageorges, N., Seifert, W., Jütte, M., et al. 2010, in Society of Photo-Optical Instrumentation Engineers (SPIE) Conference Series, Vol. 7735, Society of Photo-Optical Instrumentation Engineers (SPIE) Conference Series
Agertz, O., Lake, G., Teyssier, R., et al. 2009, MNRAS, 392, 294
Allen, M. G., Groves, B. A., Dopita, M. A., Sutherland, R. S., & Kewley, L. J. 2008, ApJS, 178, 20
Asplund, M., Grevesse, N., Sauval, A. J., & Scott, P. 2009, ARA&A, 47, 481
Baldwin, J. A., Phillips, M. M., & Terlevich, R. 1981, PASP, 93, 5
Barger, A. J., Cowie, L. L., & Wang, W.-H. 2008, ApJ, 689, 687
Barro, G., Faber, S. M., Pérez-González, P. G., et al. 2013, ApJ, 765, 104
Berta, S., Magnelli, B., Nordon, R., et al. 2011, A&A, 532, A49
Bigiel, F., Leroy, A., Walter, F., et al. 2008, AJ, 136, 2846
Bigiel, F., Leroy, A. K., Walter, F., et al. 2011, ApJ, 730, L13
Birnboim, Y., Dekel, A., & Neistein, E. 2007, MNRAS, 380, 339
Bolatto, A. D., Leroy, A. K., Rosolowsky, E., Walter, F., & Blitz, L. 2008, ApJ, 686, 948
Bonnet, H., et al. 2004, in Presented at the Society of Photo-Optical Instrumentation Engineers (SPIE) Conference, Vol. 5490, Advancements in Adaptive Optics. Edited by Domenico B. Calia, Brent L. Ellerbroek, and Roberto Ragazzoni. Proceedings of the SPIE, Volume 5490, pp. 130-138 (2004)., ed. D. Bonaccini Calia, B. L. Ellerbroek, & R. Ragazzoni, 130
Bordoloi, R., Lilly, S. J., Kacprzak, G. G., & Churchill, C. W. 2012, ArXiv e-prints, arXiv:1211.3774 [astro-ph.CO]
Bordoloi, R., Lilly, S. J., Knobel, C., et al. 2011, ApJ, 743, 10
Bouché, N., Hohensee, W., Vargas, R., et al. 2012, MNRAS, 426, 801
Bouché, N., et al. 2007, ApJ, 671, 303
Bournaud, F., Elmegreen, B. G., & Elmegreen, D. M. 2007, ApJ, 670, 237
Bournaud, F., Elmegreen, B. G., & Martig, M. 2009, ApJ, 707, L1

Bournaud, F., Elmegreen, B. G., Teyssier, R., Block, D. L., & Puerari, I. 2010, MNRAS, 409, 1088
Bower, R. G., Benson, A. J., Malbon, R., et al. 2006, MNRAS, 370, 645
Brinchmann, J., Pettini, M., & Charlot, S. 2008, MNRAS, 385, 769
Bruzual, G., & Charlot, S. 2003, MNRAS, 344, 1000
Burkert, A., Genzel, R., Bouché, N., et al. 2010, ApJ, 725, 2324
Buschkamp, P., Hofmann, R., Gemperlein, H., et al. 2010, in Society of Photo-Optical Instrumentation Engineers (SPIE) Conference Series, Vol. 7735, Society of Photo-Optical Instrumentation Engineers (SPIE) Conference Series
Cacciato, M., Dekel, A., & Genel, S. 2012, MNRAS, 421, 818
Calzetti, D., Armus, L., Bohlin, R. C., et al. 2000, ApJ, 533, 682
Catinella, B., Schiminovich, D., Kauffmann, G., et al. 2010, MNRAS, 403, 683
Cecil, G., Bland-Hawthorn, J., Veilleux, S., & Filippenko, A. V. 2001, ApJ, 555, 338
Ceverino, D., Dekel, A., & Bournaud, F. 2010, MNRAS, 404, 2151
Ceverino, D., Dekel, A., Mandelker, N., et al. 2012, MNRAS, 420, 3490
Chabrier, G. 2003, PASP, 115, 763
Chapman, S. C., Windhorst, R., Odewahn, S., Yan, H., & Conselice, C. 2003, ApJ, 599, 92
Chen, Y.-M., Tremonti, C. A., Heckman, T. M., et al. 2010, AJ, 140, 445
Cole, S., Lacey, C. G., Baugh, C. M., & Frenk, C. S. 2000, MNRAS, 319, 168
Conroy, C., Shapley, A. E., Tinker, J. L., Santos, M. R., & Lemson, G. 2008, ApJ, 679, 1192
Conroy, C., & Wechsler, R. H. 2009, ApJ, 696, 620
Contini, T., Garilli, B., Le Fèvre, O., et al. 2012, A&A, 539, A91
Cowie, L. L., Hu, E. M., & Songaila, A. 1995, AJ, 110, 1576
Cresci, G., et al. 2009, ApJ, 697, 115
Daddi, E., Cimatti, A., Renzini, A., et al. 2004a, ApJ, 617, 746
Daddi, E., Dannerbauer, H., Elbaz, D., et al. 2008, ApJ, 673, L21
Daddi, E., et al. 2004b, ApJ, 600, L127
—. 2007, ApJ, 670, 156
Daddi, E., Dannerbauer, H., Stern, D., et al. 2009, ApJ, 694, 1517
Daddi, E., Elbaz, D., Walter, F., et al. 2010a, ApJ, 714, L118
Daddi, E., Bournaud, F., Walter, F., et al. 2010b, ApJ, 713, 686
Danielson, A. L. R., Swinbank, A. M., Smail, I., et al. 2011, MNRAS, 410, 1687
Davé, R. 2008, MNRAS, 385, 147
Davé, R., Finlator, K., & Oppenheimer, B. D. 2011, MNRAS, 416, 1354
Davies, R., Förster Schreiber, N. M., Cresci, G., et al. 2011, ApJ, 741, 69
Davies, R. I. 2007, MNRAS, 375, 1099
Dekel, A., & Birnboim, Y. 2006, MNRAS, 368, 2
Dekel, A., & Krumholz, M. R. 2013, MNRAS, 432, 455
Dekel, A., Sari, R., & Ceverino, D. 2009, ApJ, 703, 785
Denicoló, G., Terlevich, R., & Terlevich, E. 2002, MNRAS, 330, 69
Devine, D., & Bally, J. 1999, ApJ, 510, 197
Donley, J. L., Koekemoer, A. M., Brusa, M., et al. 2012, ApJ, 748, 142

Dopita, M. A., Kewley, L. J., Heisler, C. A., & Sutherland, R. S. 2000, ApJ, 542, 224
Dopita, M. A., & Sutherland, R. S. 1995, ApJ, 455, 468
Dopita, M. A., Fischera, J., Sutherland, R. S., et al. 2006, ApJS, 167, 177
Downes, D., & Solomon, P. M. 1998, ApJ, 507, 615
Dufour, R. J., Talbot, Jr., R. J., Jensen, E. B., & Shields, G. A. 1980, ApJ, 236, 119
Dutton, A. A., van den Bosch, F. C., & Dekel, A. 2010, MNRAS, 405, 1690
Eisenhauer, F., et al. 2003, in Presented at the Society of Photo-Optical Instrumentation Engineers (SPIE) Conference, Vol. 4841, Instrument Design and Performance for Optical/Infrared Ground-based Telescopes. Edited by Iye, Masanori; Moorwood, Alan F. M. Proceedings of the SPIE, Volume 4841, pp. 1548-1561 (2003)., ed. M. Iye & A. F. M. Moorwood, 1548
Elbaz, D., et al. 2007, A&A, 468, 33
Elbaz, D., Dickinson, M., Hwang, H. S., et al. 2011, A&A, 533, A119
Elmegreen, B. G., Bournaud, F., & Elmegreen, D. M. 2008, ApJ, 688, 67
Elmegreen, B. G., & Burkert, A. 2010, ApJ, 712, 294
Elmegreen, B. G., & Elmegreen, D. M. 2005, ApJ, 627, 632
—. 2006, ApJ, 650, 644
—. 2010, ApJ, 722, 1895
Elmegreen, B. G., Elmegreen, D. M., Fernandez, M. X., & Lemonias, J. J. 2009a, ApJ, 692, 12
Elmegreen, D. M., Elmegreen, B. G., & Hirst, A. C. 2004a, ApJ, 604, L21
Elmegreen, D. M., Elmegreen, B. G., Marcus, M. T., et al. 2009b, ApJ, 701, 306
Elmegreen, D. M., Elmegreen, B. G., Rubin, D. S., & Schaffer, M. A. 2005, ApJ, 631, 85
Elmegreen, D. M., Elmegreen, B. G., & Sheets, C. M. 2004b, ApJ, 603, 74
Engel, H., Tacconi, L. J., Davies, R. I., et al. 2010, ApJ, 724, 233
Epinat, B., Contini, T., Le Fèvre, O., et al. 2009, A&A, 504, 789
Epinat, B., Tasca, L., Amram, P., et al. 2012, A&A, 539, A92
Erb, D. K. 2008, ApJ, 674, 151
Erb, D. K., Shapley, A. E., Pettini, M., et al. 2006a, ApJ, 644, 813
Erb, D. K., Shapley, A. E., Steidel, C. C., et al. 2003, ApJ, 591, 101
Erb, D. K., Steidel, C. C., Shapley, A. E., et al. 2006b, ApJ, 646, 107
Ferland, G. J., Porter, R. L., van Hoof, P. A. M., et al. 2013, Rev. Mexicana Astron. Astrofis., 49, 137
Finlator, K., & Davé, R. 2008, MNRAS, 385, 2181
Förster Schreiber, N. M., Genzel, R., Lutz, D., Kunze, D., & Sternberg, A. 2001, ApJ, 552, 544
Förster Schreiber, N. M., Shapley, A. E., Erb, D. K., et al. 2011a, ApJ, 731, 65
Förster Schreiber, N. M., et al. 2006, ApJ, 645, 1062
—. 2009, ApJ, 706, 1364
Förster Schreiber, N. M., Shapley, A. E., Genzel, R., et al. 2011b, ApJ, 739, 45
Förster Schreiber, N. M., et al. 2013a, in preparation
—. 2013b, in preparation

Franx, M., Illingworth, G. D., Kelson, D. D., van Dokkum, P. G., & Tran, K.-V. 1997, ApJ, 486, L75
Franx, M., et al. 2003, ApJ, 587, L79
Genel, S., Dekel, A., & Cacciato, M. 2012a, MNRAS, 425, 788
Genel, S., Naab, T., Genzel, R., et al. 2012b, ApJ, 745, 11
Genzel, R., et al. 2006, Nature, 442, 786
—. 2008, ApJ, 687, 59
Genzel, R., Tacconi, L. J., Gracia-Carpio, J., et al. 2010, MNRAS, 407, 2091
Genzel, R., Newman, S., Jones, T., et al. 2011, ApJ, 733, 101
Gnat, O., & Sternberg, A. 2009, ApJ, 693, 1514
Gnerucci, A., Marconi, A., Capetti, A., Axon, D. J., & Robinson, A. 2010, A&A, 511, A19
Gonçalves, T. S., Basu-Zych, A., Overzier, R., et al. 2010, ApJ, 724, 1373
Green, A. W., Glazebrook, K., McGregor, P. J., et al. 2010, Nature, 467, 684
Guo, Y., Giavalisco, M., Cassata, P., et al. 2011, ApJ, 735, 18
Hainline, K. N., Shapley, A. E., Greene, J. E., et al. 2012, ApJ, 760, 74
Hayashi, M., Motohara, K., Shimasaku, K., et al. 2009, ApJ, 691, 140
Hayward, C. C., Jonsson, P., Kereš, D., et al. 2012, MNRAS, 424, 951
Heckman, T. M., Armus, L., & Miley, G. K. 1990, ApJS, 74, 833
Heckman, T. M., Lehnert, M. D., & Armus, L. 1993, in Astrophysics and Space Science Library, Vol. 188, The Environment and Evolution of Galaxies, ed. J. M. Shull & H. A. Thronson, 455
Hillier, D. J., & Miller, D. L. 1998, ApJ, 496, 407
Hopkins, A. M., & Beacom, J. F. 2006, ApJ, 651, 142
Hopkins, P. F., Quataert, E., & Murray, N. 2012, MNRAS, 421, 3522
Hwang, H. S., Elbaz, D., Dickinson, M., et al. 2011, A&A, 535, A60
Ichikawa, T., Kajisawa, M., & Akhlaghi, M. 2012, MNRAS, 422, 1014
Immeli, A., Samland, M., Gerhard, O., & Westera, P. 2004a, A&A, 413, 547
Immeli, A., Samland, M., Westera, P., & Gerhard, O. 2004b, ApJ, 611, 20
Jones, T., Ellis, R., Jullo, E., & Richard, J. 2010, ApJ, 725, L176
Jones, T., Stark, D. P., & Ellis, R. S. 2012, ApJ, 751, 51
Juneau, S., Dickinson, M., Alexander, D. M., & Salim, S. 2011, ApJ, 736, 104
Juneau, S., Glazebrook, K., Crampton, D., et al. 2005, ApJ, 619, L135
Juneau, S., Dickinson, M., Bournaud, F., et al. 2013, ApJ, 764, 176
Kacprzak, G. G., Churchill, C. W., & Nielsen, N. M. 2012, ApJ, 760, L7
Kassin, S. A., Weiner, B. J., Faber, S. M., et al. 2007, ApJ, 660, L35
—. 2012, ApJ, 758, 106
Katz, N., Weinberg, D. H., & Hernquist, L. 1996, ApJS, 105, 19
Kauffmann, G., Heckman, T. M., Tremonti, C., et al. 2003, MNRAS, 346, 1055
Kennicutt, Jr., R. C. 1998, ApJ, 498, 541
Kennicutt, Jr., R. C., Calzetti, D., Walter, F., et al. 2007, ApJ, 671, 333
Kereš, D., Katz, N., Fardal, M., Davé, R., & Weinberg, D. H. 2009, MNRAS, 395, 160
Kereš, D., Katz, N., Weinberg, D. H., & Davé, R. 2005, MNRAS, 363, 2

Kewley, L. J., & Dopita, M. A. 2002, ApJS, 142, 35
Kewley, L. J., Dopita, M. A., Leitherer, C., et al. 2013, ArXiv e-prints, arXiv:1307.0508 [astro-ph.CO]
Kewley, L. J., Dopita, M. A., Sutherland, R. S., Heisler, C. A., & Trevena, J. 2001a, ApJ, 556, 121
Kewley, L. J., & Ellison, S. L. 2008, ApJ, 681, 1183
Kewley, L. J., Groves, B., Kauffmann, G., & Heckman, T. 2006, MNRAS, 372, 961
Kewley, L. J., Heisler, C. A., Dopita, M. A., & Lumsden, S. 2001b, ApJS, 132, 37
Kitzbichler, M. G., & White, S. D. M. 2007, MNRAS, 376, 2
Komatsu, E., Smith, K. M., Dunkley, J., et al. 2011, ApJS, 192, 18
Kong, X., et al. 2006, ApJ, 638, 72
Kornei, K. A., Shapley, A. E., Martin, C. L., et al. 2012, ApJ, 758, 135
Kriek, M., van Dokkum, P. G., Labbé, I., et al. 2009, ApJ, 700, 221
Kriek, M., et al. 2007, ApJ, 669, 776
Kroupa, P. 2001, MNRAS, 322, 231
Krumholz, M., & Burkert, A. 2010, ApJ, 724, 895
Kurk, J., Cimatti, A., Zamorani, G., et al. 2009, A&A, 504, 331
Kurk, J., et al. 2013, in preparation
Lacy, M., Petric, A. O., Sajina, A., et al. 2007, AJ, 133, 186
Law, D. R., Shapley, A. E., Steidel, C. C., et al. 2012a, Nature, 487, 338
Law, D. R., Steidel, C. C., Erb, D. K., et al. 2007, ApJ, 669, 929
—. 2009, ApJ, 697, 2057
Law, D. R., Steidel, C. C., Shapley, A. E., et al. 2012b, ApJ, 759, 29
—. 2012c, ApJ, 745, 85
Le Borgne, D., Elbaz, D., Ocvirk, P., & Pichon, C. 2009, A&A, 504, 727
Le Floc'h, E., Papovich, C., Dole, H., et al. 2005, ApJ, 632, 169
Lehnert, M. D., & Heckman, T. M. 1996, ApJ, 462, 651
Lehnert, M. D., Heckman, T. M., & Weaver, K. A. 1999, ApJ, 523, 575
Leitherer, C., Schaerer, D., Goldader, J. D., et al. 1999, ApJS, 123, 3
Lemoine-Busserolle, M., & Lamareille, F. 2010, MNRAS, 402, 2291
Leroy, A. K., Bigiel, F., de Blok, W. J. G., et al. 2012, ArXiv e-prints, arXiv:1202.2873 [astro-ph.CO]
Levesque, E. M., Kewley, L. J., & Larson, K. L. 2010, AJ, 139, 712
Lilly, S. J., Carollo, C. M., Pipino, A., Renzini, A., & Peng, Y. 2013, ArXiv e-prints, arXiv:1303.5059 [astro-ph.CO]
Lilly, S. J., Le Fevre, O., Hammer, F., & Crampton, D. 1996, ApJ, 460, L1
Lilly, S. J., et al. 2007, ApJS, 172, 70
Lilly, S. J., Le Brun, V., Maier, C., et al. 2009, ApJS, 184, 218
Liu, X., Shapley, A. E., Coil, A. L., Brinchmann, J., & Ma, C.-P. 2008, ApJ, 678, 758
López-Sanjuan, C., Le Fèvre, O., Tasca, L. A. M., et al. 2013, A&A, 553, A78
Lowenthal, J. D., Koo, D. C., Guzman, R., et al. 1997, ApJ, 481, 673
Madau, P., Ferguson, H. C., Dickinson, M. E., et al. 1996, MNRAS, 283, 1388

Magnelli, B., Lutz, D., Santini, P., et al. 2012, A&A, 539, A155
Mancini, C., Förster Schreiber, N. M., Renzini, A., et al. 2011, ApJ, 743, 86
Mannucci, F., et al. 2009, MNRAS, 398, 1915
Martin, C. L. 1998, ApJ, 506, 222
—. 1999, ApJ, 513, 156
—. 2005, ApJ, 621, 227
Martin, C. L., Shapley, A. E., Coil, A. L., et al. 2012, ApJ, 760, 127
Matzner, C. D. 2002, ApJ, 566, 302
McCracken, H. J., Capak, P., Salvato, M., et al. 2010, ApJ, 708, 202
McKee, C. F., & Ostriker, J. P. 1977, ApJ, 218, 148
Meynet, G., Maeder, A., Schaller, G., Schaerer, D., & Charbonnel, C. 1994, A&AS, 103, 97
Mignoli, M., Cimatti, A., Zamorani, G., et al. 2005, A&A, 437, 883
Mo, H. J., Mao, S., & White, S. D. M. 1998, MNRAS, 295, 319
Murray, N., Ménard, B., & Thompson, T. A. 2011, ApJ, 735, 66
Murray, N., Quataert, E., & Thompson, T. A. 2005, ApJ, 618, 569
—. 2010, ApJ, 709, 191
Neichel, B., Hammer, F., Puech, M., et al. 2008, A&A, 484, 159
Nelson, E. J., van Dokkum, P. G., Brammer, G., et al. 2012, ApJ, 747, L28
Nelson, E. J., van Dokkum, P. G., Momcheva, I., et al. 2013, ApJ, 763, L16
Newman, S. F., Shapiro Griffin, K., Genzel, R., et al. 2012a, ApJ, 752, 111
Newman, S. F., Genzel, R., Förster-Schreiber, N. M., et al. 2012b, ApJ, 761, 43
Newman, S. F., Genzel, R., Förster Schreiber, N. M., et al. 2013, ApJ, 767, 104
Noeske, K. G., et al. 2007, ApJ, 660, L43
Noguchi, M. 1999, ApJ, 514, 77
Ocvirk, P., Pichon, C., & Teyssier, R. 2008, MNRAS, 390, 1326
Oppenheimer, B. D., & Davé, R. 2006, MNRAS, 373, 1265
—. 2008, MNRAS, 387, 577
Oser, L., Ostriker, J. P., Naab, T., Johansson, P. H., & Burkert, A. 2010, ApJ, 725, 2312
Osterbrock, D. E. 1989, Astrophysics of gaseous nebulae and active galactic nuclei (University Science Books)
Ostriker, E. C., & Shetty, R. 2011, ApJ, 731, 41
Pauldrach, A. W. A., Hoffmann, T. L., & Lennon, M. 2001, A&A, 375, 161
Peng, C. Y., Ho, L. C., Impey, C. D., & Rix, H.-W. 2002, AJ, 124, 266
Peng, Y.-j., Lilly, S. J., Kovač, K., et al. 2010, ApJ, 721, 193
Pettini, M., & Pagel, B. E. J. 2004, MNRAS, 348, L59
Pettini, M., Rix, S. A., Steidel, C. C., et al. 2002, ApJ, 569, 742
Pettini, M., Shapley, A. E., Steidel, C. C., et al. 2001, ApJ, 554, 981
Pettini, M., Steidel, C. C., Adelberger, K. L., Dickinson, M., & Giavalisco, M. 2000, ApJ, 528, 96
Puech, M., Hammer, F., Flores, H., Neichel, B., & Yang, Y. 2009, A&A, 493, 899
Puech, M., Hammer, F., Lehnert, M. D., & Flores, H. 2007, A&A, 466, 83
Queyrel, J., Contini, T., Kissler-Patig, M., et al. 2012, A&A, 539, A93

Rangel, C., Nandra, K., Laird, E. S., & Orange, P. 2013, MNRAS, 428, 3089
Renzini, A. 1997, ApJ, 488, 35
Rich, J. A., Dopita, M. A., Kewley, L. J., & Rupke, D. S. N. 2010, ApJ, 721, 505
Rich, J. A., Kewley, L. J., & Dopita, M. A. 2011, ApJ, 734, 87
Rodighiero, G., Daddi, E., Baronchelli, I., et al. 2011, ApJ, 739, L40
Rubin, K. H. R., Weiner, B. J., Koo, D. C., et al. 2010, ApJ, 719, 1503
Rupke, D. S., Veilleux, S., & Sanders, D. B. 2005, ApJS, 160, 115
Rupke, D. S. N., & Veilleux, S. 2011, ApJ, 729, L27
Saintonge, A., Tacconi, L. J., Fabello, S., et al. 2012, ApJ, 758, 73
Sargent, M. T., Béthermin, M., Daddi, E., & Elbaz, D. 2012, ApJ, 747, L31
Sato, T., Martin, C. L., Noeske, K. G., Koo, D. C., & Lotz, J. M. 2009, ApJ, 696, 214
Schreiber, J., Thatte, N., Eisenhauer, F., et al. 2004, in Astronomical Society of the Pacific Conference Series, Vol. 314, Astronomical Data Analysis Software and Systems (ADASS) XIII, ed. F. Ochsenbein, M. G. Allen, & D. Egret, 380
Seifert, W., Ageorges, N., Lehmitz, M., et al. 2010, in Society of Photo-Optical Instrumentation Engineers (SPIE) Conference Series, Vol. 7735, Society of Photo-Optical Instrumentation Engineers (SPIE) Conference Series
Shapiro, K. L., et al. 2008, ApJ, 682, 231
—. 2009, ApJ, 701, 955
Shapley, A. E., Steidel, C. C., Erb, D. K., et al. 2005, ApJ, 626, 698
Shapley, A. E., Steidel, C. C., Pettini, M., & Adelberger, K. L. 2003, ApJ, 588, 65
Smail, I., Ivison, R. J., & Blain, A. W. 1997, ApJ, 490, L5
Somerville, R. S., & Primack, J. R. 1999, MNRAS, 310, 1087
Springel, V., & Hernquist, L. 2003, MNRAS, 339, 312
Stahler, S. W., & Palla, F. 2005, The Formation of Stars (Wiley-VCH)
Stark, D. P., Ellis, R. S., Bunker, A., et al. 2009, ApJ, 697, 1493
Steidel, C. C., Adelberger, K. L., Giavalisco, M., Dickinson, M., & Pettini, M. 1999, ApJ, 519, 1
Steidel, C. C., Erb, D. K., Shapley, A. E., et al. 2010, ApJ, 717, 289
Steidel, C. C., Giavalisco, M., Pettini, M., Dickinson, M., & Adelberger, K. L. 1996, ApJ, 462, L17
Steidel, C. C., Shapley, A. E., Pettini, M., et al. 2004, ApJ, 604, 534
Stern, D., Eisenhardt, P., Gorjian, V., et al. 2005, ApJ, 631, 163
Strickland, D. K., & Heckman, T. M. 2009, ApJ, 697, 2030
Strickland, D. K., Heckman, T. M., Colbert, E. J. M., Hoopes, C. G., & Weaver, K. A. 2004, ApJS, 151, 193
Sturm, E., González-Alfonso, E., Veilleux, S., et al. 2011, ApJ, 733, L16
Sutherland, R. S., & Dopita, M. A. 1993, ApJS, 88, 253
Swinbank, A. M., Smail, I., Chapman, S. C., et al. 2004, ApJ, 617, 64
Swinbank, A. M., Smail, I., Sobral, D., et al. 2012a, ApJ, 760, 130
Swinbank, A. M., Sobral, D., Smail, I., et al. 2012b, MNRAS, 426, 935
Swinbank, A. M., Papadopoulos, P. P., Cox, P., et al. 2011, ApJ, 742, 11

Tacconi, L. J., et al. 2006, ApJ, 640, 228
—. 2008, ApJ, 680, 246
—. 2010, Nature, 463, 781
Tacconi, L. J., Neri, R., Genzel, R., et al. 2013, ApJ, 768, 74
Tecza, M., et al. 2004, ApJ, 605, L109
Tremonti, C. A., et al. 2004, ApJ, 613, 898
Trump, J. R., Weiner, B. J., Scarlata, C., et al. 2011, ApJ, 743, 144
Trump, J. R., Konidaris, N. P., Barro, G., et al. 2013, ApJ, 763, L6
van den Bergh, S., Abraham, R. G., Ellis, R. S., et al. 1996, AJ, 112, 359
van der Kruit, P. C., & Allen, R. J. 1978, ARA&A, 16, 103
van Dokkum, P. G., Kriek, M., Rodgers, B., Franx, M., & Puxley, P. 2005, ApJ, 622, L13
van Starkenburg, L., van der Werf, P. P., Franx, M., et al. 2008, A&A, 488, 99
Vázquez, G. A., & Leitherer, C. 2005, ApJ, 621, 695
Veilleux, S., Cecil, G., & Bland-Hawthorn, J. 2005, ARA&A, 43, 769
Veilleux, S., & Osterbrock, D. E. 1987, ApJS, 63, 295
Vergani, D., Epinat, B., Contini, T., et al. 2012, A&A, 546, A118
Weiner, B. J., Willmer, C. N. A., Faber, S. M., et al. 2006, ApJ, 653, 1027
Weiner, B. J., et al. 2009, ApJ, 692, 187
Westmoquette, M. S., Smith, L. J., Gallagher, J. S., & Exter, K. M. 2007, MNRAS, 381, 913
Wisnioski, E., Glazebrook, K., Blake, C., et al. 2012, MNRAS, 422, 3339
—. 2011, MNRAS, 417, 2601
Wright, S. A., Larkin, J. E., Graham, J. R., & Ma, C.-P. 2010, ApJ, 711, 1291
Wright, S. A., Larkin, J. E., Law, D. R., et al. 2009, ApJ, 699, 421
Wright, S. A., et al. 2007, ApJ, 658, 78
Wuyts, S., Labbé, I., Schreiber, N. M. F., et al. 2008, ApJ, 682, 985
Wuyts, S., Förster Schreiber, N. M., van der Wel, A., et al. 2011a, ApJ, 742, 96
Wuyts, S., Förster Schreiber, N. M., Lutz, D., et al. 2011b, ApJ, 738, 106
Wuyts, S., Förster Schreiber, N. M., Genzel, R., et al. 2012, ApJ, 753, 114
Xue, Y. Q., Luo, B., Brandt, W. N., et al. 2011, ApJS, 195, 10
Yabe, K., Ohta, K., Iwamuro, F., et al. 2012, PASJ, 64, 60
Yuan, T.-T., Kewley, L. J., & Rich, J. 2013a, ApJ, 767, 106
Yuan, T.-T., Kewley, L. J., & Richard, J. 2013b, ApJ, 763, 9